ANNUAL REPORT 2001

Optoelectronics Department

University of Ulm

Contents

Preface 1

Articles

GaAsSb/GaAs Lasers Emitting near 1.3 μm 3

Three-Terminal VCSEL 9

Polarization Control in VCSELs by Elliptic Surface Etching 15

Improved Output Performance of High-Power VCSELs 19

Data Transmission with 1.3 μm Wavelength InGaAsN VCSELs 27

Spatial Investigation of Transverse Mode Turn-On Dynamics in VCSELs 33

Theoretical Investigation of Transverse Modes in PCSELs 39

GaAs-Based Quantum Dot LEDs 45

Tapered Gain Region Laser Amplifiers 51

Unstable-Resonator Lasers 61

Optical Coatings for Laser Facets 67

Semiconductor Disk Lasers with Intra-Cavity Frequency Doubling 73

Dislocations in GaN 79

Substrates for Wide Bandgap Nitrides from Applications Perspective 83

Wafer-bonded, Tapered InGaAlP-LEDs 89

Extraction Efficiencies of Tapered AlInGaP LEDs Emitting at 650 nm 95

Tunable GaN-Based Laser Diode 101

Habilitation and Ph.D. Theses 107

Lists of Publications

Diploma Theses and Semester Projects 109

Talks 112

Publications and Conference Contributions 117

Submitted Publications and Conference Contributions 120

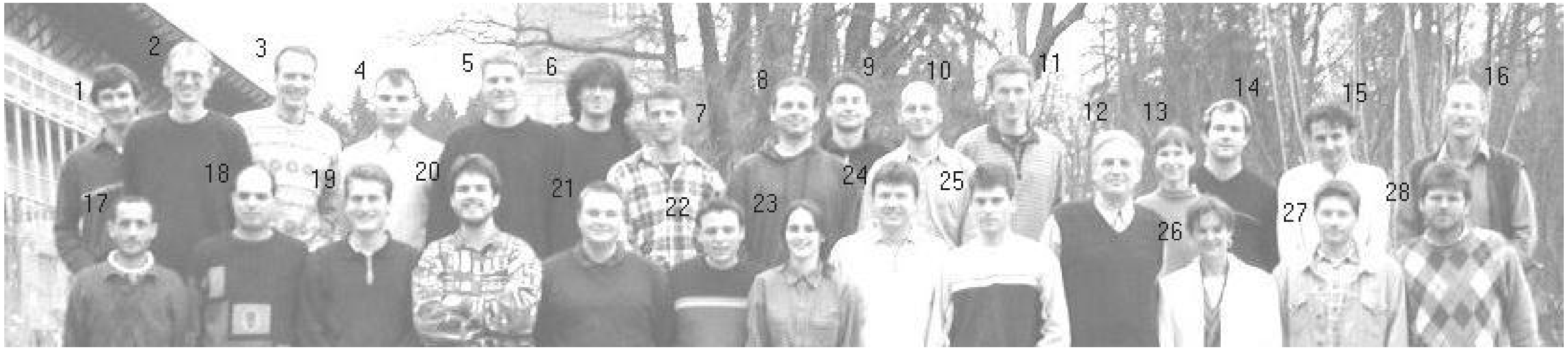

1: Felix Mederer
2: Matthias Seyboth
3: Matthias Golling
4: Pavel Ivanov
5: Michael C. Riedl
6: Fernando Rinaldi
7: Rainer Blood

8: Frank Demaria
9: Eckart Schiehlen
10: Heiko J. Unold
11: Rainer Michalzik
12: Georgi Stareev
13: Irene Ecker
14: Steffen Lorch

15: Vincent Voignier
16: Jürgen Mähnß
17: Safwat W.Z. Mahmoud
18: Ihab Kardosh
19: Christoph Eichler
20: Frank Habel
21: Marcus Scherer

22: Sven S. Schad
23: Barbara Neubert
24: Manfred Mundbrod
25: Eckard Deichsel
26: Christine Bunk
27: Thomas Knödl
28: Peter Unger

Missing in the picture

29: Roland Jäger
30: Jürgen Joos
31: Max Kicherer
32: Roger King

33: Christoph Kirchner
34: Ulrich Martin
35: Michael Miller
36: Veit Schwegler

37: Karl J. Ebeling
38: Josef Theisz
39: Susanne Döttinger
40: Gerlinde Meixner

41: Susanne Menzel
42: Sophie Pfetsch
43: Hildegard Mack

Optoelectronics Department University of Ulm

Albert-Einstein-Allee 45, D-89069 Ulm, Germany
Fax: +49–731/50–2 60 49
Phone: +49–731/50–

Intermediate Head of Department

Prof. Dr.	Peter Unger	–2 60 54	peter.unger@e-technik.uni-ulm.de

On leave at Infineon Technologies AG

Prof. Dr.	Karl Joachim Ebeling	–2 60 51	karl.ebeling@e-technik.uni-ulm.de

Senior Research Assistant

Dr.-Ing.	Rainer Michalzik	–2 60 48	rainer.michalzik@e-technik.uni-ulm.de

Cleanroom Management

Dr.-Ing.	Jürgen Mähnß	–2 60 53	juergen.maehnss@e-technik.uni-ulm.de

Secretaries

	Christine Bunk	–2 60 50	christine.bunk@e-technik.uni-ulm.de
	Hildegard Mack	–2 60 59	hildegard.mack@e-technik.uni-ulm.de

Research Staff

Dipl.-Ing.	Eckard Deichsel	–2 60 57	eckard.deichsel@e-technik.uni-ulm.de
Dipl.-Phys.	Frank Demaria	–2 60 46	frank.demaria@e-technik.uni-ulm.de
Dipl.-Ing.	Irene Ecker	–2 60 41	irene.ecker@e-technik.uni-ulm.de
Dipl.-Ing.	Christoph Eichler	–2 61 95	christoph.eichler@e-technik.uni-ulm.de
Dipl.-Ing.	Mattias Golling	–2 60 35	matthias.golling@e-technik.uni-ulm.de
Dipl.-Ing.	Frank Habel	–2 64 52	frank.habel@e-technik.uni-ulm.de
Dipl.-Ing.	Pavel Ivanov	–2 60 38	pavel.ivanov@e-technik.uni-ulm.de
Dipl.-Phys.	Roland Jäger	–2 60 40	roland.jaeger@e-technik.uni-ulm.de
Dipl.-Ing.	Jürgen Joos	–2 60 35	juergen.joos@e-technik.uni-ulm.de
Dipl.-Ing.	Ihab Kardosh	–2 60 36	ihab.kardosh@e-technik.uni-ulm.de
Dipl.-Phys.	Max Kicherer	–2 60 37	max.kicherer@e-technik.uni-ulm.de
Dipl.-Ing.	Roger King*	–2 60 40	roger.king@e-technik.uni-ulm.de
Dipl.-Ing.	Christoph Kirchner*	–2 64 54	christoph.kirchner@e-technik.uni-ulm.de
Dipl.-Ing.	Thomas Knödl	–2 60 38	thomas.knoedl@e-technik.uni-ulm.de
Dipl.-Ing.	Steffen Lorch	–2 60 39	steffen.lorch@e-technik.uni-ulm.de
M.S.	Safwat W.Z. Mahmoud	–2 60 44	safwat.mahmoud@e-technik.uni-ulm.de
Dipl.-Ing.	Ulrich Martin*	–2 60 46	ulrich.martin@e-technik.uni-ulm.de
Dipl.-Ing.	Felix Mederer	–2 60 37	felix.mederer@e-technik.uni-ulm.de
Dipl.-Phys.	Michael Miller*	–2 60 36	michael.miller@e-technik.uni-ulm.de
Dipl.-Phys.	Manfred Mundbrod	–2 60 39	manfred.mundbrod@e-technik.uni-ulm.de
Dipl.-Ing.	Barbara Neubert	–2 64 54	barbara.neubert@e-technik.uni-ulm.de
Dipl.-Ing.	Michael C. Riedl	–2 60 36	michael.riedl@e-technik.uni-ulm.de
Dipl.-Phys.	Fernando Rinaldi	–2 60 46	fernando.rinaldi@e-technik.uni-ulm.de
Dipl.-Ing.	Sven-Silvius Schad	–2 61 95	sven-silvius.schad@e-technik.uni-ulm.de
Dipl.-Ing.	Marcus Scherer	–2 61 95	marcus.scherer@e-technik.uni-ulm.de
Dipl.-Ing.	Eckart Schiehlen	–2 60 57	eckart.schiehlen@e-technik.uni-ulm.de
Dipl.-Ing.	Veit Schwegler*	–2 64 52	veit.schwegler@e-technik.uni-ulm.de

Dipl.-Phys.	Matthias Seyboth	–2 64 52	matthias.seyboth@e-technik.uni-ulm.de
Dr.-Ing.	Georgi Stareev	–2 64 53	georgi.stareev@e-technik.uni-ulm.de
Dipl.-Ing.	Heiko J. Unold	–2 60 36	heiko.unold@e-technik.uni-ulm.de
Dr.	Vincent Voignier	–2 60 35	vincent.voignier@e-technik.uni-ulm.de

Technical Staff

	Rainer Blood	–2 60 44	rainer.blood@e-technik.uni-ulm.de
	Susanne Döttinger*	–2 60 38	susanne.doettinger@e-technik.uni-ulm.de
	Susanne Menzel	–2 60 41	susanne.menzel@e-technik.uni-ulm.de
	Gerlinde Meixner	–2 60 41	gerlinde.meixner@e-technik.uni-ulm.de
	Sophie Pfetsch	–2 60 41	sophie.pfetsch@e-technik.uni-ulm.de
	Josef Theisz	–2 60 30	josef.theisz@e-technik.uni-ulm.de

* Member has left the department meanwhile

Preface

The year 2001 has again been very successful for the Optoelectronics Department. Among the achievements of the VCSEL group are the polarization control in a VCSEL using an etched elliptical surface relief that results in a polarization suppression ratio of 30 dB and two-dimensional high-power VCSEL arrays exhibiting a continuous-wave output power of 1.55 W at a record average emitted power density of 1.25 kW/cm^2. For our optically pumped semiconductor disk laser systems we achieved a continuous output power of 0.25 W at a wavelength of 980 nm in the fundamental mode with a coupling efficiency of more than 70 % into a single-mode fiber and we successfully realized intra-cavity frequency doubling resulting in 16 mW of blue-green laser emission. We also published a record value of 2.59 W for the continuous output power from a dry-etched mirror facet of a broad-area laser diode. More highlights of our research can be found in the various articles presented in the main part of this report.

In April 2001, Karl Joachim Ebeling, the former head of the department, left us for the intermediate period of 5 years and is now serving as Director of Research and Senior Vice President at Infineon Technologies. Consequently, Rainer Michalzik has assumed the project responsibilities for the VCSEL and datacom systems group. Markus Kamp has successfully achieved his habilitation degree with an excellent thesis on GaN-based light emitters and is now holding a leading management position in industry. Christoph Kirchner and Wolfgang Schmid obtained Ph.D. degrees from the Faculty of Engineering Science with theses on gas-phase epitaxy of AlGaInN and on high-efficiency LEDs, respectively. Furthermore, twelve Diploma Theses and Semester Projects have been carried out in the department.

As in recent years, our research has been performed in close cooperation with industrial partners. We also gratefully appreciate the financial support of national and European research organizations, which contribute the major part of our funding. Numerous publications at international conferences and a large number of articles in respected journals document the strong reseach activities of the department. A detailed list can be found at the end of this report.

Peter Unger Ulm, January 2002

Growth of GaAsSb/GaAs Double-Quantum-Well Lasers Emitting near 1.3 µm

Irene Ecker, Jürgen Joos, Susanne Menzel

Semiconductor gain media for the wavelength regime of 1.3 to 1.55 µm are intensively studied. For the development of surface emitting laser diodes active zones which can be grown pseudomorphic on GaAs substrate are of great interest. Fourteen GaAsSb/ GaAs edge emitting laser diodes are statistically analyzed. Furthermore we demonstrate broad area laser diodes with emission wavelength near 1.3 µm.

1. Introduction

For low-cost data transmission applications such as fiber to the home, local area networks and free-space optical interconnects vertical cavity surface emitting laser diodes (VCSELs) with emission wavelength of 850 nm are currently used. To develop metro access networks (MANs) manufacturable 1.3 to 1.55 µm VCSELs are desirable. VCSELs based on InP show poor characteristics because of low refractive index contrast and low material gain. Waferbonded structures are very complex to fabricate [1]. At the moment material systems suited for 1300 nm emission which can be grown on GaAs are intensively studied. A promising candidate seems to be GaAsSb. First structures could be realized lately under use of molecular vapor phase epitaxy (MOVPE) and gas source molecular beam epitaxy (GSMBE) [2]. We investigate the growth of edge emitting laser diodes with GSMBE.

2. Epitaxial Growth of Edge Emitting Laser Diodes

The epitaxial layers were fabricated in a modified Riber 32 P GSMBE. The active zone of the investigated edge emitting laser diodes consists of two 7 nm compressively strained GaAsSb quantum wells and a 30 nm thick GaAs barrier. The DQW (double quantum well) structure is surrounded by GaAs with a thickness of 40 nm. The active region is embedded in p- and n-doped AlGaAs cladding layers.

3. Statistics on Broad Area Laser Diodes

A statistical analysis of 14 devices which were grown under different growth conditions was carried out. To get information about the probable emission wavelength of the laser before processing the wafer into single devices, parts of the wafer were wet chemically etched in a sulphureous solution. The etch process was stopped short above the active zone of the diode. By nearly complete removal of the p-doped GaAs contact layer and the AlGaAs cladding it is possible to specify a peak wavelength of maximum intensity by photoluminescence measurements.

A) Influence of Wavelength on Photoluminescence Intensity

In fig. 1 the photoluminescence intensity versus peak wavelength is depicted. The antimony content of the quantum films varies between 16–32 %. This is tantamous to a compressive strain of GaAsSb to GaAs of 0.12–0.87 %. There are differences in intensity from 0.06 a. u. (at 1292 nm) to 100 a. u. (at 1140 nm). With increasing wavelength photoluminescence intensity decreases. The reason for this is probably a degradation of the semiconductor crystal caused by strain.

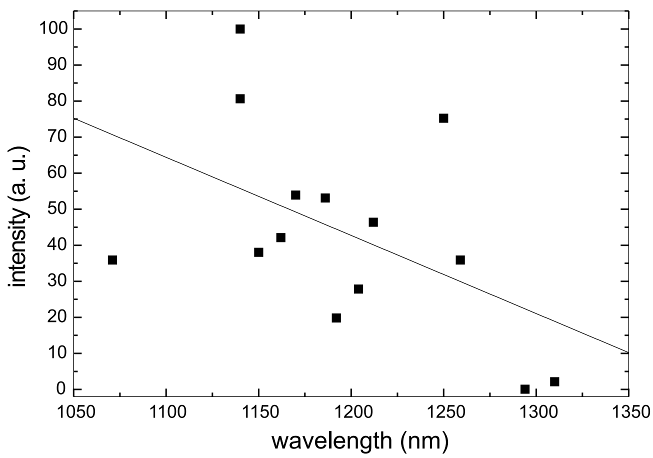

Fig. 1. Photoluminescence intensity versus wavelength.

B) Correlation between Wavelength Shift and Wavelength of Photoluminescence

It is typical for GaAsSb based laser diodes that laser oscillation occurs at a shorter wavelength in comparison to the peak wavelength of the corresponding photoluminescence spectrum. Responsible for this behaviour is the band lineup of GaAsSb in GaAs. In fig. 2 the calculated wavelength difference of photoluminescence measurement and laser oscillation dependend on wavelength of photoluminescence is shown. In general it is observed that laser oscillation occurs at shorter wavelengths compared with photoluminescence. The wavelength difference lies between minimum 4 nm (at 1170 nm) and maximum 38 nm (at 1250 nm). Unfortunately an increase in wavelength leads to a larger difference between wavelengths of photoluminescence and laser emission.

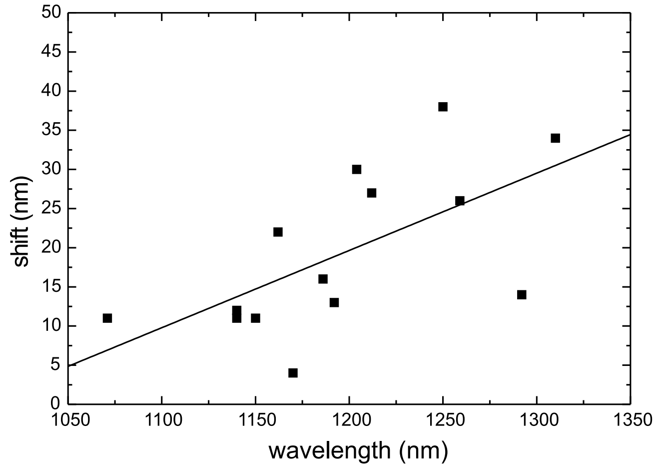

Fig. 2. Wavelength shift versus wavelength of photoluminescence.

C) Effect of Wavelength on Threshold Current Density

The correlation between threshold current density and laser emission wavelength demonstrates fig. 3. The threshold current densities span a range from 250 to 5670 A/cm^2. Again it is noticed that higher wavelength tends to result in an increase of threshold current density.

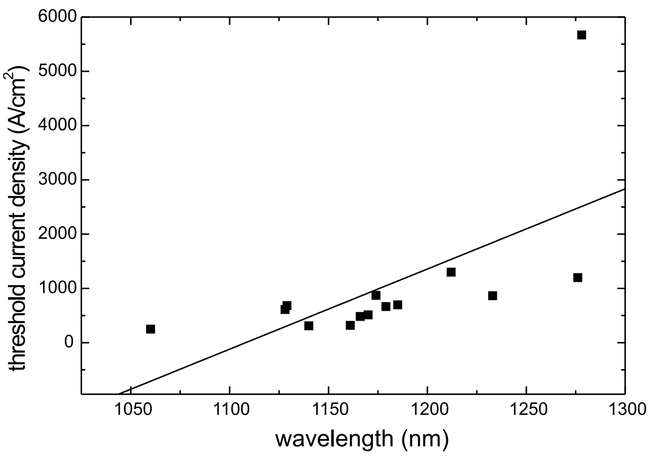

Fig. 3. Threshold current density versus laser emission wavelength.

4. Edge Emitting Laser Diodes in Continuous Wave and Pulsed Operation

By optimization of the epitaxial process it was possible to fabricate continuous wave working broad area laser diodes for the first time. Fig. 4 shows the output characteristic of a device with a width of 20 μm and a length of 800 μm. The threshold current density is 357 A/cm^2. The laser oscillates at a wavelength of 1161 nm (fig. 5).

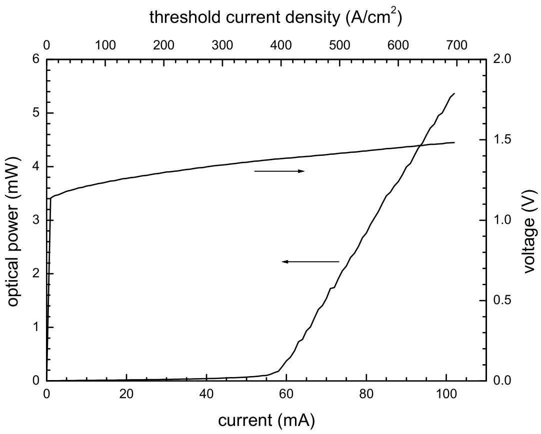

Fig. 4. Light output-current characteristics of GaAsSb/GaAs DQW laser diode under continuous wave operation.

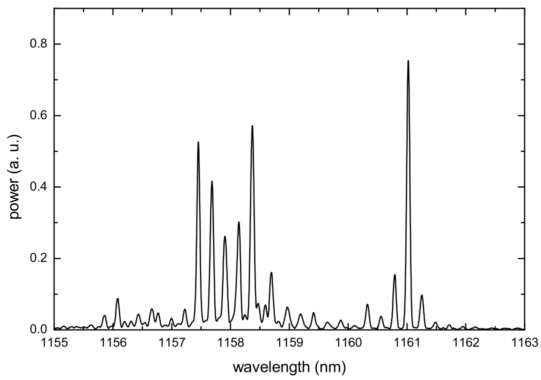

Fig. 5. Corresponding emission spectrum of GaAsSb/GaAs DQW laser diode.

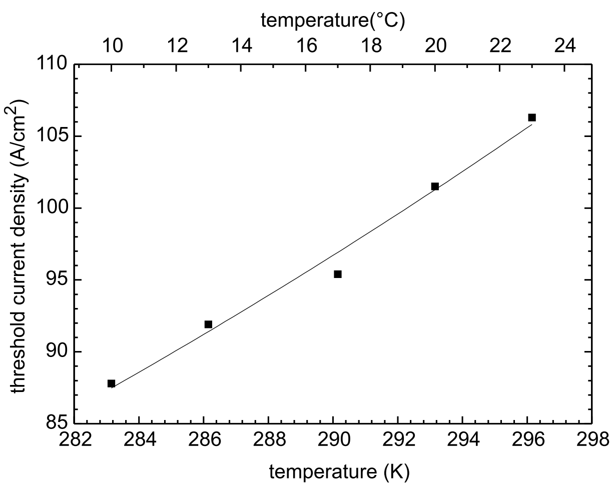

Fig. 6. Characteristic temperature of GaAsSb/GaAs DQW laser diode.

The temperature characteristic of the laser was measured within a range of 10 to 23 °C. Because of the dependency of the threshold current density on temperature a characteristic temperature T_0 of 68.3 K could be determined (fig. 6). This value agrees with the values published in literature [3], [4], [5]. This value is very low compared with InGaAs laser diodes. A reason might be the bad carrier confinement of electrons in the GaAsSb/GaAs system.

In fig. 7 the light output-current characteristic of a device with emission near 1300 nm is depicted. The diode works under pulsed operation. The pulse length is 50 ns and the repetition rate is 1 kHz. The threshold current density of the device is 1.5 kA/cm^2. The emission wavelength of the laser diode is located at 1276 nm (fig. 8). The corresponding peak wavelength obtained from a photoluminescence measurement is at 1310 nm.

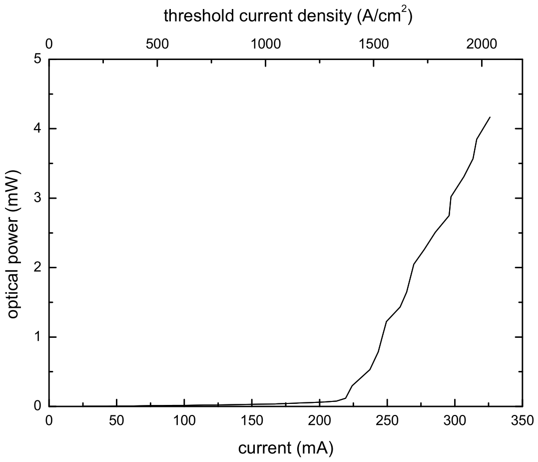

Fig. 7. Light output-current characteristics of GaAsSb/GaAs DQW laser diode under pulsed operation.

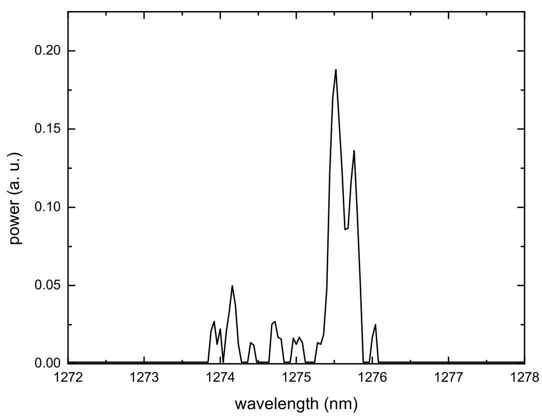

Fig. 8. Corresponding emission spectrum of GaAsSb/GaAs DQW laser diode.

5. Conclusion

A statistical analysis of 14 edge emitting laser diodes showed that increasing wavelengths lead to reduced photoluminescence intensity, an increase of wavelength shift between photoluminescence and laser emission and threshold current density.
A broad area laser diode under continuous wave operation was demonstrated for the first time (threshold current density 375 A/cm^2, laser emission at 1161 nm). Furthermore a device was fabricated with an emission wavelength of 1276 nm and a threshold current density of 1.5 kA/cm^2 under pulsed operation.
Further work will concentrate on the optimization of growth process of edge emitting laser diodes to achieve emission at 1.3 μm.

References

[1] K.D. Choquette, "The Race Toward Long Wavelength VCSELs," *IEEE/LEOS Ann. Meet. Conf. Proc.*, ISSN 1092-8081, 2001.

[2] M. Yamada, T. Anan, K. Kurihara, K. Nishi, K. Tokutome, A. Kamei, and S. Sugou, "High-performance 1.3 μm VCSELs with GaAsSb/GaAs quantum wells," *IEEE/LEOS Ann. Meet. Conf. Proc.*, ISSN 1092-8081, 2001.

[3] S.W. Ryu and P.D. Dapkus, "Low threshold current density GaAsSb quantum well (QW) lasers grown by metal organic vapour deposition on GaAs substrates," *Electron. Lett.*, vol. 36, pp. 1387–1388, 2000.

[4] O. Blum and J.F. Klem, "Characteristics of GaAsSb Single-Quantum-Well-Lasers Emitting near 1.3 μm," *IEEE Photon. Technol. Lett.*, vol. 12, pp. 771–773, 2000.

[5] M. Yamada, T. Anan, K. Tokutome, A. Kamei, K. Nishi, and S. Sugou, "Low-Threshold Operation of 1.3 μm GaAsSb Quantum-Well-Lasers Directly grown on GaAs Substrates," *IEEE Photon. Technol. Lett.*, vol. 12, pp. 774–776, 2000.

Three-Terminal Dual-Stage Vertical-Cavity Surface-Emitting Laser

T. Knödl and M. Golling

We have fabricated a three-terminal dual-stage VCSEL, operating continuous-wave (cw) at room temperature. Independent biasing of the two active stages leads to an extended singlemode regime compared to conventional VCSELs. The parallel configuration reveals singlemode operation with a differential series resistance of less than 35 Ω.

1. Introduction

The successful research into conventional vertical-cavity surface-emitting lasers (VCSELs) at 850 nm wavelength has led to mass-production of these devices for commercial short-distance high-speed and parallel optical data communication systems. Today, the research is mainly focused on the development of reliable 1.3 and 1.55 μm VCSELs but also on the realization and investigation of new design concepts to overcome the bottlenecks of standard VCSELs such as tunability [1], singlemode power [2], dynamic behavior [3] and roundtrip gain [4]. In this letter we present the experimental results on a fabricated three-terminal dual-stage p-n-p VCSEL at 980 nm wavelength. This approach offers the possibility to address several bottlenecks at once. The parallel configuration can reduce the series resistance at a similar threshold current as conventional VCSELs. The independent three-terminal design could allow active wavelength stabilization, an increase of singlemode power and may even lead to higher modulation frequencies.

2. Device Structure

Fig. 1 depicts a schematic cross-section of the selectively oxidized dual-stage VCSEL that is grown by molecular beam epitaxy. The device contains two active pn-junctions, each of which comprises three undoped 8 nm thick $In_{0.2}Ga_{0.8}As$ quantum wells separated by 10 nm thick GaAs barriers. Both active regions are placed in the antinodes of the standing wave pattern. The p-type top and bottom Bragg reflector stacks consist of 19 and 32 $Al_{0.9}Ga_{0.1}As$/GaAs layer pairs, respectively. Current confinement is achieved by mesa etching and subsequent selective oxidation of two 30 nm thick AlAs layers incorporated in the node of the standing wave pattern on each p-side of the cavity. The active regions are sharing a common ground intracavity contact placed in the middle of the about 1.3 μm thick n-type spacer. For the top stage, a ring contact is deposited on the mesa that allows

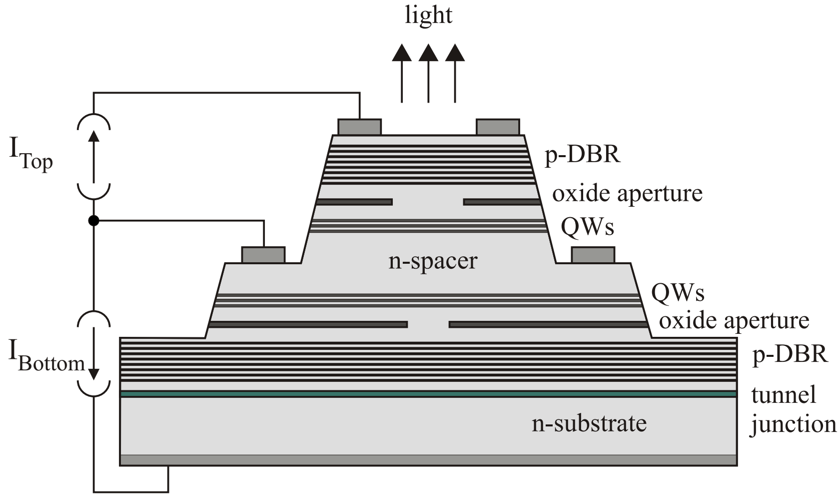

Fig. 1. Schematic cross-section of the dual-stage p-n-p VCSEL, fabricated in the (In)AlGaAs-GaAs material system.

for top surface emission. The bottom stage is connected by a full-area contact on the backside of the n-GaAs substrate. Thus, the three-terminal design offers the possibility to either drive the active stages in parallel with only one current source or independently from each other. In order to favor the growth on an n-type substrate, a highly doped reverse biased GaAs tunnel junction is placed between the bottom Bragg reflector and the substrate. For the p- and n-type doping we use C and Si, respectively.

3. Experimental Results

The successful fabrication of the p-n-p VCSEL is verified through the light versus current (L-I) curves in Fig. 2. The minimum total threshold current is about 2.3 mA and can be provided either in parallel driving mode or with various current ratios between top and bottom stage. For simplicity reasons, the results for independent biasing are reported only for the case of varying the current through the top active stage while maintaining various fixed pumping currents for the bottom stage. Similar results are obtained for the inverse contact configuration. It is seen that the pumping current levels of the bottom stage strongly influence the threshold of the driving stage and the output power of the VCSEL. The threshold current of the top active region decreases to about 0.5 mA with increasing current of the bottom stage. Further reduction is not observed for this sample because the design does not allow to optically bleach out one stage by electrically pumping the other in the regime of cw operation at room temperature. This is confirmed by biasing only the bottom active stage in pulsed mode ($I_{\mathrm{Top}} = 0\,\mathrm{mA}$) where the threshold of the laser is found at about 40 mA. The relatively high total threshold current of the dual-stage VCSEL in cw operation is, besides an unintended negative detuning, probably mainly caused by the 3.5 μm deviation of the oxide aperture diameters of top ($\sim$ 6.5 μm) and bottom stage ($\sim$ 3 μm). This is because the smaller aperture determines the lasing diameter of the

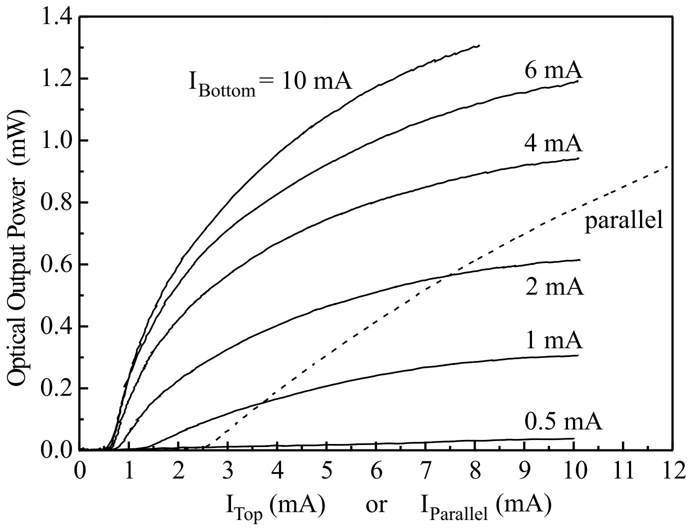

Fig. 2. CW room temperature L-I characteristics at various bias configurations of the dual-stage p-n-p VCSEL.

dual-stage VCSEL and therefore leads to carrier leakage in the larger aperture stage. On the one hand side, this could be prevented in an optimized structure with two identical apertures. On the other hand, two different oxide apertures offer the possibility of large effective area singlemode VCSELs. The dominance of the smaller oxide aperture with respect to transverse mode selection is suggested by optical spectrum measurements at various current levels. Changing the driving current in the large diameter top stage from 2 to 16 mA at a constant pumping current of 2 mA in the small diameter bottom stage gives no significant influence on the transverse mode behaviour, as shown in Fig. 3. Singlemode emission with a side-mode suppression ratio (SMSR) of more than 30 dB is preserved over the hole driving range. For comparison, the inset of Fig. 3 shows the optical spectrum of a conventional VCSEL with 5.5 μm aperture. The multimode behaviour is clearly seen at an already low injection level, in contrast to the dual-stage VCSEL with even larger diameter. Thus, the design with different apertures allows a significant extension of the singlemode regime for larger area lasers. Moreover, the parallel configuration of the dual-stage VCSEL reduces the total series resistance compared to conventional lasers. As seen in Fig. 4, the independently operated stages show series resistances of 70 and 50 Ω for the 3 μm bottom and the 6.5 μm top active region, respectively. These values are already very low compared to standard VCSELs and confirm the successful realization of a low resistivity intracavity contact. Driving the device in parallel, the total differential resistance decreases to about 32 Ω as expected. The inset of Fig. 4 shows the optical spectrum at a total current of 8 mA. Singlemode operation with a SMSR of more than 35 dB is observed. Thus, the dual-stage VCSEL design offers the possibility of singlemode devices with a differential series resistance of even less than 50 Ω.

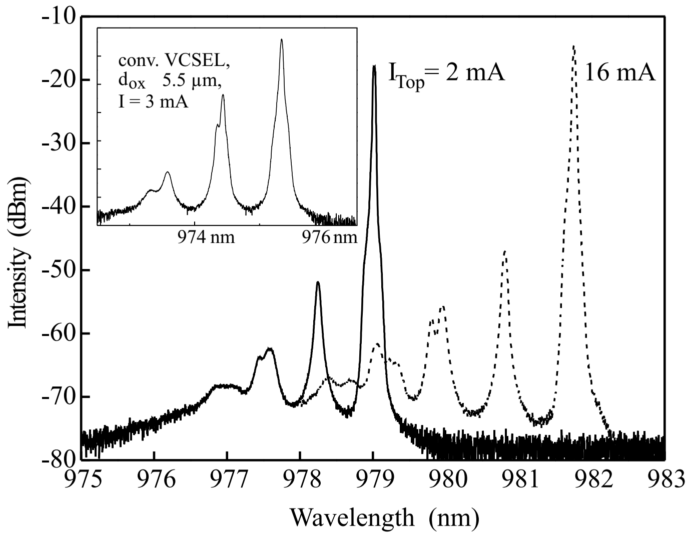

Fig. 3. Optical spectra of the dual-stage VCSEL at different top stage driving currents. The bottom stage current is fixed at 2 mA. The inset shows the spectrum of a conventional VCSEL with 5.5 μm aperture at 3 mA current on a 70 dB vertical and 4 nm horizontal scale.

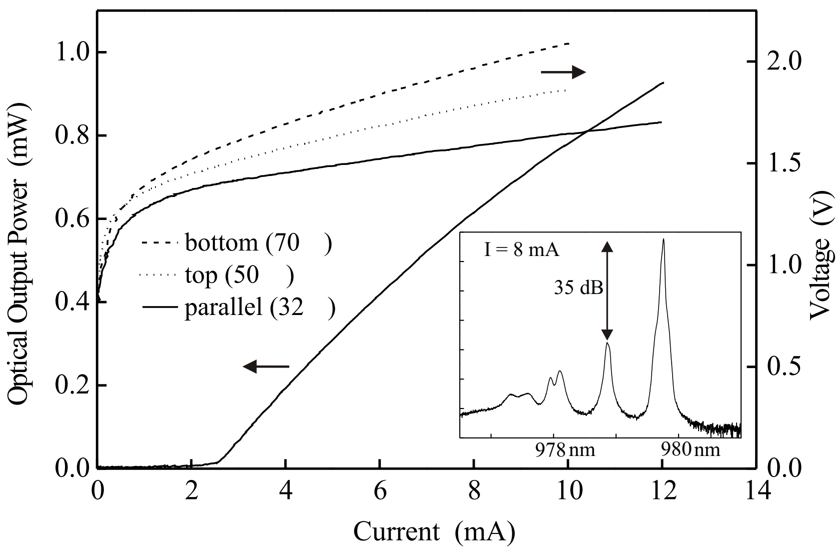

Fig. 4. L-I performance for parallel biasing and I-V characteristics for the independent and parallel driving configuration. The inset shows the optical spectrum at a current of 8 mA on a 70 dB vertical and 4.5 nm horizontal scale.

4. Conclusion

We have successfully fabricated a three-terminal dual-stage VCSEL where the active regions can be operated independently from each other or in parallel. The singlemode regime could be significantly extended with respect to conventional VCSELs due to different oxide apertures for the top and bottom stage. The differential series resistance of the singlemode VCSEL is reduced to $32\,\Omega$ in parallel driving configuration. Further work will include the investigation of active wavelength stabilization and modulation properties.

References

[1] C.J. Chang-Hasnain, "Tunable VCSELs," *IEEE J. Selected Topics Quantum Electron.* vol. 6, pp. 978–987, 2000

[2] H.J. Unold, S.W.Z. Mahmoud, F. Eberhard, R. Jäger, M. Kicherer, F. Mederer, M.C. Riedl, and K.J. Ebeling, "Large-Area Single-Mode Selectively Oxidized VCSELs: Approaches and Experimental," in Proc. *SPIE* vol. 3946, pp. 207–218, 2000

[3] J.A. Hudgings, R.J. Stone, C.-H. Chang, S.F. Lim, K.Y. Lau, and C.J. Chang-Hasnain, "Dynamic Behavior and Applications of a Three-Contact Vertical-Cavity Surface-Emitting Laser," *IEEE J. Selected. Topics Quantum Electron.* vol. 5, pp. 512–519, 1999

[4] T. Knödl, A. Straub, M. Golling, R. Michalzik, and K.J. Ebeling, "Scaling Behavior of Bipolar Cascade VCSELs," *IEEE Photon. Technol. Lett.* vol. 13, pp. 930–932, 2001

Polarization Control in VCSELs by Elliptic Surface Etching

Heiko J. Unold

We have fabricated 850 nm-wavelength VCSELs with an elliptical shallow surface relief having various aspect ratios and orientations. Using appropriate etch dimensions, VCSELs of up to 12.5 μm active diameter are forced to operate on the fundamental mode for a certain current range. By aligning the longer axis of the etched ellipse with the [011] *or* $[01\bar{1}]$ *crystal axes, the polarization of the fundamental mode is pinned accordingly with a polarization suppression ratio of about 30 dB.*

1. Introduction

Much attention has been given to the investigation of polarization in vertical-cavity surface-emitting lasers (VCSELs) [1]. Consequently, many approaches have been suggested to control the polarization state, more specifically to eliminate spontaneous polarization switching. These include elliptical mesas [2], misoriented substrates [3], external polarization selection elements [4], and more. However, these previous attempts are either rather difficult to implement, or do not provide sufficiently strong polarization selection for applications such as high-speed data transmission. Strong polarization selection with a simple method is desirable to achieve lowest noise for highest modulation speed, low susceptibility to polarization-sensitive loss or to enable polarization state selection e. g. to carry additional information. In this letter, we present the extension of our self-aligned surface-etching method, which has been very successful in fabricating large-area single-mode VCSELs [5, 6], to include elliptical surface etch patterns. This approach stabilizes single-mode emission and polarization simultaneously with one simple additional fabrication step.

2. Device Fabrication

The epitaxial structure consists of 34.5 n-Bragg pairs, three 8 nm GaAs quantum wells, a 30 nm $Al_{.98}Ga_{.02}As$ layer for selective oxidation and 27 p-Bragg pairs. An additional $\lambda/2$ $Al_{.1}Ga_{.9}As$ cap layer allows for the 50 nm deep surface etching without exposing high-aluminum content layers. To achieve anisotropic spatially varied loss, self-aligned surface etching [5] is carried out using elliptical etch patterns. The lithography mask includes ellipse orientations 0°, 30°, 45°, 60°, 90°, and 135° versus the [011] crystal axis with aspect ratios ranging from 1/2 to 1/4. Five device sizes with oxide apertures between 2.5 and 12.5 μm diameter have been fabricated. In this letter, we present the results of four selected devices whose fabrication parameters are given in Table 1. Consistent results have been obtained for the other devices.

Tab. 1. Fabrication parameters for the presented devices.

device	aperture diameter (μm)	short axis (μm)	long axis (μm)	angle to [011]
5_90	5.0	2.25	4.5	90°
5_45	5.0	1.95	5.9	45°
5_0	5.0	1.8	7.2	0°
5_U	5.0	unetched		

3. Measurement Results

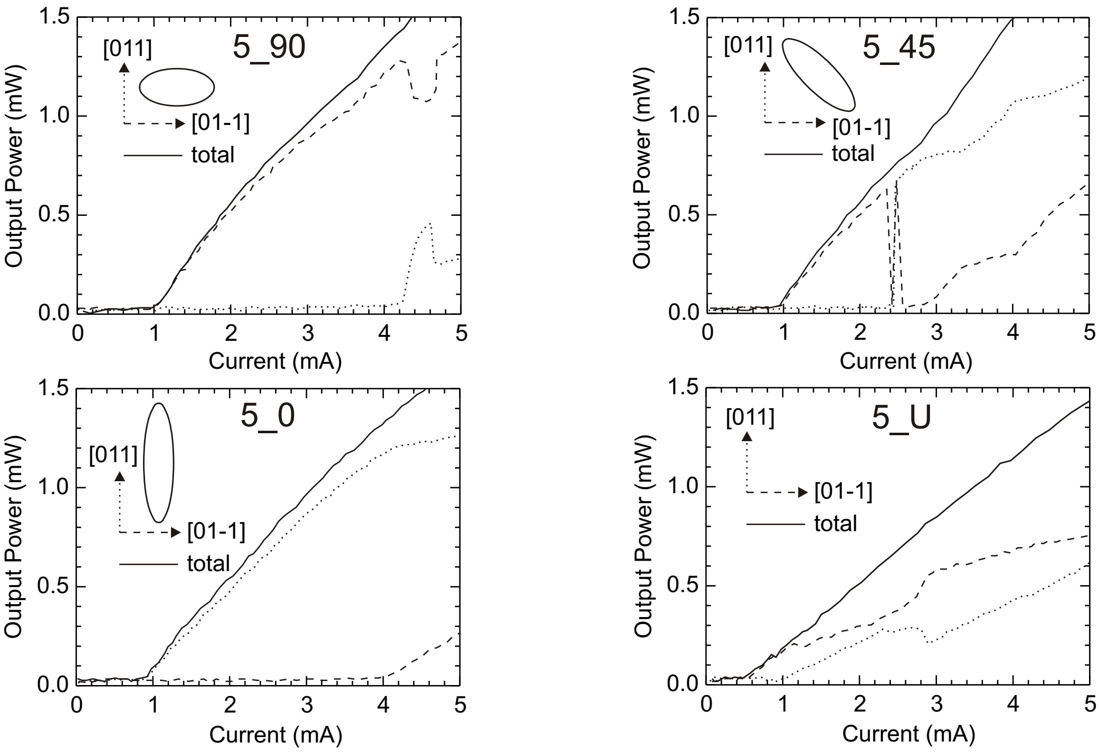

Fig. 1. Polarization-resolved LIV-characteristics of the four differently etched 5 μm aperture diameter devices. The insets illustrate orientation and aspect ratio of the etched ellipses.

The polarization-resolved LIV-characteristics of the four devices are shown in Fig. 1. No temperature control is employed for these devices held by vacuum on a copper block. As can be seen easily, the two devices 5_90 and 5_0 with ellipses oriented along the low-index crystal axes are forced to emit on the polarization parallel to the longer ellipse axis for the single-mode regime up to about 4 mA. Due to the surface etching, device 5_45 also displays an increased single-mode regime, but exhibits a polarization switch from $[01\bar{1}]$ to [011] at about 2.4 mA current. The unetched reference device 5_U only has a very small single-mode range with no significant polarization selection. For unetched devices of different aperture size, polarization switching can also be observed. A slight output power increase depending on the surface etch size can also be seen as previously reported in [6].

To confirm these results, a large number of devices has been tested using polarization resolved LIV-characteristics. Out of 58 5_90 devices and 62 5_0 devices, only 1 5_90 device exhibited switching, whereas only 5 5_U reference devices out of 60 measured did **not** switch polarizations. The polarization-resolved spectra in Fig. 2 taken at 3 mA confirm the strong polarization suppression of about 30 dB within the single-mode operation regime of device 5_90.

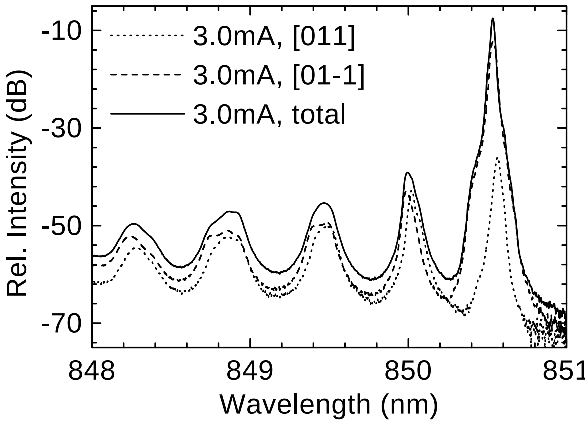

Fig. 2. Polarization-resolved spectra of device 5_90 for a current of 3 mA.

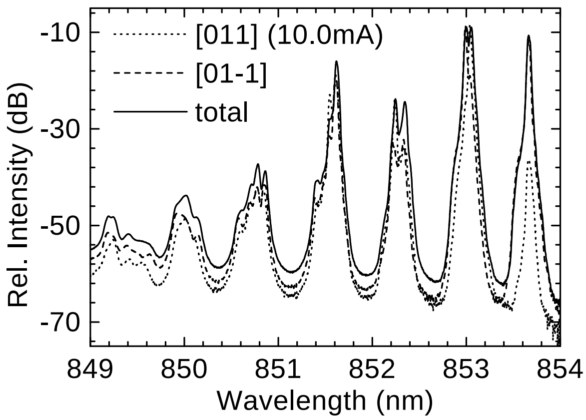

Fig. 3. Polarization-resolved spectra of device 5_90 for a current of 10 mA.

The spectral behavior of device 5_90 at a current of 10 mA, well into the multi-mode regime, is shown in Fig. 3. Even though higher-order modes contain various fractions of both polarizations, the fundamental mode polarization is still pinned to the $[01\bar{1}]$ crystal direction with a similar suppression ratio as before. This indicates that the polarization selection mechanism may be strong enough for applications like high-speed data transmission.

4. Conclusion

We have successfully fabricated for the first time 850 nm selectively oxidized VCSELs with a self-aligned elliptical shallow surface relief. CW measurements at room temperature with the bare die sample held by vacuum on a copper block have been carried out on a large number of devices. These measurements show deterministic polarization selection of the fundamental mode with about 30 dB suppression ratio over the complete operating range if the ellipse is aligned along the [011] or [01$\bar{1}$] crystal axis. By using a layer structure with lower p-side reflectivity in the future, we expect to much augment the effect, resulting in a much higher single-mode, single-polarization current range and optical output power. Additionally, the strength of the polarization pinning will be evaluated by applying mechanical strain, elevated temperatures and high-speed modulation.

5. Acknowledgement

This work is supported by the German Ministry for Research and Technology (BMBF). We wish to thank G. Steinle at Infineon Technologies, Munich for providing the epitaxial material.

References

[1] K. Panajotov, J. Danckaert, G. Verschaffelt, M. Peeters, B. Nagler, J. Albert, B. Ryvkin, H. Thienpont, and I. Veretennicoff, "Polarization Behavior of Vertical-Cavity Surface-Emitting Lasers: Experiments, Models and Applications," *Nanoscale and Nonlinear Optics: International School on Quantum Electronics*, in Proc. AIP, vol. 560, pp. 403–417, 2001.

[2] B. Weigl, M. Grabherr, C. Jung, R. Jäger, G. Reiner, R. Michalzik, D. Sowada, and K.J. Ebeling, "High-Performance Oxide-Confined GaAs VCSEL's," *J. Selected Topics Quantum Electron.*, vol. 3, no. 2, pp. 409–415, 1997.

[3] Y. Kaneko, D. Mars, S. Nakagawa, Y. Ichimura, and N. Yamada, "Vertical-Cavity Surface-Emitting Lasers with Stable Polarization Grown on (411)A-Oriented Substrates," *Jpn. J. Appl. Phys.*, vol. 38, no. 8A, pp. 864–866, 1999.

[4] C.-A. Berseth, B. Dwir, I. Utke, H. Pier, A. Rudra, V.P. Iakovlev, and E. Kapon, "Vertical cavity surface emitting lasers incorporating structured mirrors patterned by electron-beam lithography," *J. Vac. Sci. Technol. B*, vol. 17, no. 6, pp. 3222–3225, 1999.

[5] H.J. Unold, S.W.Z. Mahmoud, R. Jäger, M. Grabherr, R. Michalzik, and K.J. Ebeling, "Large-Area Single-Mode VCSELs and the Self-Aligned Surface Relief," *J. Selected Topics Quantum Electron.*, vol. 7, no. 2, pp. 386–392, 2001.

[6] H.J. Unold, M. Golling, F. Mederer, R. Michalzik, D. Supper, and K.J. Ebeling, "Singlemode output power enhancement of InGaAs VCSELs by reduced spatial hole burning via surface etching," *Electron. Lett.*, vol. 37, pp. 570–571, 2001.

Improved Output Performance of High-Power VCSELs

Michael Miller and Ihab Kardosh

The intention of this paper is to report on state-of-the-art high-power vertical-cavity surface-emitting laser diodes (VCSELs), single devices as well as two-dimensional arrays. Both approaches are studied in terms of electro-optical characteristics, beam performance and scaling behavior. The maximum cw output power at room temperature of large-area bottom-emitting devices with active diameters up to 320 μm is as high as 0.89 W which is to our knowledge the highest value reported for a single device. Measurements under pulsed conditions show more than 10 W optical peak output power. Also the cw performance of two-dimensional arrays has been increased from 0.56 W for 23 elements [1] up to 1.55 W for 19 elements due to significantly improved heat sinking. The extracted power densities spatially averaged over the area close to the honeycomb like array arrangement raised from 0.33 kW/cm^2 to 1.25 kW/cm^2.

1. Introduction

Small diameter VCSELs are accepted devices for datacom applications due to their distinguished performance. One of those is the high conversion efficiency of more than 40 % which is also a basic for high-power devices. But most of the datacom VCSELs have output powers in the range of a few mW. For higher powers edge-emitting lasers are more suited because they achieve up to several W at high conversion efficiencies [2],[3]. Disadvantages of these devices are the strongly elliptical beam with a large divergent far-field angle in the fast axis and the high effort in testing and mounting. To close the gap between low power datacom VCSELs and high power edge-emitting lasers large-area single device VCSELs [4] and two-dimensional arrays [5] have been investigated. More than 2 W at -1°C heat sink temperature are reported from a VCSEL array consisting of a large number of 1000 single elements resulting in a chip area averaged power density of 30 W/cm^2. Our aim is to fabricate devices which combine high optical output powers in the Watt regime, high conversion efficiencies above 20 % and high power densities of more than 1 kW/cm^2 in cw-operation at room temperature. Therefore a layout with high packing densities and optimized number of elements is performed. As carried out in this previous work [1], large-area top-emitting VCSELs are not suited because of the decreasing efficiencies with increasing device size and the poor beam quality due to the ring-shaped near field caused by the inhomogeneous carrier injection through the top ring contact. Therefore we have concentrated the work on bottom-emitting devices which provide a homogeneous current injection also for large-area devices and are suited for a sophisticated mounting technique.

2. Device Structure

The fabrication of bottom-emitting single devices and two-dimensional arrays is very similar. The layer structure is grown by solid-source molecular beam epitaxy on GaAs-substrate. A schematic cross-sectional view of a VCSEL array is shown in Fig. 1. The

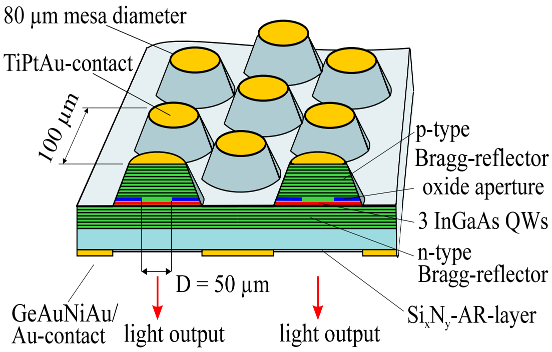

Fig. 1. Cross-sectional view of the oxidized VCSEL array.

carbon doped p-type Bragg reflector consists of 30 pairs of $Al_{0.9}Ga_{0.1}As/GaAs$ layers. The active region is composed of three 8 nm thick $In_{0.2}Ga_{0.8}As$ quantum wells for an emission wavelength of about 980 nm. Above the p-type cladding layer a 30 nm thick AlAs layer is inserted. Wet chemically etching with sulphuric acid is used to define mesa type active regions. The exposed AlAs layer is laterally oxidized in a water vapor atmosphere using nitrogen as carrier gas at a temperature of 410°C in order to form the current aperture and determine the active diameter of the device. For light emission through the GaAs substrate the silicon doped n-type distributed Bragg reflector has only 20 layer pairs of the same composition as the p-type mirror. On top of the mesa a full size p-contact consisting of Ti/Pt/Au is evaporated which provides a homogeneous current distribution and serves as a wettable metal pad for soldering. After mechanically polishing the GaAs substrate down to a thickness of 150 μm, an anti-reflection coating of Si_3N_4 with refractive index of 1.89 and quarter-wavelength thickness is deposited using plasma enhanced chemical vapor deposition. The Si_3N_4 layer is opened selectively with reactive ion etching for Ge/Au/Ni/Au large-area contacts surrounding the emission windows. After annealing the n-type contact at 400°C the processing is completed by depositing an electroplated Au layer of 1-2 μm thickness.

3. Mounting on Heat Sinks

VCSELs with active diameters up to 100 μm can be operated without mounting on heat sinks and are generally capable for on-wafer-testing of electro-optical device performance like threshold current density, threshold voltage, differential resistance, differential efficiency and emission wavelength. Due to a slight gradient in layer thickness across the grown wafer and corresponding detuning of gain and cavity resonance device performance depends on wafer position. Only large active diameter VCSELs with matched gain and cavity resonance are suited for highest output powers since not optimized detuning increases threshold current and dissipated power drastically. On-wafer-tests are performed in order to select appropriate large-area devices or arrays for mounting. The standard mounting technique shown in Fig. 2 is the same for single devices and for two-dimensional arrays.

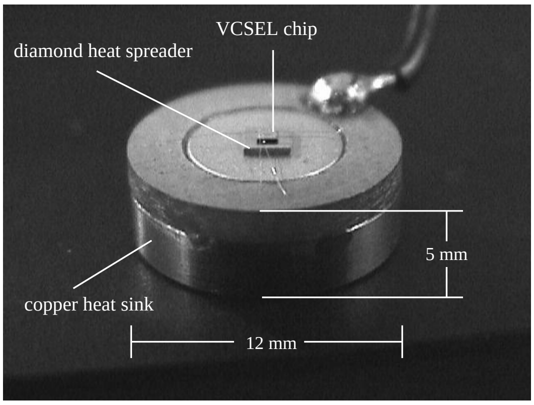

Fig. 2. Mounted semiconductor chip on metallized diamond and copper heat sink.

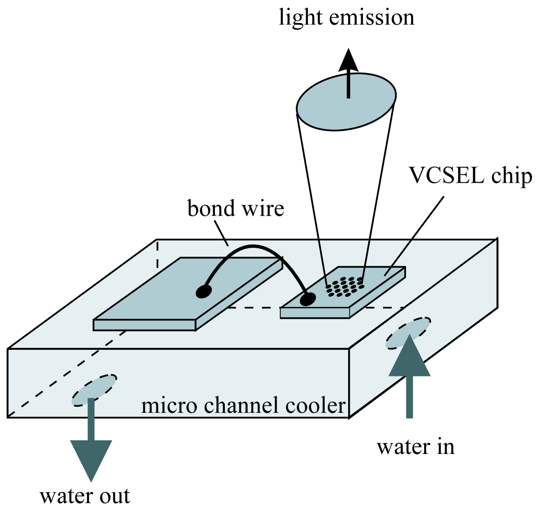

Fig. 3. Schematic drawing of a mounted semiconductor chip on a water cooled copper submount.

The cleaved semiconductor chip with dimensions between 0.5 × 0.5 mm^2 (single device) and 0.8 × 0.8 mm^2 (two-dimensional arrays) is soldered junction-down with eutectic $Au_{80}Sn_{20}$-solder on a metallized diamond heat spreader of 2 × 2 mm^2 size. The same AuSn solder is used to attach the diamond on a small copper heat sink. Soldering is achieved in a single-step heating process at a temperature of about 300°C. The cylindrical copper mount has a diameter of 12 mm and a height of 5 mm. In the backside a thread is cut for easy mounting on a larger heat sink. Heat dissipation predominantly occurs through the p-type contact. For the two-dimensional arrays the p-contact is common for all devices after mounting. Therefore a good homogeneity of the electrical parameters for all devices across the array is required.

As an alternative heat sink a microchannel cooler has also been employed for two-dimensional arrays as indicated in Fig. 3. The thickness of the water cooled copper-plate where the array is soldered onto is about 0.4 mm and the thickness of the indium solder is about 3 μm. To reduce costs the semiconductor chip is mounted without diamond heat spreader. The thermal strain on the devices during soldering is reduced because the melting point of indium is only about 160°. Both solders are generally applied and tested for high-power edge-emitting lasers. The mounting can be done automatically by pick-and-place machines because alignment tolerances are much more relaxed compared to edge-emitting lasers. The electrical connections are done via wire-bonding.

4. Large-Area Single Devices

In Fig. 4 the output characteristics for 3 different device sizes of 170, 245 and 320 μm are shown. The threshold currents are 215 mA, 465 mA and 1.1 A, respectively. This corresponds to a threshold current density of 1 kA/cm^2. The maximum output powers are 450 mW, 740 mW and 890 mW. The highest value we have obtained before was 350 mW for a device with 200 μm active diameter [6]. In comparison to these results, the mounting technique has improved drastically. Various applications like free space data transmission, optical sensoring or LIDAR request pulsed operation. Therefore the capability of the largest device has been investigated. The electrical pulses had a width of approximately 10 ns and a repetition rate of 67 kHz. The optical pulses for different laser currents are slightly wider as can be seen in Fig. 5 due to reflections in the supply cables between the current source and the laser.

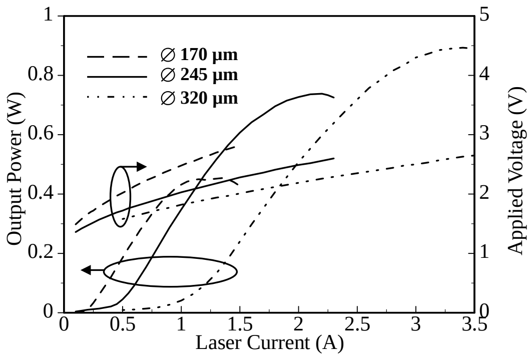

Fig. 4. Output characteristics for large-area single devices with 170, 245 and 320 μm active diameter.

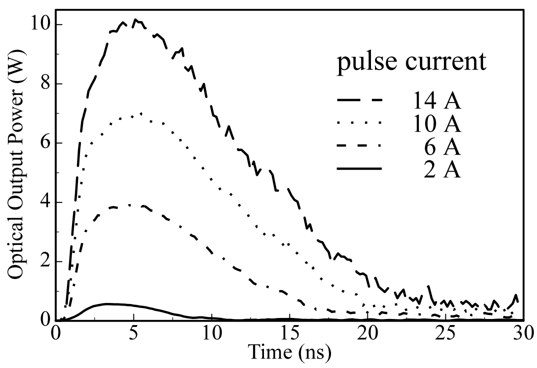

Fig. 5. Optical pulses measured by a fast photodiode at different laser currents. The width of the electrical pulses was about 10 ns and the repetition rate 67 kHz.

The maximum peak output power of 10 W is achieved at a current of 14 A which was the limit of the current source. At this point a current density of 17.5 kA/cm^2 is present and there are still no thermal effects observable.

In VCSELs with small active diameters of around 5 μm current densities at thermal rollover of more than 50 kA/cm^2 are applied so peak output powers in the range of 30 W seem to be possible.
Due to the large active diameter the emitted light is strongly multi-mode. To measure the spectrum of these VCSELs one have to ensure that all light is detected in a spectrum analyzer. Therefore the coupling into a small core diameter fiber of e.g. 50 μm is not reasonable because mode filtering would occur. To avoid errors in measuring we coupled the light into a 600 μm core diameter silica fiber with a numerical aperture of 0.37. The disadvantage of this setup is the low resolution of the analyzer which is about 0.5 nm. The mode spacing is in the range of a few picometer so single modes can not be observed

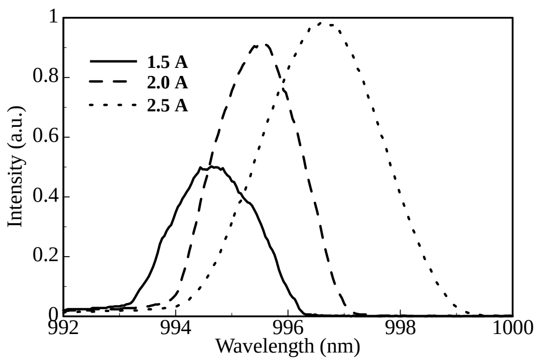

Fig. 6. Spectra of the 320 μm active device for different laser currents.

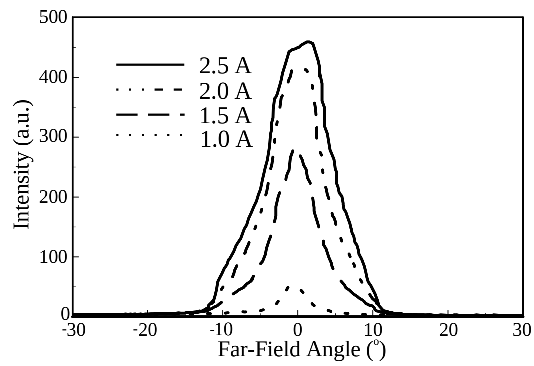

Fig. 7. Far-field measurements of the 320 μm active device for different laser currents.

and the shape of the spectrum is smooth in comparison to small VCSELs as can be seen in Fig. 6. The peak-wavelength is in the range of 995 nm due to the cavity resonance which can be designed for wavelengths between 940 nm and 1020 nm by changing the thickness of the DBR layer pairs. The full width at half maximum of the spectra is lower than 5 nm for all currents which is useful for applications like pumping of Er- or Yb-doped fibers and Nd-YAG microdisk lasers. The far-field of this laser is shown in Fig. 7 again for different laser currents. The graph shows a single lobe with a FWHM of less than 12° for all currents and no side-lobes or amplified spontaneous emission (ASE) are observed. Due to the circularly symmetric far-field pattern the beam can easily be focused or collimated by one usual lens. In comparison to edge-emitting lasers the low divergent beam is astigmatism free and shows no filamentations.

5. Two-Dimensional VCSEL Arrays

Criteria for optimized array design were discussed in previous works [1],[7]. First arrays consisted of 23 elements with active diameters between 30 - 40 μm and center-to-center spacings between 70 - 90 μm. For an active diameter of 40 μm and a spacing of 90 μm this results in maximum output powers of 0.56 W in cw-operation at room temperature and 0.8 W at -10°C. The corresponding power densities spatially averaged over the cleaved semiconductor chip are 0.33 and 0.47 kW/cm^2, respectively. In order to obtain maximum optical output power at high power densities, the number of elements was first reduced to 19 individual devices again arranged in a honeycomb-like layout with a mesa diameter of 80 μm and an active diameter of 40 μm defined by oxidation of the current aperture. The center-to-center spacing of neighboring elements is 100 μm and the area close to the honeycomb-like arrangement of the lasers is about 0.123 mm^2 as can be seen in Fig. 8 from the white line. The array was soldered on a microchannel cooler as shown in Fig. 3 and tested in cw-operation at 18°C water temperature. Due to the fact that all devices are driven in parallel after mounting the threshold current is 285 mA which corresponds to 19 times the threshold of a single device. The maximum output power is 0.97 W which

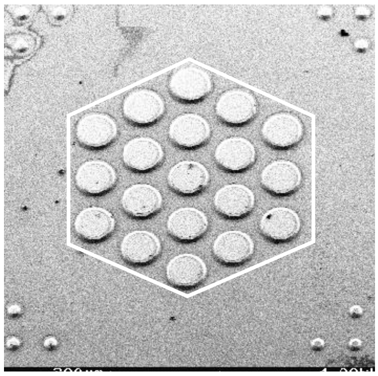

Fig. 8. Top view of the array with wet chemically etched mesas. The white line is drawn to indicate the effective area of the array.

corresponds to a spatially averaged power density of 0.81 kW/cm^2 over the effective chip area shown in Fig. 8 [8].

After optimization of the mounting technique and heat sinks, the active diameter was increased to 50 μm in order to increase the maximum output power and the array were mounted on both kinds of heat sinks, diamond heat spreader combined with a copper heat sink as well as microchannel cooler.

The differential resistance of the arrays with 50 μm active diameter mounted on diamond heat spreader combined with a copper heat sink is reduced to 0.48 Ω which, due to some additional ohmic losses caused by the soldering, is slightly above the value expected for the given parallel connection. Fig. 9 shows the output characteristics of the array at different heat sink temperatures. The threshold current is decreased for lower temperatures indicating a slightly negative detuning of the gain peak with respect to the cavity resonance at room temperature. Maximum output power is as high as 1.08 W for a heat sink temperature of 18°C and increases to 1.4 W at 10°C. The maximum cw power density at 10°C exceeds 1 kW/cm^2 if a spatial average is taken over the area close to the honeycomb-like arrangement as indicated in Fig. 8. Maximum conversion efficiencies are above 20 % over the whole temperature range with corresponding optical output powers between 0.6 W for 18°C and 0.8 W for 10°C.

The LIV-characteristics of an array mounted on the water cooled heat sink is given in Fig. 10. The water temperature again is 18°C and the maximum output power is as high as 1.55 W which corresponds to a power density of 1.25 kW/cm^2. The higher output power in comparison to the array described above is mainly due to a better heat-sinking and heat removal by the water cooled submount.

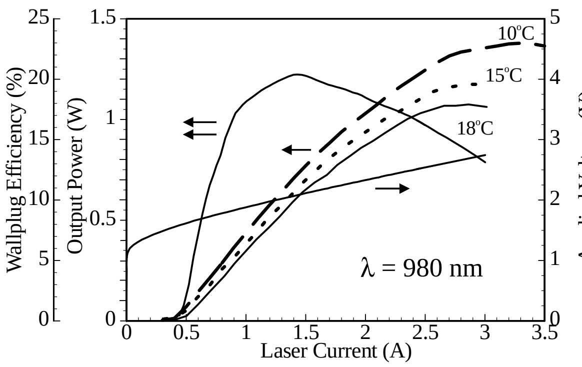

Fig. 9. Output characteristics of the mounted array under cw operation at different heat sink temperatures.

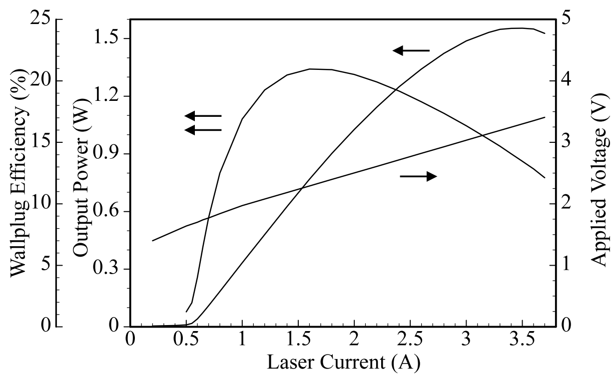

Fig. 10. LIV-characteristics and wallplug efficiency of a VCSEL array with active diameters of 50 μm mounted on a water cooled heat sink.

Since both arrays are from the same wafer and have similar electro-optical characteristics from on-wafer testing the output power is only depending on the mounting. This is also obvious from a simulation of the output characteristics. The calculated thermal conductivities λ_c of the modules achieved from a model, which is rather simple and described in detail in [1], are 320 W/(K·m) for the diamond/copper-submount and 400 W/(K·m) for the water cooled submount. This value is 8, respectively 10 times higher compared to devices with AlGaAs-material compositions tested on wafer without heat-sinking. A detailed study of the thermal properties has to be done in future with FEM-simulations.

6. Conclusion

In conclusion we have fabricated high-power VCSELs, single devices as well as two-dimensional arrays with proven potential for applications requiring output power in the Watt-regime. The single devices with active diameters up to 320 μm show output powers up to 0.89 W which is up to now the highest value reported. The arrays consisting of 19 elements with an individual active diameter of 50 μm and a spacing of 100 μm which are arranged in a dense honeycomb pattern achieve output powers of 1.55 W corresponding to a spatially averaged power density of 1.25 kW/cm^2 over the effective array chip size. Favorable beam profiles with low divergence angles and a high reliability of over 10.000 hours are remarkable characteristics that recommend for the implementation of VCSELs as high-power lasers. The wavelength is at the moment restricted between 900 and 1020 nm but further investigations in mounting and substrate removal will enable emission wavelengths down to about 800 nm where 808 nm is the desired pump wavelength for the Nd-YAG crystal. Future work is expected to result in modules with optical output powers of about 10 W in cw operation through increasing the number of elements and a further improved mounting technique.

References

[1] M. Grabherr, M. Miller, R. Jäger, R. Michalzik, U. Martin, H. Unold, and K.J. Ebeling, "High-Power VCSEL's: Single devices and densely packed 2-D-arrays," *IEEE J. Select. Topics Quantum Electron.*, vol. 5, pp. 495–502, 1999.

[2] A. Al-Muhanna, L.J. Mawst, D. Botez, D.Z. Garbuzov, R.U. Martinelli, and J.C. Connolly, "High-power ($>$ 10 W) continuous-wave operation from 100-μm-aperture 0.97-μm-emitting Al-free diode lasers," *Appl. Phys. Lett.*, vol. 73, pp. 1182–1184, 1998.

[3] J. Braunstein, M. Mikulla, R. Kiefer, M. Walther, J. Jandeleit, W. Brandenburg, P. Loosen, R. Poprawe, and G. Weimann, "267 W cw AlGaAs/GaInAs Diode Laser Bars," in *Laser Diodes and LEDs in Industrial, Measurement, Imaging, and Sensors Applications II; Testing, Packaging, and Reliability of Semiconductor Lasers V*, Proc. SPIE, vol. 3945, pp. 17-22, 2000.

[4] F.H. Peters, M.G. Peters, D.B. Young, J.W. Scott, B.J. Thibeault, S.W. Corzine, and L.A. Coldren, "High power vertical-cavity surface-emitting lasers," *Electron. Lett.*, vol. 29, pp. 200-201, 1993.

[5] D. Francis, H.-L. Chen, W. Yuen, G. Li, and C. Chang-Hasnein, "Monolithic 2D-VCSEL array with 2 W CW and 5 W pulsed output power," *Electron. Lett.*, vol. 34, pp. 2132-2133, 1998.

[6] M. Grabherr, R. Jäger, M. Miller, C. Thalmaier, J. Heerlein, R. Michalzik, and K.J. Ebeling, "Bottom-Emitting VCSEL's for high-cw optical output power," *Photon. Technol. Lett.*, vol. 10, pp. 1061–1063, 1998.

[7] M. Grabherr, M. Miller, R. Jäger, R. Rösch, U. Martin, H. Unold, and K.J. Ebeling, "Densely Packed High Power VCSEL Arrays," in *Proc. ISLC 1998*, vol. 1, pp. 245–246, (Nara, Japan), Sep. 1998.

[8] M. Grabherr, M. Miller, R. Jäger, and K.J. Ebeling, "Reliable 1 W cw VCSEL module for high optical power density," in *Proc. LEOS Annual Meeting 1999*, vol. 1, pp. 265–266, (San Francisco, USA), Nov. 1999.

Up to 10 Gbit/s Data Transmission with 1.3 μm Wavelength InGaAsN VCSELs

Felix Mederer and Gunther Steinle*
* Infineon Technologies AG, München, Germany

We demonstrate room-temperature data transmission with monolithic InGaAsN/GaAs VCSELs, emitting maximum single-mode optical power of 700 μW at 1304 nm wavelength. Bit error rates of less than 10^{-12} have been achieved for transmission over 20.5 km standard single-mode fiber and 500 m multi-mode fiber at 2.5 Gbit/s and back-to-back transmission at 10 Gbit/s.

1. Introduction

850 nm wavelength vertical-cavity surface-emitting lasers (VCSELs) are currently used as transmitters for short-distance optical links like Gigabit Ethernet or parallel optical links such as PAROLI™ [1]. High beam quality, easy array scaling, on-wafer testability, low power consumption, easy packaging, comparatively low production cost [2] and high-speed modulation capability [3] promote the use of VCSELs for short-distance multi-mode fiber (MMF) based interconnects. At an emission wavelength of 1.3 μm eye-safety restrictions are relaxed compared to 850 nm and standard single-mode silica fibers (SSMF) with higher bandwidth-length products can be used for km-long links in local and metropolitan area networks. By incorporating only 1.8 % fraction of nitrogen into the active quantum wells (QWs), direct band gaps suitable for 1.3 μm transmission can be achieved within the well-known InGaAs/GaAs material system [4]. Thus both high-quality AlGaAs/GaAs distributed Bragg reflectors and the active region can be grown monolithically on GaAs substrates [5, 6, 7]. In this paper we present devices with new record performance as well as data transmission experiments at 2.5 Gbit/s, 5 Gbit/s, and 10 Gbit/s.

2. InGaAsN VCSEL Properties

The active region consists of two 6.5 nm thick InGaAsN QWs which contain about 35 % indium and 1.8 % nitrogen and are separated by 20 nm thick GaAs barriers. We use undoped mirrors and two intracavity contact layers doped with silicon or beryllium for lateral current supply. Current confinement is achieved through a single 15 nm thick AlAs layer incorporated into the p-doped GaAs spacer, which is selectively oxidized to an aperture size of about $4{\times}6$ μm². The dry-etched top-mesa with a diameter of 15 μm

Fig. 1. Output characteristics of a $4{\times}6\ \mu\mathrm{m}^2$ active area single-mode selectively oxidized InGaAsN VCSEL.

consists of 28 pairs of AlGaAs/GaAs. The diameter of the wet-chemically etched lower mesa is 35 μm. Further details of the structure can be found in [7]. As seen from the continuous wave (CW) output characteristics in Figure 1, the threshold current is 1.9 mA. The maximum output power at room temperature is 700 μW at a driving current of 10 mA. The differential series resistance has a nearly constant value of 280 Ω until thermal roll-over.

Fig. 2. Spectra at CW and modulated operation with V_{pp}=1 V at 6 mA bias current.

The lasing wavelength shifts from 1302.5 nm at an operation current of 2 mA to 1306.1 nm at 10 mA. Single-mode and single-polarization emission is maintained at a side-mode suppression ratio of more than 35 dB up to a driving current of 9 mA. At 6 mA bias and digital modulation with V_{pp}=1 V the laser also remains single-mode and shows only a wavelength shift of 0.1 nm versus CW mode as shown in Figure 2.

3. Dynamic Properties and Data Transmission Results

From small-signal modulation measurements as indicated in Figure 3 we have deduced a modulation efficiency of 3.7 GHz/$\sqrt{\text{mA}}$ and a maximum 3 dB modulation frequency of 5.4 GHz at a driving current of 7 mA.

Fig. 3. Small-signal frequency response of a 4×6 μm^2 active area InGaAsN VCSEL for various bias currents.

Transmission experiments have been carried out at 2.5 Gbit/s with a pseudo-random bit sequence (PRBS) of $2^7 - 1$ word length. The VCSEL was biased at 6 mA and modulated with 1 V_{pp} from a 50 Ω impedance driver, corresponding to an average output power of –4 dBm and a measured optical extinction ratio of 6.4 dB. An avalanche germanium photodetector with a bandwidth of 2 GHz was employed for detection

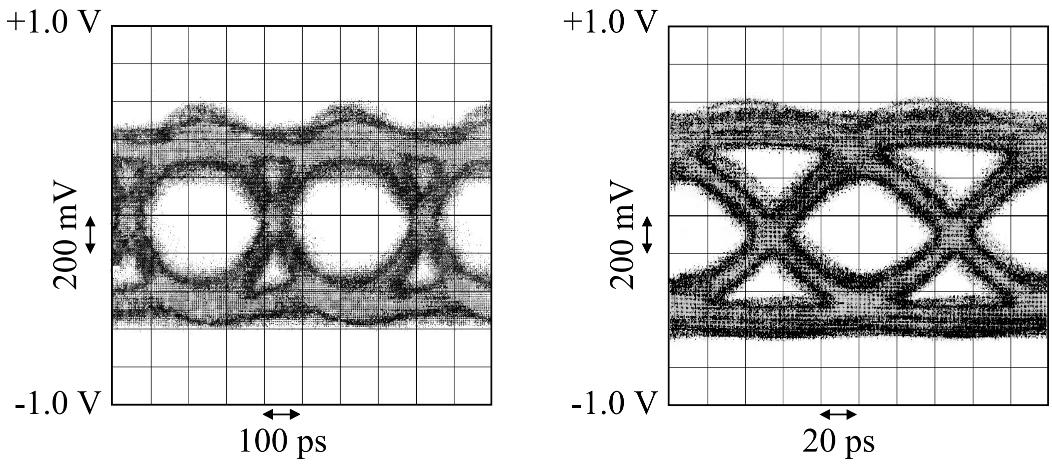

Fig. 4. Eye diagrams recorded for a BER of 10^{-12} after 20.5 km SSMF transmission with 2.5 Gbit/s data rate (left) and for BTB testing with 10 Gbit/s (right).

The eye diagrams in Figure 4 are wide open and symmetric and are displayed for transport of 2.5 Gbit/s data rate over 20.5 km SSMF (left) and 10 Gbit/s for back-to-back (BTB) transmission (right). Minimum measured bit error rates (BER) are below 10^{-12} as shown in Figure 5. For BTB transmission at 2.5 Gbit/s data rate the minimum received optical power for a BER of 10^{-12} is –29.0 dBm and since fiber dispersion is negligible at 1.3 μm, the measured power penalty after 20.5 km of SSMF is only 0.5 dB compared with 4.5 dB power penalty for transmission over 500 m MMF with 50 μm core diameter. For 5 Gbit/s transmission, an InGaAs pin-diode with 9 GHz bandwidth together with a suitable 3 GHz Bessel filter was used. Again the VCSEL was driven with 6 mA bias current and 1 $V_{\rm pp}$ which leads to an optical extinction ratio of 6 dB. For BTB and 10 km SSMF transmission with a BER of 10^{-12}, the minimum received optical power is –19.1 dBm and –18.5 dBm, respectively. Without 3 GHz filtering we were able to demonstrate 10 Gbit/s BTB transmission. In order to obtain the necessary modulation frequency range, the bias current had to be increased to 8 mA. As inferred from Figure 5 for a BER of 10^{-12}, a minimum received optical power of –10.4 dBm is necessary. Unfortunately, under modulation at 8 mA bias current, the donut-shaped next order transverse mode is excited, prohibiting a suitable transmission over the single-mode fiber.

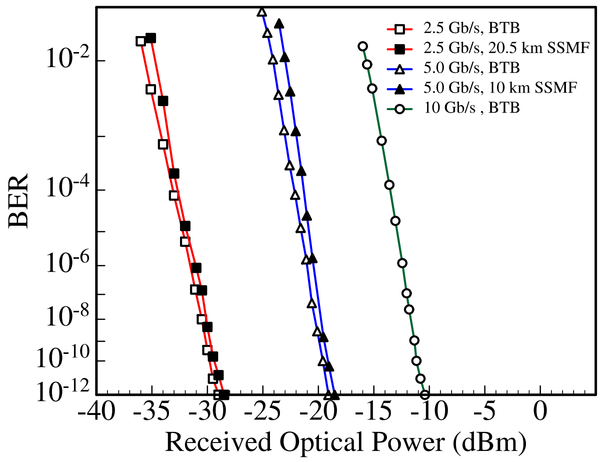

Fig. 5. BER characteristics for $2^7 - 1$ word length PRBS 2.5 Gbit/s data rate transmission over 500 m MMF, 20.5 km SSMF and for BTB testing, 5 Gbit/s BTB and over 10 km SSMF and 10 Gbit/s BTB.

4. Conclusion

We have fabricated and characterized new monolithic InGaAsN VCSELs emitting single-mode at 1.3 μm wavelength. The devices are suitable for error-free data transmission at 2.5 Gbit/s, 5 Gbit/s, and 10 Gbit/s over distances of 20.5 km SSMF, 10 km SSMF, and BTB, respectively. At a data rate of 2.5 Gbit/s, we have also compared the transmission behavior between 500 m MMF and 20.5 km SSMF. All presented results clearly demonstrate the excellent prospects of 1.3 μm wavelength VCSEL sources as the key elements for low-cost datacom applications.

5. Acknowledgment

The authors would like to acknowledge the support of G. Kristen, and H. Riechert from Infineon Technologies AG, Otto-Hahn-Ring 6, D-81730 Munich, Germany and of A.Y. Egorov from the Ioffe Institute, St. Petersburg, Russia. A.Y. Egorov gratefully acknowledges support by an Alexander von Humboldt fellowship. This work was partly funded by the Bundesministerium für Bildung und Forschung (BMBF) and the European Commission under BriteEuram BRPR-CT98-0721 (OPTIVAN).

References

[1] Infineon Technologies , "Parallel Optical Links", [Online], (1999), Available http://www.infineon.com, Link: products → fiber optics → PAROLI.

[2] K.S. Giboney, L.B. Aronson, and B.E. Lemoff, "The ideal light source for datanets",*IEEE Spectrum*, vol. 2, pp. 43–53, 1998.

[3] F. Mederer, C. Jung, R. Jäger, M. Kicherer, R. Michalzik, P. Schnitzer, D. Wiedenmann, and K.J. Ebeling, "12.5 Gbit/s data rate fiber transmission using single-mode selectively oxidized GaAs VCSELs at λ=850 nm", in Proc. *IEEE LEOS Annual Meeting*, San Francisco, CA, USA, 1999, pp. 697–698.

[4] M. Kondow, K. Uomi, A. Niwa, T. Kitatani, S. Watahiki, and Y. Yazawa, "GaInNAs: a novel material for long-wavelength-range laser diodes with excellent high-temperature performance", Jpn. J. Appl. Phys., vol. 35, pp. 1273–1275, 1996.

[5] K.D. Choquette, J.F. Klem, A.J. Fischer, O. Blum, A.A. Allerman, I.J. Fritz, S.R. Kurtz, W.G. Breiland, R. Sieg, K.M. Geib, J.W. Scott, and R.L. Naone, "Room temperature continuous wave InGaAsN quantum well vertical-cavity lasers emitting at 1.3 μm" , Electron. Letters, vol. 36, pp. 1388–1390, 2000.

[6] N. Nishiyama, S. Sato, T. Miyamoto, T. Takahashi, N. Jikutani, M. Arai, A. Matsutani, F. Koyama, and K. Iga, "First CW Operation of 1.26 μm Electrically Pumped MOCVD Grown InGaAsN/GaAs VCSEL", *IEEE Semiconductor Laser Conf.* , Monterey, CA, USA, 2000, post deadline paper, PD 2.

[7] G. Steinle, H. Richert, A.Yu. Egorov, "Monolithic VCSEL with InGaAsN active region emitting at 1.28 μm and CW output power exceeding 500 μW at room temperature", Electron. Letters, vol. 37, pp. 93–95, 2001.

Spatial Investigation of Transverse Mode Turn-On Dynamics in VCSELs

Safwat W.Z. Mahmoud

Data transmission experiments with single-mode as well as multimode 850 nm VCSELs are carried out from a near-field point of view. Special attention is paid to important quantities like on/off-ratio and bit error rate (BER). A single-mode VCSEL oscillating on the fundamental LP_{01} mode shows no change in eye opening, on/off-ratio, and BER at different lateral fiber coupling positions. In case of a multimode VCSEL oscillating both on the LP_{01} mode and LP_{11} donut mode we observe a significant lateral change in the on/off-ratio which plays an important role in BER measurements.

1. Introduction

A light source of great scientific and commercial interest is the vertical-cavity surface-emitting laser (VCSEL) because it offers a number of favorable properties like low lasing threshold current [1], dynamic single-mode operation [2], low divergence circular beams [3], high packing density [4], and high-speed current modulation for multi-Gb/s data generation [5]. Despite these attractive features, the complex transverse modal behavior of VCSELs at high pump rates and large active diameters is a major drawback mainly in datacom applications. The mode dynamics are strongly dependent on the spatial carrier distribution which itself is governed by the influence of pump induced current spreading, hole burning, and thermal gradients in the laser cavity [6], [7]. The details of the transverse mode pattern in the device are of concern especially for fiber coupling where today both single-mode and multimode VCSEL approaches are followed in combination with a graded-index multimode fiber (MMF). In addition, the laser turn-on event depends on the driving current and consequently can be expected to be influenced by the device's transverse mode structure. In this work we employ near-field measurements to investigate the spectral and spatial intensity distribution of transverse modes in VCSELs with 4 and 6 μm active diameters. We use the same approach to perform bit error measurements at moderate bit rates of 1 and 2.5 Gb/s for different lateral fiber coupling offsets.

2. Device Structure and Output Characteristics

The layer structure of the selectively oxidized top-emitting VCSELs used in this work is grown by solid source molecular beam epitaxy. The active region is formed by three 8 nm thick GaAs quantum wells embedded in $Al_{0.2}Ga_{0.8}As$ barriers for about 850 nm gain peak wavelength. The carbon doped p-type and silicon doped n-type Bragg reflectors consist of 19 and 35.5 $Al_{0.1}Ga_{0.9}As/Al_{0.9}Ga_{0.1}As$ pairs, respectively. For lateral current confinement, a single 25 nm thick AlAs layer is placed in the first quarter wavelength layer above the active zone and is subsequently oxidized after a mesa etching process. In Fig. 1 the light output characteristics of 4 μm (solid curves) and 6 μm (dashed curves) aperture diameter selectively oxidized VCSELs are depicted. The smaller device has a threshold current of 0.7 mA and emits in a single mode, as shown in Fig. 2(b). The threshold current of the larger device is 1.1 mA and it starts lasing on the fundamental mode up to 1.5 mA, then becomes multimode for higher currents as illustrated in Fig. 2(d).

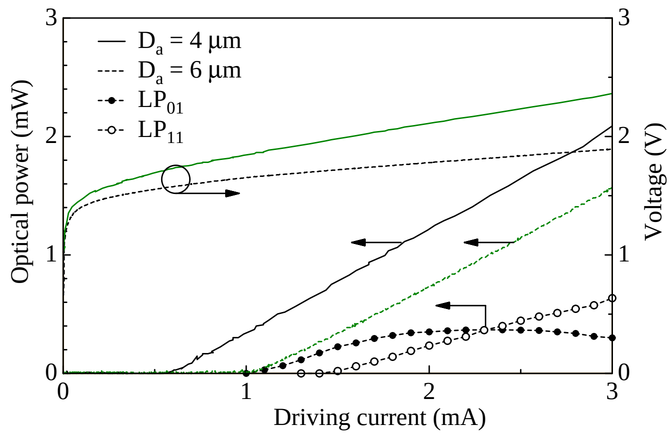

Fig. 1. Light-current and current-voltage characteristics of 4 μm (solid curves) and 6 μm (dashed curves) aperture oxide-confined VCSELs. The closed and open circles define the peak spectral power emitted from the larger device in the LP_{01} and LP_{11} modes, respectively.

To analyze the spatial profiles of the lasing modes we have carried out near-field measurements based on a single-mode fiber (SMF) tip scanning technique [8]. Fig. 2(a) shows a transverse central cross-section of the measured near-field intensity profile of the Gaussian-like transverse fundamental LP_{01} mode (solid circles) for the VCSEL with active diameter $D_a = 4\,\mu$m at 2 mA bias current and 300 mV modulation voltage of a 1 Gb/s data rate pseudo-random bit sequence (PRBS) signal. Under these conditions, emission is single-mode with a sidemode suppression ratio of better than 30 dB, as illustrated in Fig. 2(b). The same measurements for the VCSEL with $D_a = 6\,\mu$m at 2 mA bias current and 150 mV modulation voltage are illustrated in Fig. 2(c). In this case the increase of the active diameter leads to the excitation of both LP_{01} mode (solid circles) and the higher order transverse LP_{11} mode (open circles). Both modes are circularly symmetric with the LP_{11} mode exhibiting an intensity dip in the center of the cavity. The emission spectrum in Fig. 2(d) shows that the LP_{11} mode is blue shifted from the LP_{01} mode by 0.4 nm.

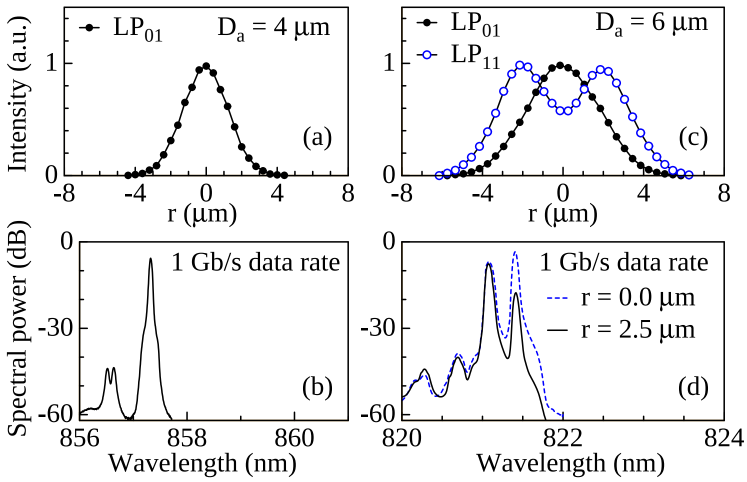

Fig. 2. Spatial intensity distribution and emitted spectrum of a 4 μm aperture device at 2 mA bias current and 300 mV modulation voltage (a) and (b). The results of the same measurements on a 6 μm aperture device at 2 mA bias current and 150 mV modulation voltage are displayed in (c) and (d), where the additional spectrum in (d) is taken for 2.5 μm radial fiber offset.

3. Data Transmission

To investigate data transmission at different lateral positions of the fiber relative to the VCSEL center, we employed a SMF tip near-field scanning system in combination with a data transmission setup [5], using a 2 GHz bandwidth germanium avalanche photodiode as a receiver. The bias current of 2 mA and a 1 Gb/s PRBS signal of 2^7-1 word length and modulation voltage $V_{pp} = 300$ mV were combined in a bias-tee and fed to the VCSEL of $D_a = 4\,\mu$m. The results of the data transmission experiments using the 2 m length SMF whose tip has a semispherical lens or using a 5 m length, 50 μm core diameter MMF are summarized in Fig. 3. The eye diagrams in the inset show that as the SMF tip is moved laterally from the center at a radial position r = 0 to the edge of the LP_{01} mode at $r = 2\,\mu$m, the eye remains symmetric and has the same form as with the MMF. The received power for a BER of 10^{-11} is about -19 dBm for both SMF and MMF. The radial distribution of the on/off-ratio (P_{on}/P_{off}) is obtained from a sampling oscilloscope by dividing the average values of histograms on both the "1" and "0" rails of the eye diagram. The closed squares in Fig. 4 reveal a nearly constant ratio of 9 dB which is the same value as obtained by using the MMF.

In case of the multimode VCSEL, the same bias current and modulation signal, however with $V_{pp} = 150$ mV, are chosen. In accordance with the emission spectrum in Fig. 2(d), at the center both LP_{01} and LP_{11} modal power is coupled into the SMF. As the tip is moved toward the edge of the VCSEL, the LP_{01} mode is strongly attenuated and shows 10 dB suppression ratio in the interval between $r = 2.5 \ldots 3.5\,\mu$m. This is evidenced in the results of the data transmission experiments in Fig. 5 using the forementioned fibers. The eye diagrams in the inset show that at r = 0 the eye is no longer symmetric because

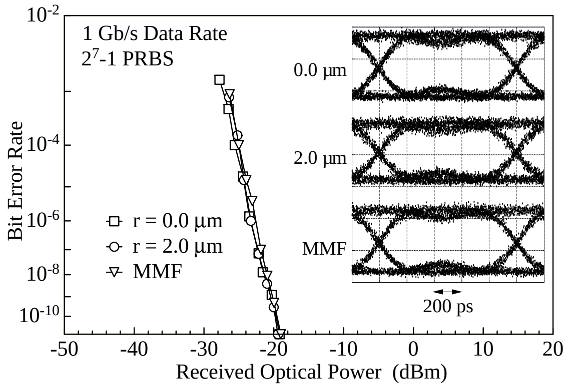

Fig. 3. Bit error measurements using a 2 m length SMF at two different radial positions or using 5 m MMF. The 4 μm aperture VCSEL is fed with 2 mA dc and 1 Gb/s PRBS signals at a word length of $2^7 - 1$ and $V_{pp} = 300$ mV. The corresponding eye diagrams are recorded at 10^{-11} BER.

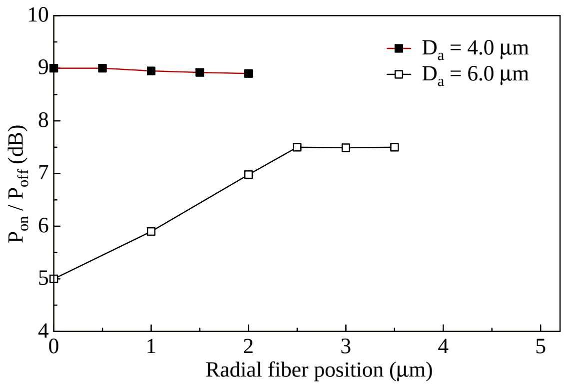

Fig. 4. Spatial on/off-ratio distribution for a 4 μm aperture VCSEL (closed squares) under the same conditions as in Fig. 3 and for a 6 μm aperture device (open squares) under the same conditions as in Fig. 5.

the LP_{01} and LP_{11} modes are both coupled into the SMF. Since the LP_{11} mode has a higher threshold current, as seen in Fig. 1, it has a lower resonance frequency at the same bias current and as a result gives rise to ringing in the eye diagram. At r = 2.5 μm, the dominance of LP_{11} at a sidemode suppression in the order of 10 dB gives a symmetric eye opening with a longer switch-on time than at r = 0, as expected. These conclusions are supported by the results of theoretical simulations performed in [9]. In calculations of the time traces of the LP_{11} and LP_{01} modal powers it was found that the latter has a shorter turn-on delay and accordingly the LP_{01} mode starts lasing emission. When a significant number of photons are present in the laser microcavity, a hole is burnt in the carrier profile which leads to the excitation of the higher order LP_{11} mode. Using a MMF, a superposition of all portions of the two modes gives an eye diagram with symmetric opening. The BER curves show that the received optical power for a BER of 10^{-11} is -16.6 dBm for the SMF at r = 2.5 μm with a power penalty of 3.3 dB at r = 0 and of 2.1 dB for the MMF. This difference is attributed to the radial change of P_{on}/P_{off}, as illustrated in Fig. 4 (open squares). The on/off-ratio is continually increasing up to r = 2.5 μm where it reaches a constant value of about 7.5 dB, while 6.5 dB ratio is recorded for the MMF. These results are also confirmed by the separate light-current characteristics in Fig. 1 which are obtained from the spectrometer as the peak spectral power of each mode. In accordance with these curves, the average differential efficiency for the LP_{01} mode is smaller than for LP_{11} in the interval around 2 mA at which the VCSEL is modulated. The data transmission experiments are repeated with the same multimode VCSEL and fibers for 2.5 Gb/s data rate and are summarized in Fig. 6. The same effects as in the case of 1 Gb/s data transmission are seen, but a BER floor at 10^{-8} is observed at r = 0 because the “1” rail in the eye diagram exhibits much noise which reduces its opening. This increased noise is probably due to mode partition because as the total optical power remains constant, the relative distribution of the modal powers fluctuates as shown in Fig. 1.

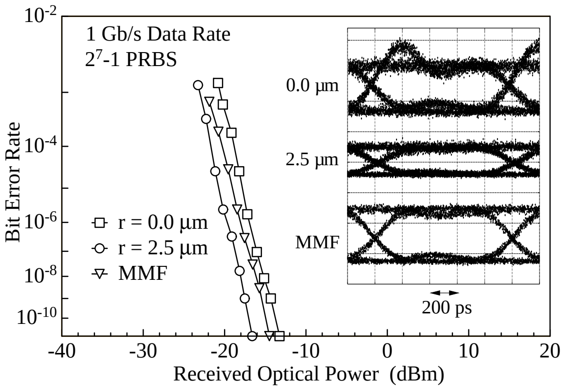

Fig. 5. Bit error measurements using 2 m SMF at different radial positions defined by the legends or 5 m MMF for a 6 μm aperture device fed with 2 mA dc and 1 Gb/s PRBS signal at a word length 2^7-1 and $V_{pp} = 150$ mV. The corresponding eye diagrams are recorded at 10^{-11} BER.

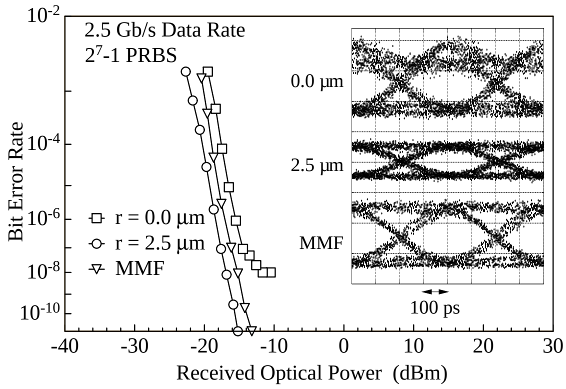

Fig. 6. The same measurements as in Fig. 5 at 2.5 Gb/s data rate. The eye diagrams are recorded at the minimum BER for each case.

4. Conclusion

We have measured spectral as well as spatial intensity distributions of the eigenmodes for single-mode and multimode VCSELs under modulation. Bit error rate measurements at 1 Gb/s and 2.5 Gb/s for these devices have been presented for different lateral SMF offsets which point to a better performance of single-mode compared with multimode VCSELs. The multimode device has shown a lateral variation of the on/off-ratio which leads to a reduced BER for the LP_{11} mode at 10 dB LP_{01} suppression than when the two modes coexist. We conclude from these results that at moderate bit rates the on/off-ratio is the dominant mechanism governing the BER measurements regardless of the type of oscillating mode in the cavity. The difference between the switch-on times of the lasing modes in the multimode device can be of importance even at high bit rates.

References

[1] D.G. Deppe, D.L. Huffaker, T. Oh, H. Deng, and Q. Deng "*Low-threshold vertical-cavity surface-emitting lasers based on oxide-confined and high contrast distributed Bragg reflectors,*" IEEE J. Selected Topics Quantum Electron., vol. 3, pp. 893–904, 1997.

[2] C. Jung, R. Jäger, P. Schnitzer, R. Michalzik, B. Weigl, S. Müller, and K.J. Ebeling "*4.8 mW single-mode oxide confined top-surface emitting vertical-cavity laser diodes,*" Electron. Lett., vol. 32, pp. 1790–1791, 1997.

[3] D.G. Deppe and D.L. Huffaker, "*High spatial coherence vertical-cavity surface-emitting laser using a long monolithic cavity,*" Electron. Lett., vol. 33, pp. 211–213, 1997.

[4] R. King, R. Michalzik, C. Jung, M. Grabherr, F. Eberhard, R. Jäger, P. Schnitzer, and K.J. Ebeling "*Oxide confined 2D VCSEL arrays for high-density inter/intra-chip interconnects,*" Proc. SPIE, vol. 3286, pp. 64–67, 1998.

[5] D. Wiedenmann, R. King, C. Jung, R. Jäger, P. Schnitzer, R. Michalzik, and K.J. Ebeling "*Design and analysis of single-mode oxidized VCSEL's for high-speed optical interconnects,*" IEEE J. Quantum Electron., vol. 5, pp. 503–511, 1999.

[6] C. Deng, I. Fischer, and W. Elsäßer, "*Transverse modes in oxide confined VCSELs: Influence of pump profile, spatial hole burning, and thermal effects,*" Optics Express, vol. 5, pp. 38–47, 1999.

[7] Y.G. Zhao and J. McInerney, "*Transverse-mode control of vertical-cavity surface-emitting lasers,*" IEEE. J. Quantum Electron., vol. 32, pp. 1950–1958, 1996.

[8] S.W.Z. Mahmoud, H. Unold, W. Schmid, R. Jäger, R. Michalzik, and K.J. Ebeling, "*Analysis of longitudinal mode wave guiding in vertical-cavity surface-emitting lasers with long monolithic cavity*", Appl. Phys. Lett., vol. 78, pp. 586–588, 2001.

[9] J. Dellunde, M.C. Torrent, J.M. Sancho, and K.A. Shore, "*Statistics of transverse-mode turn-on dynamics in VCSEL's*", IEEE J. Quantum Electron., vol. 33, pp. 1197–1204, 1997.

Theoretical Investigation of Transverse Modes in PCSELs

Pavel S. Ivanov, Heiko J. Unold

Selected results of a numerical analysis of the spatial part of the optical mode in Photonic Crystal Surface-Emitting Lasers (PCSELs) is introduced. It is shown that such a structure provides different propagation constants for different spatial modes which can result in larger optical feedback for LP_{01} optical mode in comparison with other modes guided by the photonic crystal defect.

1. Introduction

Vertical-Cavity Surface-Emitting Lasers (VCSELs) attracted significant attention in the past few years because of their characteristics such as a low threshold current, single longitudinal mode operation, circular shape of the output beam and wafer-scale integration. Moreover, high-speed data transmission and temperature stability of VCSELs has been demonstrated [1] which is important for their application as optical sources in low-cost short-distance optical links. However, for reliable high-speed data transmission and increased transmission distances controlling the optical mode behavior is still an issue due to the deterioration of modulation [2] and noise properties [3] with increasing number of lasing modes. For this purpose, the optical mode control has two main ways: modifications of transverse guiding and creation of conditions where the modes have different losses or gain [4]. One such method involves photonic crystals for localization of the optical wave and creation of selective conditions for high-order modes. In result, the single mode operation achieved. In given paper, we numerically investigate and discuss this methodology for further optimization of operation parameters of given type of lasers.

2. Simulation Results

In the most common case the Photonic Crystal Surface-Emitting Laser are fabricated by dry etching a pattern of small air holes in the cavity medium of the VCSEL. We chose for our investigations the simple PCSEL structure (Fig.1) where holes are etched through both mirrors and active region [5]. Such modification by hole etching has changes the nature of the cavity by including an additional resonance system for the optical field in the laser cavity. Therefore, the hexagonal geometry of the hole pattern provides additional confinement of the optical field in the area where one hole is left out. This leads to a more complex cavity in comparison with conventional VCSELs. In other words, the optical confinement is now composed of the reflection from the mirrors and the effect of the photonic crystal area. Thus, a numerical investigation of the mentioned cavity is quite complex and in some cases it is still impossible because it requires direct solution of the Maxwell equations in a three-dimensional coordinate system connected with detailed space cell due to the very small size of photonic crystal area. Therefore, assuming that the

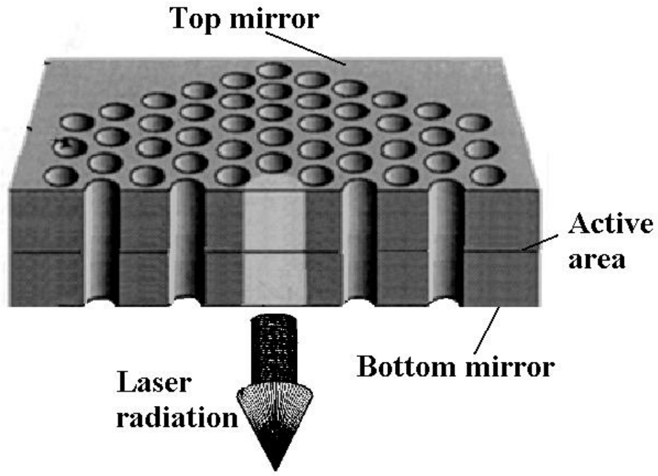

Fig. 1. Investigated structure of PCSEL [5]

investigated PCSEL can operate in several transverse modes, the value of the refractive index to be constant in the considered wavelength range and the dielectric constant to be constant in the z-direction between mirrors, the electrical field can be presented as [6]:

$$E(x, y, z) = \frac{1}{2} \sum_{j=0}^{n} \hat{e_j} E_j \psi_j(x, y) \exp(i(\beta_j z - \omega_j t)), \tag{1}$$

Here, n is the total number of transverse modes, j is the transverse mode index, $\hat{e_j}$ is the polarization vector unit, E_j is the j-th transverse mode amplitude, $\psi_j(x, y)$ is the transverse mode distribution, β_j is j-th mode propagation constant, ω_j is the angular frequency of the mode. The value of the transverse mode amplitude E_j can be computed based on the conventional coupled mode theory of optical cavities or using direct solution of rate equations for field density. It is not so difficult to see, that the amplitude inside etched holes will be close to zero, because of two reasons: there is neither gain and reflectivity available. At the same time, the transverse part of the mode can exist inside the holes and its distribution is described by the eingenvalue equation:

$$\nabla_T^2 \psi_j(x, y) + \{n^2(x, y) \frac{\omega_j^2}{c^2} - \beta_j^2\} \psi_j(x, y) = 0, \tag{2}$$

Here, where ∇_T^2 is the transverse Laplacian, $n(x, y)$ is the refractive index of structure and c is the velocity of light in vacuum. In present paper, we focus our attention only on the transverse field behavior because the mentioned photonic crystals provide a periodic modulation of the reflection coefficient in the XY plane. Therefore, this modulation mainly effects the transverse part of the optical modes defined by equation (2).

3. Numerical Model and Investigated Structure

Solution of the eigvenvalues problem (2) is achieved by using the finite element method. We chose variation of Neumann and Dirichlet boundary conditions on the border region b for computation [7] which can be accordingly presented as:

$$\psi_j(x, y)|_b = 0, \nabla_T \psi_j(x, y)|_b = 0. \tag{3}$$

This method allowed us to define the isolation of a wave inside the waveguide core from the surrounding hole cladding region. It was made by comparison of eigvenvalues computed for both types of boundary conditions (3) at the same geometry and a vacuum wavelength. Numerical investigation was made in two directions: influence of hole radius and hole pitch influences on mode properties of the described structure. For this, we have investigated several samples presented in Table 1 at different vacuum wavelengths. The value of the refractive index is set to 1 inside the holes and to 3.5 for the surround area for all samples. First, let us consider the evolution of the effective the mode index (Fig. 2) for LP_{01} and LP_{11} waveguiding modes with the normalized quantity $k_n = 2\pi\Lambda/\lambda$ for the structure No 5. The behavior of the evolution is similar to the commonly used BV diagram of an optical fiber. The value of the effective refractive index for the LP_{01} mode is larger than the effective refractive index for LP_{11} in the whole computed range of k_n. This effect demonstrates that the LP_{11} extends further into the holes in comparison with LP_{01} especially at small values of k_n. The difference between the mode indices decreases with increasing k_n.

Table 1. Geometrical parameters of investigated structures

No of structure	Pitch Λ, microns	Hole radius r, microns	$2r/\Lambda$
1	1.60	0.1	1.1250
2	1.50	0.1	0.1333
3	1.25	0.1	0.1600
4	1.25	0.2	0.3200
5	1.25	0.5	0.8000

At the same time, the distribution of LP_{01} mode and its level of localization also chances with k_n (see Fig. 3). At the small values of k_n the optical wave has the smallest level of localization in the core where the hole is missing, and the wave can propagate in the cladding region constructed by holes. In other hand, increasing the k_n results in an increase of the localization level and focusing of the light mainly inside the core.

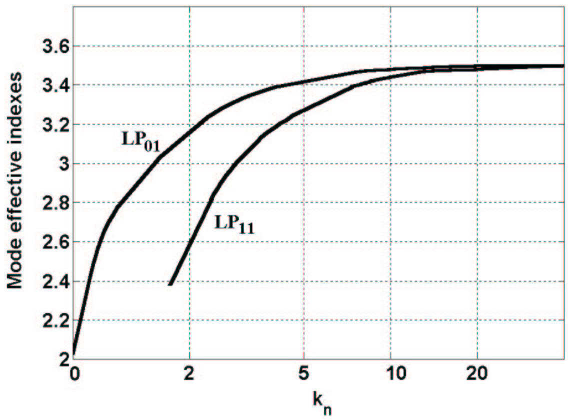

Fig. 2. Influence of the k_n on effective refractive index of LP_{01} and LP_{11} modes for sample 5

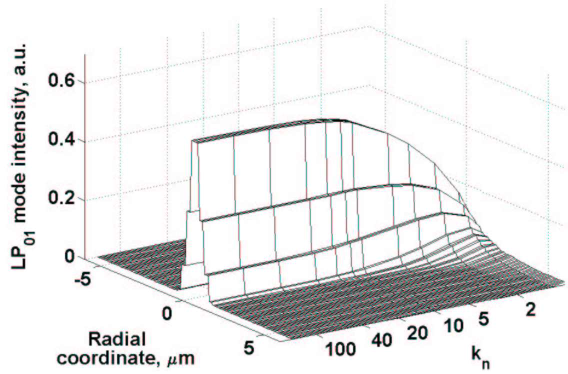

Fig. 3. Evolution of LP_{01} mode radial distribution with k_n for sample 5

The same behavior of the LP_{01} mode effective index is still observed for smaller hole radius. Fig.4 demonstrates the change of the mode index for structures No 3-5. It shows that decreasing the hole radius at constant pitch leads to increasing of the effective index of a given mode at smallest values of k_n (at largest vacuum wavelength of the radiation). Thus, following our above conclusions, the radiation can propagate more inside the air holes due to increased the hole sizes.

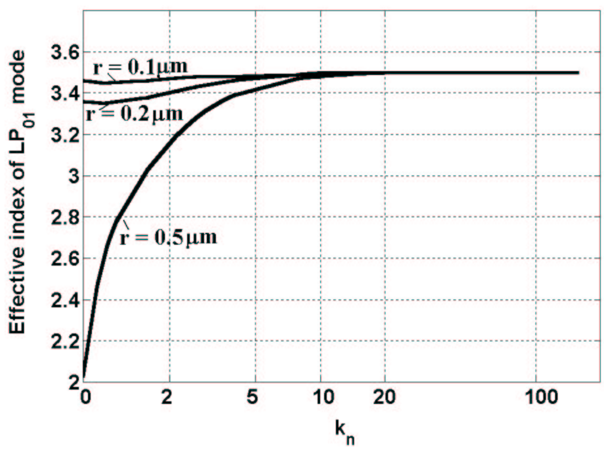

Fig. 4. Change of the PL_{01} effective index with k_n

4. Analysis

Based on the results presented above, we can conclude that in the given waveguide laser structure the effective indices of the transverse modes are strongly dependent on the geometrical parameters of the hole waveguiding structure. The LP_{01} mode has the maximal effective refractive index and therefore this mode more localized in the semiconductor medium, where the refractive index has a value close to 3.5. Let us now consider coupled mode theory of distributed feedback lasers [8]. Following this, in order to exist, the radiation which propagates inside a hole in the cavity should also be reflected in the optical cavity. In our specific case, there is no feedback in the hole region simply because here the mirror is removed by etching. Therefore, the transverse optical modes characterized by the lowest value of the effective mode index propagates more in the air holes, and they are badly reflected in the optical cavity. This creates conditions where LP_{01} dominates in the cavity, and this domination becomes maximal at $k_n \approx 9$ for structure 5, where LP_{01} mode is still situated mainly in the semiconductor and has the maximal feedback. The next guiding mode LP_{11} has smaller reflectivity from the mirror facet at the same value of k_n, and this results in a smaller quantity of the feedback provided by the Bragg mirror for this mode. The position of this 'optimal point' can be moved by changing the geometrical parameters of the hole region, for example increasing the hole size as demonstrated in Fig. 4.

5. Conclusion

In the present paper, we demonstrated selected results of numerical investigation of transverse modes in a photonic crystal slab, which supports transverse modes dominating in the cavity of a PCSEL. It was shown that such a slab provides different effective refractive indices for different modes. which can result in a creation of different feedback conditions for those modes. In addition, a way to manage this selection by changing the hole radius was introduced.

Our further research interests focused on the numerical investigation of the effective refractive index of the photonic crystal cladding region and computation of normalized B-V diagrams for the given waveguiding structure.

References

[1] F. Mederer, et al., "5 Gbit/s data transmission with single-mode GaAs VCSELs over a 0^0C to 80_0C temperature range," *Proc. ECOC 2000*, Munich, Germany, Sept. 2000.

[2] I. A. Sukhoivanov, P. S. Ivanov, "Spatial characteristics of oxide-confined VCSEL in single and multimode conditions," *Proc. of Int. Workshop on Optical Waveguide Theory and Numerical Modelling*, Paderborn, Germany, April 2001.

[3] Li-Gao Zei, et al., "Noise performance of multimode VCSELs," *J. Lightwave Technol.*, vol. 19, pp. 884-892, June 2001.

[4] H. J. Unold, et al., "Advances in self-aligned surface-etched single-mode VCSELs," *Proc. of Photonics West 2002*, San Jose, USA, Jan. 2002.

[5] O. Painter, et al., "Lithographic tuning of a two-dimensional photonic crystal laser array," *IEEE Photonic Technology Lett.*, vol. 12, No. 9, pp. 1126-1128, Sep. 2000.

[6] J. Y. Law, G. P. Agrawal, "Effects of spatial hole burning on gain switching in vertical-cavity surface-emitting lasers," *IEEE J. Quantum Electron.*, vol. 33, pp. 462-468, Mar. 1997.

[7] "Partial differential equation toolbox user's guide," Mathworks Inc., 1996, http://www.mathworks.com

[8] G. P Agrawal, A. H. Bobeck, "Modelling of distributed feedback semiconductor lasers with axially-varying parameters," *IEEE J. Quantum Electron.*, vol. 24, pp. 2407-2414, Dec. 1988.

Data Transmission Using GaAs-Based InAs-InGaAs Quantum Dot LEDs Emitting at 1.3 μm Wavelength

Max Kicherer

We use vertical emission light-emitting diodes (LEDs) based on long-wavelength, self-assembled InAs-InGaAs quantum dots (QDs) grown on GaAs substrate to demonstrate up to 1 Gbit/s digital data transmission. The devices are characterized in terms of small-signal modulation, showing bandwidths beyond 1 GHz.

1. Introduction

There is an increasing interest in the development of GaAs-based active materials emitting at 1.3 and 1.55 μm wavelength for telecommunication applications. Since the first realization of lasing using self-assembled InAs-GaAs quantum dots on GaAs substrate, great advances have been made yielding laser diodes with remarkably low threshold current densities [1, 2, 3, 4]. QD-based LEDs may represent efficient and cheap sources for low data rate links at 1.3 μm [5]. To our knowledge, this letter presents the first demonstration of data transmission using 1.3 μm QD LEDs.

2. Device Structure

In this experiment we use single-mirror QD LEDs operating at around 1.3 μm wavelength. Devices are grown on Si-doped (001)-oriented GaAs substrate using solid source molecular beam epitaxy. A $\lambda/2$-thick layer of AlGaAs is grown first for carrier confinement, followed by a GaAs spacer layer. For the active QD region InAs is deposited directly on the GaAs surface and covered by an InGaAs layer. A successive low-index $Al_{0.97}Ga_{0.03}As$ layer is intended for wet oxidation to serve as a current aperture. It is sandwiched between two $Al_{0.3}Ga_{0.7}As$ barriers and forms a single Bragg period with the following high-index GaAs layer. To phase match the reflection from the gold layer deposited on top, a highly p-doped GaAs cap layer is grown, serving as a contact layer as well. Layer thicknesses are chosen such that radiation reflected by the top mirror constructively interferes with emission from the QD region, resulting in a fourfold increase in optical output at the substrate side [6]. Device fabrication consists of mesa etching, lateral wet oxidation of the $Al_{0.97}Ga_{0.03}As$ layer, contact evaporation and annealing. Using this structure we previously demonstrated an external quantum efficiency of 1 % at low current densities [5].

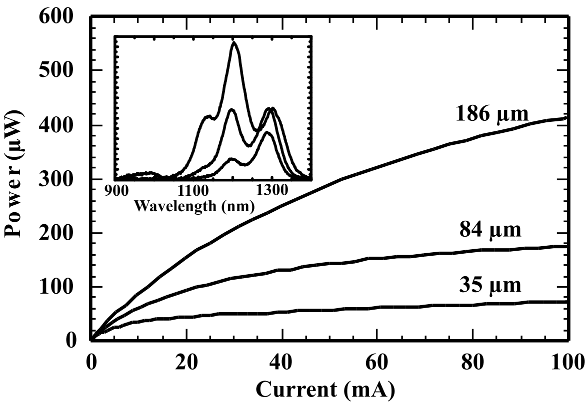

Fig. 1. Light-current characteristics of single-mirror QD LEDs with different current aperture sizes (CW, room temperature). Inset: Electroluminescence spectra of a 84 μm-size device for injection currents of (from bottom to top) 4, 12 and 50 mA.

3. DC Characteristics

In Fig. 3. the optical output power is plotted versus the injected current for three different device sizes denoted by their oxidized aperture size. The inset shows electroluminescence (EL) spectra taken for CW operation of a 84 μm-size device. As the injection density increases, ground state emission at 1285 nm saturates due to state filling in the QDs, and two peaks corresponding to emission from excited states are observed. Total output power also saturates since carriers on excited states are more easily lost due to escape to the wetting layer and nonradiative recombination.

4. Small-Signal Modulation

We use a scalar network analyzer for the small-signal modulation measurements. The modulation signal out of the 50 Ω impedance source is combined in a bias-T with the DC-bias current and fed to the LED. The device is contacted by a ground-signal-ground configuration high-frequency probe head to ensure signal integrity during on-wafer testing. The optical signal is collected using a microscope objective with a numerical aperture of 0.4 and focused onto an InGaAs PIN detector of 100 μm diameter using another objective. All optical components are anti-reflection coated for the emission wavelength. The electrical signal is amplified by 25 dB prior to detection. The bandwidth of the setup is limited to 1.5 GHz by the photodiode (PD). All measurements have been performed at room temperature with no temperature stabilization of the device.

Fig. 4. shows the modulation response curves of an 84 μm device for different bias currents, normalized to the value at 20 MHz. Periodic modulations in the curves are caused by reflections on the feeding lines due to the impedance mismatch between LED and driving source. The modulation power was set to −11 dBm out of the 50 Ω system for all currents. The 3 dB decay is indicated by a horizontal line. We observe the modulation depth to increase with bias current up to about 4 mA, while for higher currents it decreases. Furthermore we observe a continuous increase in bandwidth with increasing bias, leading to rather flat response curves for high driving currents. The maximum bandwidth reached for 20 mA of bias is 860 MHz.

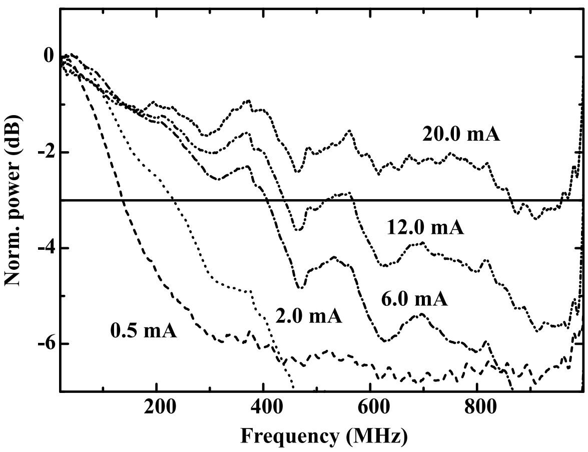

Fig. 2. Normalized modulation response curves for an 84 μm device at different driving currents.

This behaviour can be attributed to state filling, as observed in the DC characteristics. The modulation depth is related to the slope of the light-current curve, which is seen to decrease at high currents in Fig. 3.. On the other hand, at high bias the modulation mostly affects carrier population on excited states, which have shorter carrier lifetime due to both increased nonradiative recombination and an alternative relaxation channel to lower states [7]. This shorter carrier lifetime, also observed independently by time-resolved photoluminescence measurements, results in the observed increase of the modulation bandwidth with bias.

The same setup was used to investigate 35 and 186 μm-size devices. At a bias of 20 mA, the 186 μm devices showed a maximum bandwidth of about 400 MHz, while for the 35 μm devices we found a maximum bandwidth of above 1 GHz at 8 mA of driving current.

5. Data Transmission Experiments

For digital modulation, the scalar network analyzer is replaced by a pulse pattern generator on the transmission side. In the detection circuit the same PD was used. After two amplifiers, totaling about 50 dB of gain, the bit pattern was viewed on a digital sampling oscilloscope.

We use the 84 μm device presented above at a bias of 12 mA. The generator is set for a modulation voltage of 2 V_{pp} out of the 50 Ω impedance port. With a pseudo-random bit sequence of $2^7 - 1$ word length at 300 Mbit/s we could detect an open, but somewhat asymmetric eye diagram. Using a repetitive 1-0-bit sequence at a data rate of 1 Gbit/s we recorded the eye diagram shown in Fig. 5.. Again we use the 84 μm device biased at 12 mA of DC current. The modulator output was set for 1.6 V_{pp}. The resulting eye diagram is wide open and symmetric.

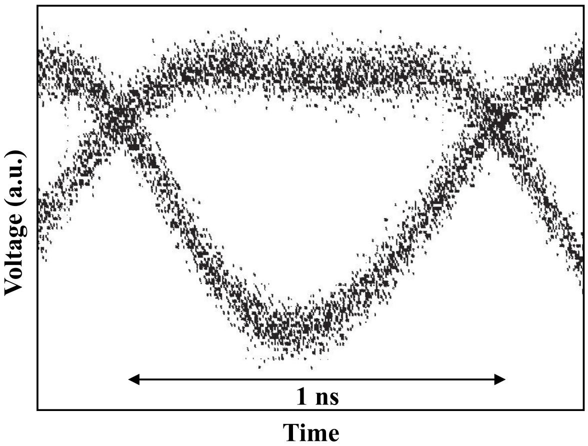

Fig. 3. Eye diagram for an alternating 1-0-bit sequence transmitted at 1 Gbit/s using an 84 μm LED.

6. Conclusions

In conclusion, we have demonstrated up to 1 Gbit/s data transmission employing single-mirror vertically emitting LEDs operating around 1.3 μm wavelength from self-assembled InAs-InGaAs quantum dots on GaAs substrate. This shows that QD LEDs may be suitable as low-cost sources for short-distance 1.3 μm optical links.

7. Acknowledgments

All samples have been grown an processed by A. Fiore, U. Oesterle and R.P. Stanley in M. Ilegems group at the Institute for Micro-Optoelectronics of the Ecole Polytechnique Fédérale de Lausanne.

The authors would like to acknowledge support by the European Community under IST Project "GSQ".

References

[1] G. Park, O.B. Shchekin, D.L. Huffaker, and D.G. Deppe, "Low-threshold oxide-confined 1.3-μm quantum-dot laser," *IEEE Photon. Technol. Lett.*, vol. 12, no. 3, pp. 230–232, 2000.

[2] Y.M. Shernyakov, D.A. Bedarev, E.Y. Kondrateva, P.S. Kopev, A.R. Kovsh, N.A. Maleev, M.V. Maximov, S.S. Mikhrin, A.F. Tsatsulnikov, V.M. Ustinov, B.V. Volovik, A.E. Zhukov, Z.I. Alferov, N.N. Ledentsov, and D. Bimberg, "1.3 μm GaAs-based laser using quantum dots obtained by activated spinoidal decomposition," *Electron. Lett.*, vol. 35, no. 11, pp. 898–900, 1999.

[3] K. Mukai, Y. Nakata, K. Otsubo, M. Sugawara, N. Yokoyama, and H. Ishikawa, "1.3 μm CW lasing of InGaAs-GaAs quantum dots at room temperature with a

threshold current of 8 mA," *IEEE Photon. Technol. Lett.*, vol. 11, no. 10, pp. 1205–1207, 1999.

[4] X. Huang, A. Stintz, C.P. Hainsa, G.T. Liu, J. Cheng, and K.J. Malloy, "Efficient high-temperature CW lasing operation of oxide-confined long-wavelength InAs quantum dot lasers," *Electron. Lett.*, vol. 36, no. 1, pp. 41–42, 2000.

[5] A. Fiore, U. Oesterle, R.P. Stanley, and M. Ilegems, "High-efficiency light-emitting diodes at $\approx 1.3\,\mu$m using InAs-InGaAs quantum dots," *IEEE Photon. Technol. Lett.*, vol. 12, no. 12, pp. 1601–1603, 2000.

[6] D.G. Deppe, J.C. Campbell, R. Kuchibholta, T.J. Rogers, and B.G. Streetman, "Optically-coupled mirror-quantum well InGaAs-GaAs light emitting diode," *Electron. Lett.*, vol. 26, no. 20, pp. 1665–1666, 1990.

[7] M. Grundmann and D. Bimberg, "Theory of random population for quantum dots," *Phys. Rev. B*, vol. 55, no. 15, pp. 9740–9745, 1997.

Properties and Design Features of Tapered Gain Region Semiconductor Laser Amplifiers

Frank Demaria and Manfred Mundbrod

By measuring the corrected far fields of tapered laser amplifiers, we calculate the astigmatism and virtual spot sizes at different currents and optical output powers. The Results of those investigations concerning the coupling efficiency of the signal beam into tapered laser amplifiers and the demands on the positioning accuracy are also presented. We report a novel self-aligned process for fabricating single-mode ridge waveguide structures.

1. Introduction

High brightness laser sources are essential for various applications like nonlinear frequency doubling [1] or free-space communication. The master-oscillator power amplifier approach provides this with reasonable effort and cost. It combines the particular advantages of two common semiconductor laser types, the diffraction-limited spatial beam quality of small-aperture single-mode lasers and the high optical output power of the broad-area type. Both, the spatial beam quality, described by the assigned beam quality factor M^2, and the optical output power P are considered in the attribute brightness [2]

$$B = \frac{P}{\lambda^2 M_\mathrm{f}^2 M_\mathrm{s}^2} = \frac{P}{A\,\Omega}\,. \tag{1}$$

It is a measure of the maximum achievable optical power density in a focused beam. This depends on the inverse square of the wavelength λ since diffraction is the limiting factor. The indices f and s of the quality factors indicate the vertical and horizontal direction according to the fast and slow axis. Usually brightness is defined as the optical power which is emitted from the area A into the solid angle Ω. For laterally single-mode lasers the area is defined by the optical mode at the output facet. However, applying this definition to laser devices with tapered lateral geometry one has to consider that the emitted beam is highly astigmatic. Thus, in the lateral plane it seems to emerge from an intra-device virtual beam source. The capability of such laser devices concerning high brightness results from the fact that in (1) A is determined by the lateral width of the virtual spot, which at several μm is in the range of the facet width of single-mode lasers. However, the maximum optical output power is limited by the power density at the output facet. So the achievable optical power is proportional to the actual width of the facet and that usually exceeds the virtual spot width by about more than one order of magnitude.

In order to suppress spontaneous recombination of charge carriers, the gain of the amplifier should be sufficiently saturated. Therefore, the intensity of the master laser excluding coupling losses must be higher than the saturation intensity

$$J_{\mathrm{s}} = \frac{\hbar\omega j_{\mathrm{tr}}}{\Gamma q g_0} \tag{2}$$

of the amplifier, wherein J_{s} is the optical power per lateral extension. The transparency current density j_{tr} and the gain coefficient g_0 depend on the material and the confinement factor Γ on the design of the vertical waveguide. The values of J_{s} are in the range of 1 – 2 mW/μm. Since the output power of the master laser is limited, sufficient high optical powers can be achieved by implementing a single-mode waveguide-structure, which acts as a preamplifier. As a pleasant side effect, it also works as a mode filter.

2. Virtual Spot Size and Astigmatism

There are different ways to determine the brightness of laser sources. All of them have in common that besides the optical output power, the focusing properties of the beam have to be quantified. According to (1) one can determine the two orthogonal beam quality factors M_{f}^2 and M_{s}^2. This is done by investigating the beam propagation within the range of a beam waist. For that purpose, the collimated beam is focused and its widths are measured at different distances to the focusing lens. There are various commercial beam analyzing systems available to handle this task. Then together with the wavelength λ, B can be calculated.

Another approach in assessing the beam quality of tapered laser devices is done by measuring the so called corrected far field. Fig. 1 illustrates how this can be achieved. Because of the strong astigmatism, the vertically collimated beam is convergent in the lateral direction. The lateral scan of the optical intensity at the waist is called the corrected far field. It can be interpreted as an expanded image of the virtual source. The magnification factor and also the astigmatism can easily be calculated from the image equation if the distance z to the facet is also quantified. Further interpretation of the corrected far field founds on the fictitious case of the phase correction. Therein, the quadratical curvature of the wavefronts is assumed to be compensated by an ideal cylindrical lens. If the distance of the focusing lens is the same as in the real configuration, the lateral intensity distribution in the back sided focal plane would be the same in both cases [3], only the distance z would be bigger in the theoretical case.

In Fig. 2, the astigmatism of a 2.5 mm-long tapered-region amplifier is plotted as a result of such a measurement versus the optical output power. According to Snells law the astigmatism is approximately the optical length of the taper region. It is rising with higher optical output powers because of the enhanced thermal lensing. The corresponding calculated virtual spot sizes are shown in Fig. 3.

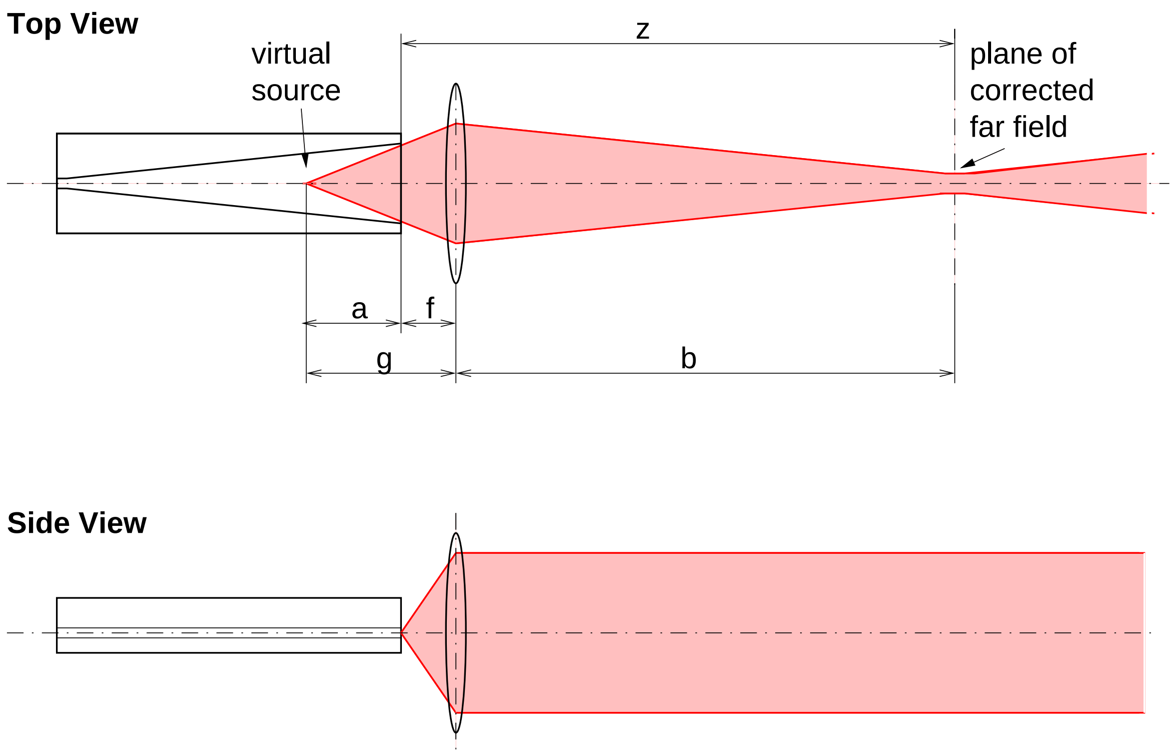

Fig. 1. Schematic diagram, showing the geometric proportions for a corrected far field measurement. Because of the strong astigmatism, the vertically collimated beam is convergent in the lateral direction.

3. Coupling Behavior

The optical coupling of the signal beam into the optical amplifier is crucial for the performance of the setup. The degree of saturation of the amplifier depends on the optical power that is actually coupled in. Whilst the optical power outside the amplifier is easily measured by a photo diode, it seems impossible to measure its coupled rate this way. A practicable method to perform this task is the use of the amplifier itself as a photo diode. We measured the photo current of an unbiased amplifier together with the transmitted optical power by the setup sketched in Fig. 4 . With the assumption that all the carriers are generated within the coupled optical mode, it is easy to calculate the minimum coupling efficiency which then is equal to the optical-electrical conversion efficiency. The mentioned assumption should be considered as a working hypothesis. Nevertheless, most of the results are meaningful, concerning different aspects of the coupling behavior of the system and properties of the amplifier. Furthermore, the described method is suitable for comparative measurements and a useful procedure in the demanding topic of characterizing semiconductor laser amplifiers.

We performed a comparative measurement with two 7° laser amplifiers, with different waveguiding layer structures. The resulting different width of the vertical optical mode is shown Fig. 5, which is a result of a calculation. From the nearfields, the theoretical farfields

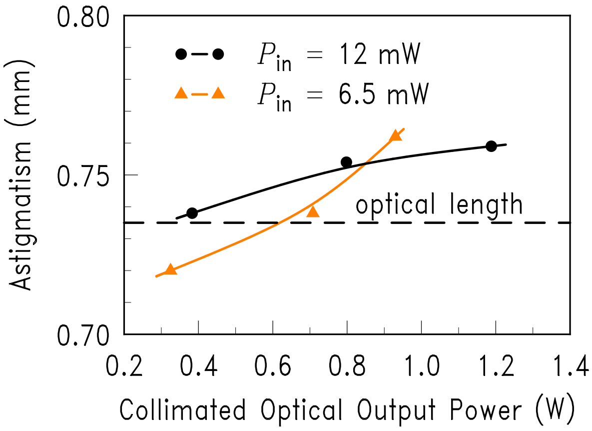

Fig. 2. Astigmatism of an amplifier with a taper length of 2.5 mm. The increase with the output power can be explained by thermal lensing.

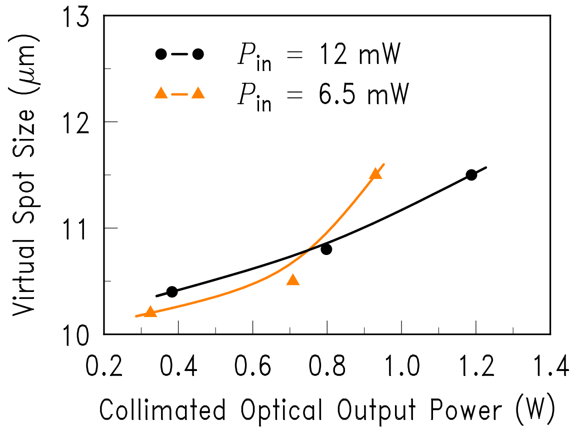

Fig. 3. The calculated $1/e^2$ virtual spot size, corresponding to the same measurement as in Fig. 2.

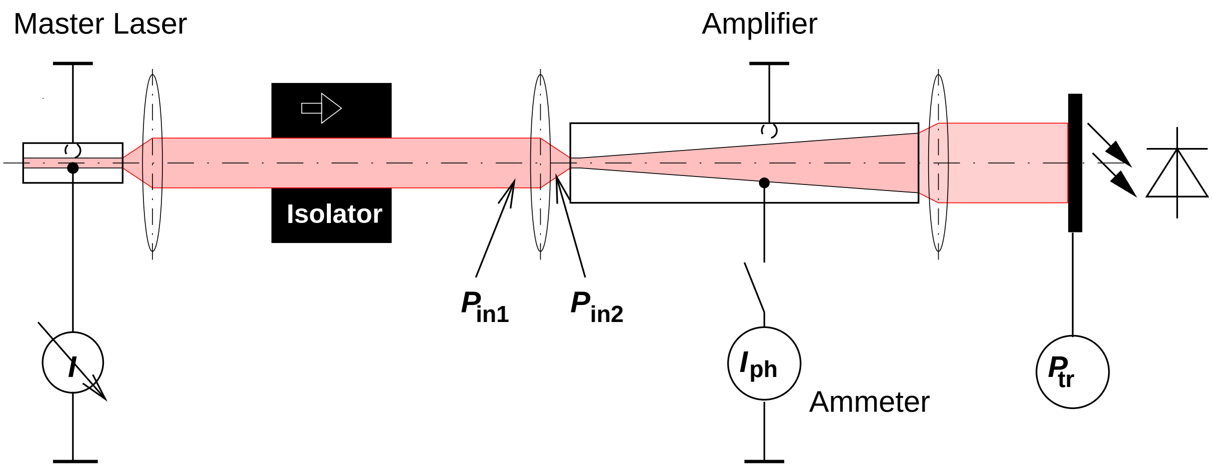

Fig. 4. Measurement setup for the evaluation of the coupling efficiency of the MOPA system

have been calculated which compared well to the experimentally achieved ones. According to Fig. 6, the sample with the broader vertical mode revealed a higher photocurrent and a higher optical transmission, both of which are evidence of a better optical coupling. This is in good agreement with the assumption, that in the vertical direction its mode has a better overlap with the still broader focal optical field. The difference appears more drastic for the transmission which in Fig. 6 has been measured at the same time with the photocurrent.

For sample B, we also measured the transmission with open contacts. The result is shown in Fig. 7. The carriers remain in device and can contribute to stimulated emission in a recycling process when the circuit is open. The result is a higher transparency in that case. Figure 8 shows that the transmission is high for small input powers, where the

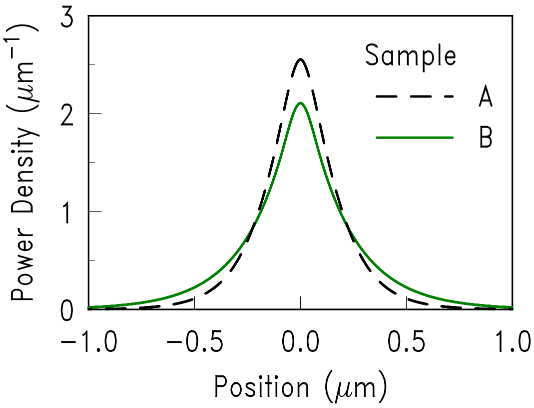

Fig. 5. The calculated vertical intensity distributions reveal a broader nearfield for Sample B.

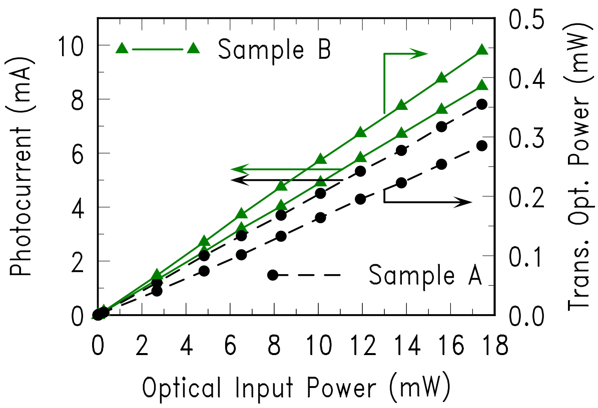

Fig. 6. The with the smaller nearfield shows a much smaller optical transmission than Sample B. The photocurrent is also less, but not that drastical.

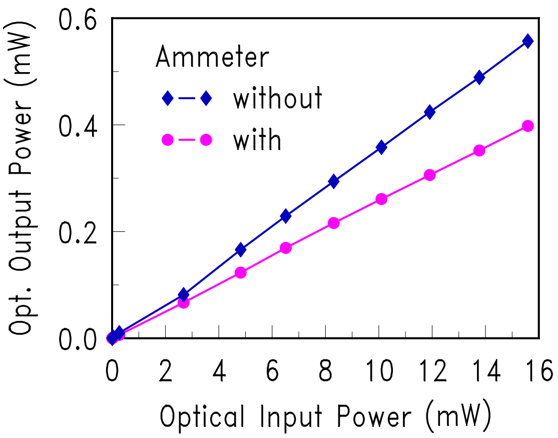

Fig. 7. The transmitted optical power is significant higher if the contacts of the amplifier are not bypassed by the amp-meter and the optical power exceeds the saturation value.

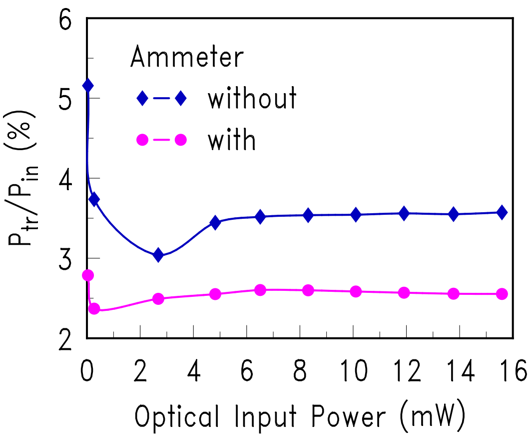

Fig. 8. Ratio of the transmitted optical power to the optical input power. The high value for very small input powers arises from the different beam properties below master laser threshold.

master laser is below threshold. With increasing power it drops to its minimum but then it increases again to stabilize at a nearly constant value.

The electrical-to-optical conversion efficiency in Fig. 9 shows reversal behavior for small optical powers, but is also nearly constant for sufficiently high optical power values. The decrease in efficiency with optical power can be explained by the lower coherence of the master laser below threshold which means the beam doesn't focus and couple as well. The upper curve in Fig. 9 shows the result of a measurement where we also considered the losses of the focusing lens, that here have been mainly aperture losses. In this way, we achieved a conversion efficiency of 80 %. We also investigated the influence of vertical

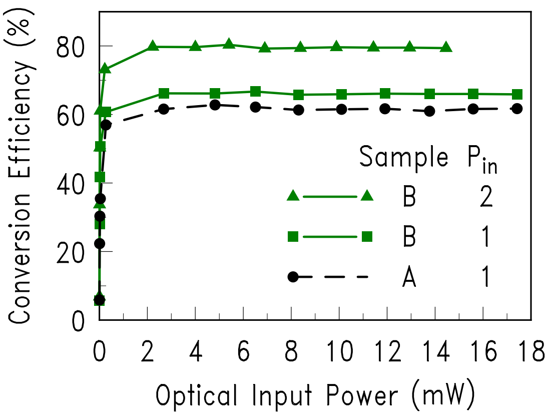

Fig. 9. Calculated optical-electrical conversion efficiency as a function of the optical input power. For the upper curve of sample B the focusing lens losses have also been taken into account. The optical input powers have been measured at the positions according to Fig. 4.

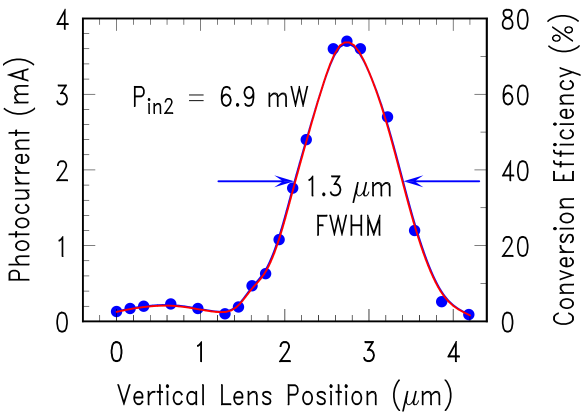

Fig. 10. The optical-electrical conversion efficiency as a function of the vertical lens position, gives evidence about accuracy requirements and the overlap of the guided wave and the focal intensity distribution.

position changes of the focusing lens, that is almost identical with the position of the focal spot. The result, which is depicted in Fig. 10, is in good agreement with the mentioned assumption, that the vertical focal width is larger than the modal widths of the vertical waveguide. The measurement also highlights the demand for high accuracy in the positioning of the optical components in a MOPA setup.

4. Fabrication of Preamplifiers

The preamplifiers of the tapered amplifiers are realized as ridge-waveguide structures. The ridge is defined by etching two 30 μm-wide trenches into the semiconductor in a two-step process, first, a dry-etching step using chemically assisted ion beam etching (CAIBE), which is followed by a wet-chemical step. In order to ensure the single-mode behavior of the lasers it is necessary to control the etch depth very exactly, because the height of the ridge defines the step in refractive index. Since the etch rate of the CAIBE system is not reproducible enough, the last 200–300 nm are etched wet chemically in a solution with a slow etch rate. The dry-etching step helps to minimize the large undercut which will occur, if only wet-chemical etching is used to fabricate the ridge. In Fig. 11, a cross section of the ridge can be seen, which is processed in the described way after removal of the photoresist.

The next process step is a complete coating of the wafer with a Si_3N_4-passivation layer with a thickness of about 250 nm. The difficulty at this point is to open a passivation window on top of the ridge. The contact area should be as large as possible in order to reduce the contact resistance. For process reliability reasons there should be also a

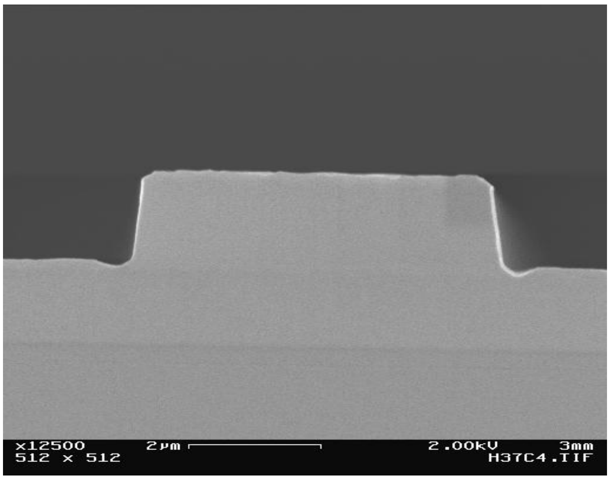

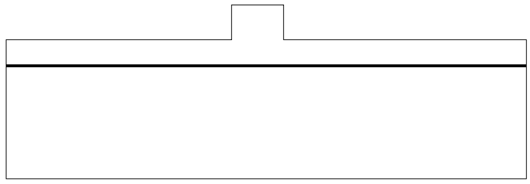

Fig. 11. Micrograph of the ridge after the complete etch process and removal of the photoresist

sufficient overlap of the passivation over the ridge. Especially for narrow ridges this is a severe problem. Additionally, it is important to adjust the passivation window right in the center of ridge in order to prevent asymmetric current injection.

For these reasons, we developed a self-aligned process for opening the passivation. As can be seen schematically in Fig. 12, in the first lithographic step, AZ1512 photoresist is deposited on the wafer with an approximately 3 μm wide trench between resist and ridge, whereby the alignment accuracy is not critical.

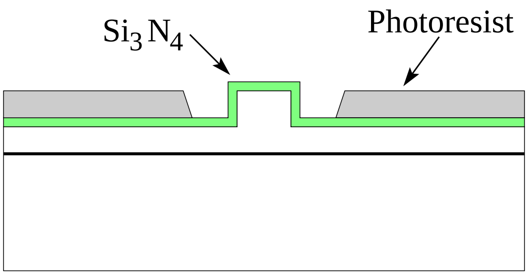

Fig. 12. Side view of the first lithography step for structuring the passivation.

Then the photoresist is baked at 170° for 15 min in order to make the photoresist stable against solvents of the subsequent process steps. The wafer is afterwards planarized with a second layer consisting of two parts photoresist AZ1512 and one part AZ-thinner. By exposing the whole wafer to an oxygen plasma the photoresist is gradually removed. The process is stopped when the topmost part of the ridge is fully uncovered (see Fig. 13). In this status the passivation can easily be etched in a CF_4 plasma and the result is a self-aligned passivation which covers most of the sidewalls of the ridge and allows a symmetric and complete current injection into the ridge. In Fig. 14, the complete passivation structure can be seen around the ridge region.

The hardbake of the photoresist of the first lithographic step as described above is necessary because the passivation at the sidewalls of the etched trenches on the opposite to

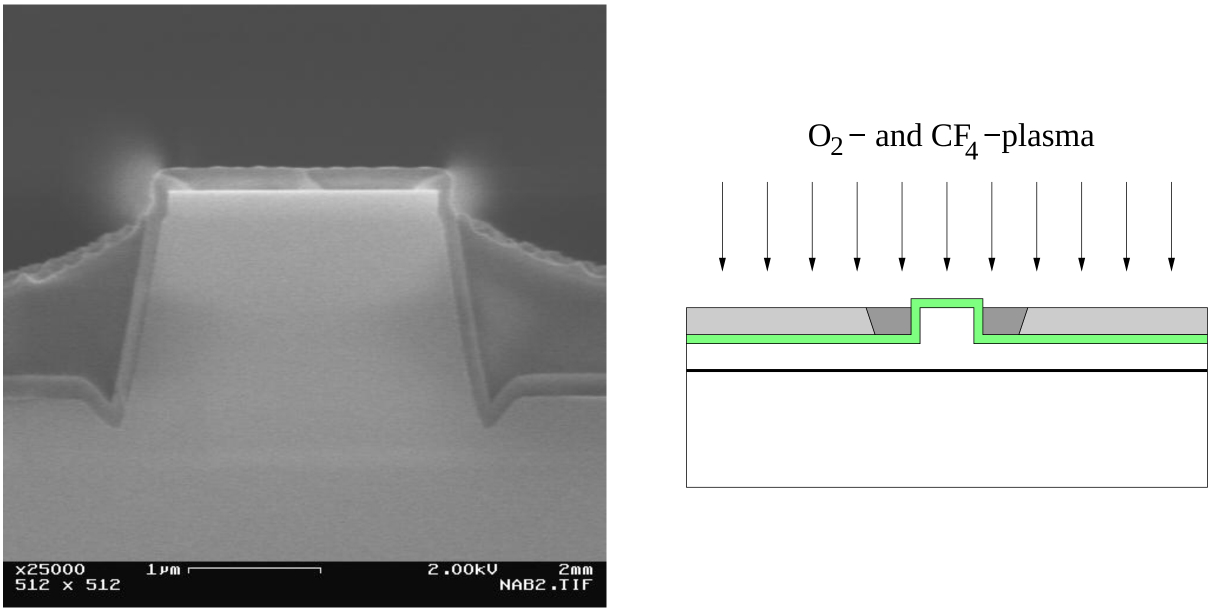

Fig. 13. Cross section of the ridge region after complete lithography for the passivation

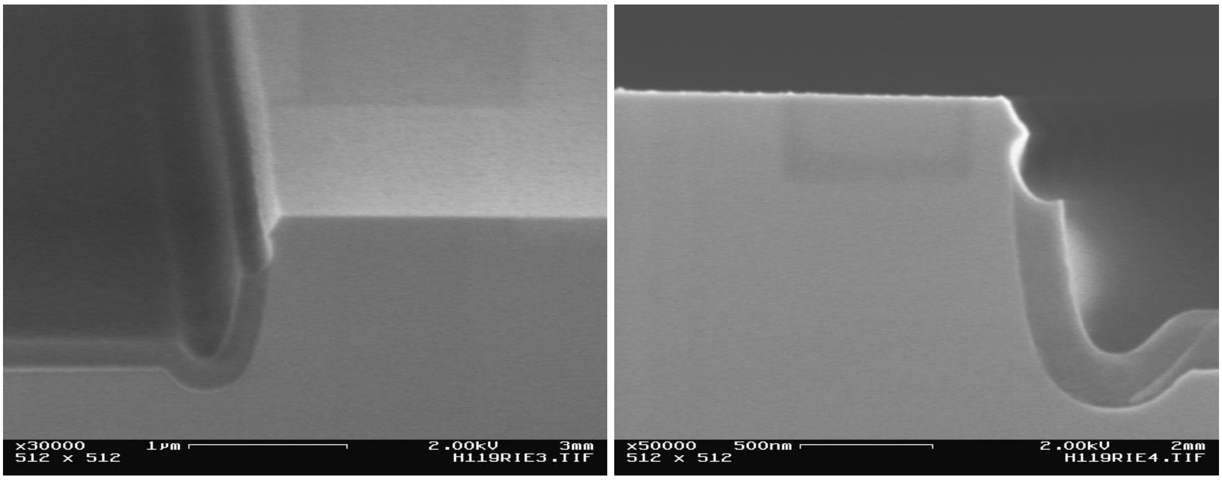

Fig. 14. Passivation after complete structuring

the ridge must not be opened. Without this hardbake the first photoresist would be partially solved by the second photoresist and the resulting resist layer would be too thin to withstand the subsequent oxygen plasma. So the passivation would be etched and finally result in a parasitic current path. But with the 170°C curing process this area can be protected as can be seen in Fig. 15.

In the last step, the electrical contacts are deposited. Again there is no need for elaborate alignment of the lithography. The contacts are formed by evaporating layers of Ti, Pt and Au. In order to facilitate the cleaving of the laser bars the contact material has to be removed from the scribing area, which is done by a lift-off process. For good heat extraction, it is additionally advisable to apply a thick Au layer. This is performed by

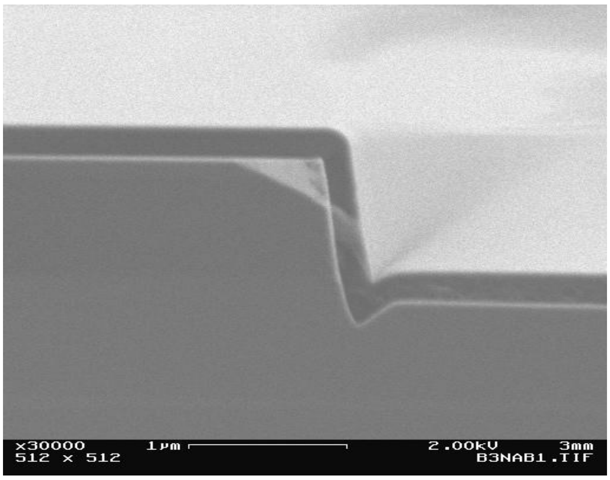

Fig. 15. Edge on the opposite to the ridge at which the passivation remains closed.

electroplating. The complete process of the p-side of the wafer can be seen in Fig. 16.

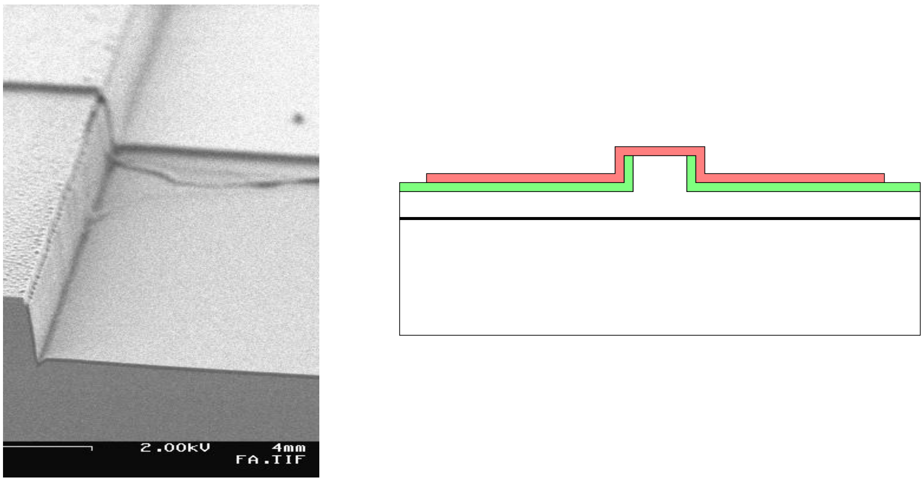

Fig. 16. Completely processed ridge-waveguide laser

After having finished the p-side, the wafer is thinned to a thickness of 100–120 μm by chemo-mechanically polishing in a H_2O_2:NH_3-solution. At last the n-contact consisting of a Ge/Au/Ni/Au-layer system is evaporated on the backside of the wafer and is annealed at 420°C in a RT-processor.

5. Conclusion

Besides the determination of the beam quality factor M^2, the measurement of the corrected far-field pattern yields information not only about the spatial beam quality, but also about the astigmatism and thermal lensing behavior of tapered-area semiconductor laser amplifiers. The approximation of the astigmatism as the optical length of the taper region is shown to be valid. The measurements of the optical-electrical conversion efficiency do not contradict with the assumption of high coupling efficiencies up to 80%. High coupling efficiencies are shown to be achieved rather by epitaxial waveguide structures with weak guiding and small vertical nearfields. The novel process we presented is particularly suitable for the fabrication of preamplifier structures to improve the device performance.

References

[1] D. Woll, B. Beier, K.-J. Boller, and R. Wallenstein, "1 W blue 465-nm radiation generated by frequency doubling of a high-power diode laser in critically phase-matched LiB_3O_5," *Optics Lett.*, vol. 24, no. 10, pp. 691–693, 1999.

[2] J. N. Walpole, "Semiconductor amplifiers and lasers with tapered gain regions," *Optical and Quantum Electron.*, vol. 28, pp. 623–645, 1996.

[3] S. Morgott, "Halbleiter-Trapezverstärker als Laserstrahlquellen hoher Brillanz," *Dissertation, Shaker Verlag Aachen*, 2000.

Unstable-Resonator Lasers Fabricated with Improved Dry-Etching Technology for Ultra-Smooth Laser Facets

Eckard Deichsel

In this article, we present the fabrication and investigation of high-brightness unstable-resonator semiconductor lasers. Details about the epitaxial growth together with results of broad-area lasers are shown. For the fabrication of the dry-etched laser mirrors, a multi-layer etch mask together with an optimized chemically-assisted ion-beam etching (CAIBE) process have been developed leading to ultra-smooth laser facets. With this technique, unstable-resonator lasers with curved mirrors have been fabricated. The devices were tested in pulsed and continuous wave operation, exhibiting high optical output powers. Corrected far fields were measured and the corresponding virtual source size was calculated to be in the range of 2 μm.

1. Introduction

Laser fabrication using dry-etching techniques offers a variety of advantages compared to the conventional fabrication process and enables many new applications. Accurate control of etching depths, lateral positions, and sidewall slopes of the etched structures are required for the ridge-waveguide laser fabrication which can be realized in a dry-etching process. Another advantage is the ability of full-wafer processing and testing that allows fabrication and characterization of lasers without separating the chips. Therefore, the manipulation of the cleaved laser bars and chips, e.g. for the mirror coating, can be reduced to a minimum. New applications become possible like the monolithic integration of a monitor photodiode allowing to control the optical output power of the laser during operation. Finally, the orientation and shapes of the mirrors are no longer dependent on the crystal orientation. This enables new laser designs including unstable resonators [1],[2], curved mirrors [3]. Many other advantages and applications are described in [4], like Fresnel lenses, 45° reflectors, microlenses, and waveguides.

However vertical, flat, smooth, and damage-free laser mirrors are necessary for good device performance. Tilted facets or corrugation of mirror surfaces lead to increased threshold currents, reduced efficiencies, and far-field distortions. Additionally, the lifetime and maximum output power of the devices may be reduced due to chemical contamination of the facets caused by the dry-etching process. All these requirements must be considered in the development of an optimized etching process.

2. Epitaxy

The epitaxial material is a MBE-grown graded-index separate-confinement heterostructure (GRINSCH). The active region is a 8-nm-thick compressively strained $In_{0.2}Ga_{0.8}As$ single quantum well, surrounded by 10-nm-thick GaAs spacing layers. The p- and n-dopants of the AlGaAs grading and cladding layers are C and Si, respectively. The emission wavelength of the laser devices is 980 nm. Details of the epitaxial growth process and the optimization of the epitaxy for high-brightness applications are described in [5].

3. Dry-Etching Process for Laser Mirrors

An improved dry-etching process has been developed for the fabrication of semiconductor laser diodes with dry-etched resonator mirrors. However, there are strict requirements for the quality of the dry-etched laser mirrors. The fabrication method of these facets includes two steps, the fabrication of a suitable etch mask and the mirror etching process itself.

As etch mask, a multilayer resist based on a thick bottom polymer, a thin SiO intermediate layer, and a photoresist on top is used. The schematic process sequence is shown in Fig. 1. It provides a stable etch mask, which fulfills the requirements for the fabrication of deep, vertical, and flat laser mirrors. After photolithography, the pattern transfer into the intermediate layer and the bottom polymer is performed by CF_4 and O_2 reactive ion etching (RIE), respectively. To improve the sidewall roughness of the etch mask, a short isotropic O_2 RIE step at higher operation pressure is used, which is prerequisite to achieve ultra-smooth dry-etched laser mirrors.

The 8-μm-deep mirrors are formed by an improved chemically-assisted ion-beam etching (CAIBE) process. Vertical, flat, and smooth facets in the semiconductor material are achieved using a substrate temperature of 75 °C, an ion energy of 400 eV, and a chlorine

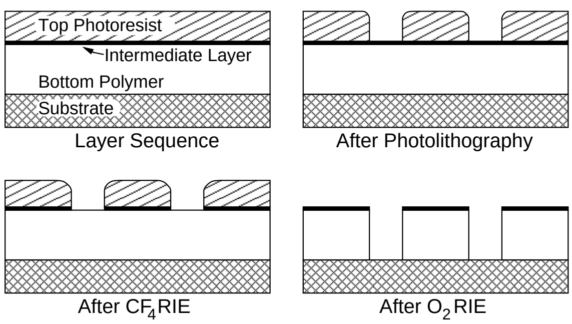

Fig. 1. Process sequence of the multilayer resist. After photolithography, the pattern transfer into intermediate layer and bottom resist is performed by CF_4 and O_2 RIE, respectively.

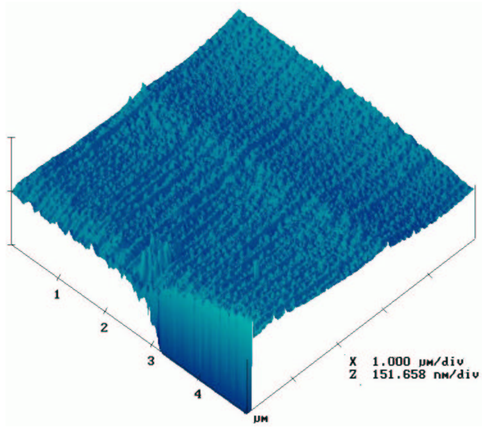

Fig. 2. The AFM characterization of a dry-etched laser mirror shows a remaining roughness of less than 5 nm (rms).

flow of 4 sccm. AFM measurements on the laser facet show a remaining roughness of 3–5 nm (rms), which is shown in Fig. 2. Details of the dry-etching process are described in [6].

4. Fabrication and Characterization of Broad-Area Lasers with Dry-Etched Mirror Facets

The gain-guided area is defined by wet-chemical etching. A SiO_2 passivation layer is deposited by plasma-enhanced chemical vapor deposition (PECVD). The p-contact window openings are defined using a CF_4 reactive ion etching (RIE) process followed by the p-contact Ti/Pt/Au metallization. These first steps are similar to the conventional fabrication of lasers.

The dry-etched mirrors require vertical, flat, and smooth facets, which can be achieved using the optimized CAIBE process together with the multilayer resist as described above. At this state of the process, first pulsed on-wafer tests can be performed and mirror coatings can be applied. Then, a thick gold layer is electroplated onto the p-contact metal to reduce thermal and electrical resistance of the devices. After substrate thinning and Ge/Ni/Au n-contact evaporation, the devices are seperated by crystal oriented cleaving.

For high-power operation, lasers fabricated with the above described process have been mounted junction-side down on diamond submounts and characterized in cw operation. The active stripe geometry is $1000\,\mu\mathrm{m} \times 100\,\mu\mathrm{m}$. As presented in Fig. 3, an optical output power of 2.59 W from the front facet of a laser with straight parallel dry-etched facets has been measured with a calibrated integrating-sphere detector. To our knowledge, this value represents the highest cw output power from a dry-etched laser facet. Additionally, it should be emphasized that no protective facet coating has been deposited onto the laser mirrors. The corresponding wall-plug efficiency for both facets is over 55 % in the range between 1 and 3 A. Lasers with cleaved facets and identical geometry have been fabricated from the same epitaxial wafer material. For comparison, the output power characteristic of a laser of this type is plotted in Fig. 3 as a dashed line. No significant differences can be noticed when comparing lasers with cleaved and dry-etched facets under these conditions.

With this technique, lasers with monolithically-integrated monitor diodes have also been fabricated and tested. The measured current of the monitor diode behaves almost linear to the output power of the laser diode and allows the monitoring of the laser during operation. Details of the characterization are already published in [7].

Dry-etched resonator mirrors are independent of shape and crystal orientation of the mirrors, which allows the fabrication of unstable resonator lasers with curved mirrors. Figure 4 shows the dry-etched curved facet of an unstable resonator laser.

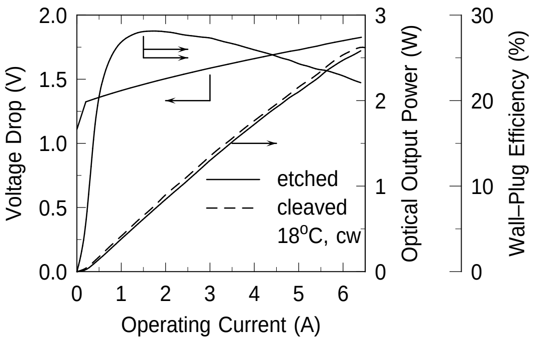

Fig. 3. Optical front-facet output power, voltage drop, and wall-plug efficiency of a $1000\,\mu\mathrm{m} \times 100\,\mu\mathrm{m}$ broad-area laser with dry-etched facets (solid lines). For comparison, the output power characteristic of a laser with cleaved facets is also plotted (dashed line).

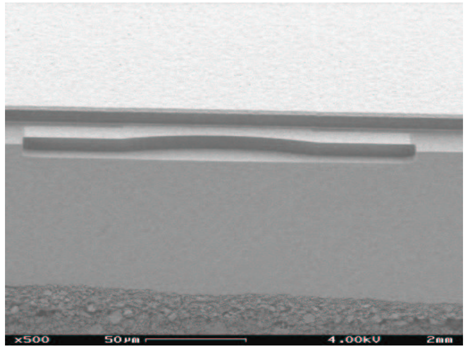

Fig. 4. SEM micrograph of the curved facet of an unstable-resonator laser with a mirror curvature radius of $250\,\mu\mathrm{m}$.

5. Unstable Resonator Lasers

Unstable resonators with curved mirrors have been fabricated and mounted p-side up on heat sinks. The devices are uncoated and all results refer to the front output facet. Figures 5 and 6 show the L–I curves of unstable-resonator lasers with an active-region geometry of $500\,\mu\mathrm{m} \times 100\,\mu\mathrm{m}$ in pulsed and cw operation, respectively. The concave mirrors are located symmetrically on both ends of the laser with curvature radii of 250, 500, 1000, and $2000\,\mu\mathrm{m}$ and corresponding magnifications of 34, 14, 7, and 4, respectively. For comparison a broad-area laser with the same dimensions and two cleaved mirrors is also shown.

With increasing magnification, the loss per round trip of the unstable resonators also increases, which leads to reduced output powers for the lasers with smaller mirror curvature radii. This effect is stronger for the cw measurements than for the measurements in pulsed operation. This can be explained by heating effects, which are reduced by mounting the devices p-side down on diamond heat spreaders. Additional AR/HR coatings can also increase the output power.

The corrected far fields were recorded in cw operation at room temperature using an imaging lens at the focal distance away from the output facet. Thus, the beam is collimated in vertical direction, however due to the strong astigmatism of the unstable resonator lasers an image of the virtual source is achieved in the plain of the corrected far field. This is shown in Fig. 7 for the device with $500\,\mu\mathrm{m} \times 100\,\mu\mathrm{m}$ active-stripe geometry and a mirror curvature radius of $1000\,\mu\mathrm{m}$. The corrected far fields for the other lasers with different mirror curvatures are comparable. Currents below threshold lead to wide corrected far fields, due to the spontaneous emission. With increasing current, the width of corrected far field narrows to a minimum value around laser threshold and raises again for increasing currents.

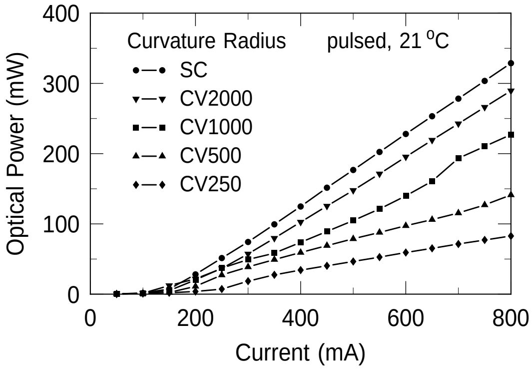

Fig. 5. *L–I* curves in pulsed operation of unstable-resonator lasers with curved mirrors on both sides. The geometry of the active region is $500\,\mu$m $\times 100\,\mu$m. The mirror curvature radii R are 250, 500, 1000, and $2000\,\mu$m. For comparison a laser with two cleaved ends (SC) is also shown.

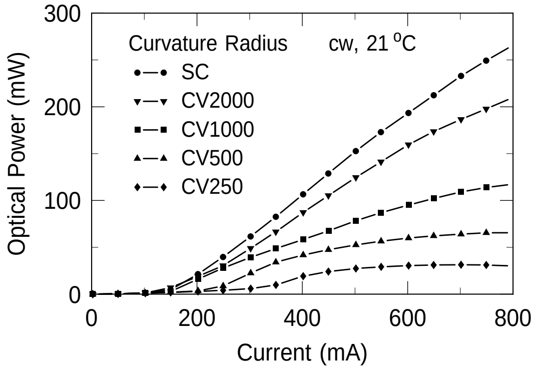

Fig. 6. Same lasers as in Fig. 5 but in cw operation at room temperature.

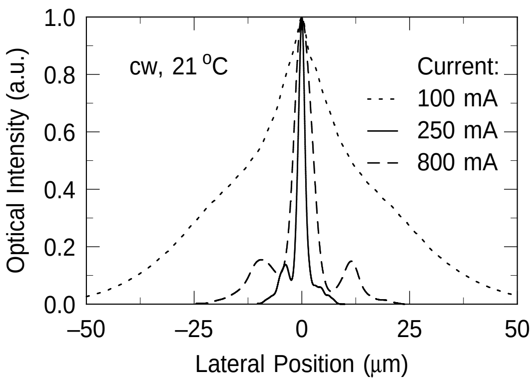

Fig. 7. Corrected far field of the device with $500\,\mu$m $\times$ $100\,\mu$m active stripe geometry and $1000\,\mu$m mirror curvature radius for different currents in cw operation.

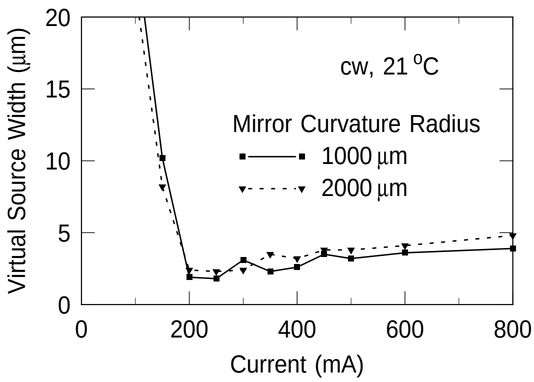

Fig. 8. Virtual source sizes in dependency of the operating current of the laser from Fig. 7 measured in cw operation. Additionally the results of the laser with $2000\,\mu$m mirror curvature radius are shown.

The width of the virtual source can be calculated from the data of the corrected far fields using the lens equation. Figure 8 shows the virtual source widths of the devices with 1000 and $2000\,\mu$m mirror curvature radii for different currents in cw operation. The minimum virtual source width of the $2000\,\mu$m device is $2.3\,\mu$m at laser threshold and increases to $4.8\,\mu$m for 800 mA pump current. The laser with $1000\,\mu$m mirror curvature shows slightly decreased values, but at reduced output powers. The minimum value around threshold is less than $2\,\mu$m. In this case the power in the central lobe is more than 70 % of the total output power of the laser. For increasing currents this value decreases and is around 65 % for 800 mA pumping current. Devices with smaller mirror curvatures show also very narrow virtual source sizes, however with poor cw-operation behaviour.

6. Conclusion

An improved dry-etching process for ultra-smooth dry-etched laser mirrors is prerequisite for the fabrication of unstable-resonator devices. Lasers with straight dry-etched mirrors show output powers comparable to devices with cleaved facets fabricated out of the same epitaxial material and with same dimensions. Unstable resonators with different mirror curvature radii were tested in pulsed and cw operation. Single-lobed corrected far fields were achieved with minimum virtual source sizes around 2 μm.

References

[1] M. L. Tilton, G. C. Dente, A. H. Paxton, J. Cser, R. K. DeFreez, C. E. Moeller, and D. Depatie, "High power, nearly diffraction-limited output from a semiconductor laser with unstable resonator," *IEEE J. Quantum Electron.*, vol. 27, no. 9, pp. 2098–2108, 1991.

[2] S. A. Biellak, C. G. Fanning, Y. Sun, S. S. Wong, and A. E. Siegman, "Reactive-ion-etched diffraction-limited unstable resonator semiconductor lasers," *IEEE J. Quantum Electron.*, vol. 33, no. 2, pp. 219–230, 1997.

[3] P. Unger, V. Boegli, P. Buchmann, and R. Germann, "Fabrication of curved mirrors for visible semiconductor lasers using electron beam lithography and chemically assisted ion-beam etching," *J. Vac. Sci. Technol. B*, vol. 11, no. 6, pp. 2514–2518, 1993.

[4] P. P. Deimel, "Micromachining processes and structures in micro-optics and optoelectronics," *J. Micromech. Microeng.*, vol. 1, pp. 199–222, 1991.

[5] R. Jäger, J. Heerlein, E. Deichsel, and P. Unger, "63% wallplug efficiency MBE grown InGaAs/AlGaAs broad-area laser diodes and arrays with carbon p-type doping using CBr_4," *J. Crystal Growth*, vol. 201/202, pp. 882–885, 1999.

[6] E. Deichsel, R. Jäger, and P. Unger, "High-brightness lasers fabricated with improved dry-etching technology for ultra-smooth laser facets," *Microprocess and Nanotechnology Conference*, Shimane, Japan, 2001.

[7] E. Deichsel, F. Eberhard, R. Jäger, and P. Unger, "High-power laser diodes with dry-etched mirror facets and integrated monitor photodiodes," *IEEE J. Selected Topics Quantum Electron.*, vol. 7, no. 2, pp. 106–110, 2001.

Optical Coatings for Laser Facets Fabricated by Reactive Ion-Beam Sputter Deposition

Steffen Lorch

Reactive ion-beam sputter deposition is the best method to fabricate stoichiometric and dense layers for optical coatings with very low optical absorption. The refractive indices and the thicknesses of such multilayers can be optimized to get the required reflectivities for antireflection-/high-reflection-coatings on laser facets or antireflection coatings lower than 10^{-4} *for laser amplifiers. The characterization can be done using the threshold shift or the Hakki-Paoli method.*

1. Introduction

Optical coatings are used for adjustment of facet reflectivity R and for passivation. For conventional semiconductor lasers, an antireflection-/high-reflection-coating (AR/HR with $R = 10\% / 90\%$) is used. For laser amplifiers, an antireflection (AR) coating with a very low reflectivity ($R < 10^{-4}$) is needed. Due to the high intensity on the output facet, the coating becomes hot and can be destroyed by catastrophic optical mirror damage (COMD). This can be reduced by a low optical absorption in the coating, which can be realized with very dense and stoichiometric oxide layers. The best method to fabricate such optical coatings is reactive ion-beam sputter (RIBS) deposition with an assisted ion beam.

2. Fabrication

The aim is to fabricate optical layers for lasers or laser amplifiers with very low optical absorption and a good reproducibility. There are a lot of possibilities to fabricate such layers. An old and often used method is thermal deposition with or without an electron beam. Using this method, the layers have very low densities. The kinetic energy of thermally evaporated material is very low (much lower than 1 eV) and the mobility on the substrate is too low to build stoichiometric and dense layers. The packing density may be lower than 50%, the layers are very rough and moisture can diffuse into the cavities. Such layers show high optical absorption and scattering. The mobility of the deposited material can be increased using a higher substrate temperature, but the required temperature is too high (sometimes higher than 800 °C) and the substrate may be destroyed. The mobility can also be increased with ion assisted deposition (IAD) or ion plating (IP) but here the layers may be damaged by the ions and the optical absorption as well as scattering in the layers is high. Another possibility is the deposition of sputtered material using a conventional parallel-plate reactor. But in this way, the substrate is in direct contact with the plasma which also leads to damage. Additionally, the starting conditions may cause problems for the deposition. The ion-beam sputter (IBS) deposition uses an ion beam to sputter a target and this material is deposited on the substrate. Here, the parameters for the plasma, the beam, and the chamber pressure can be varied independently in a wide range. Also, the starting conditions are always the same due to the fact that the deposition does not starts until all conditions are stable and a good reproducibility is achieved. With such a sputter system, it is possible to fabricate layers with very low optical absorption because the energy of the sputtered material is high enough (2–4 eV) and the mobility is sufficient to build layers with a high density. Additionally, oxygen should be introduced in the chamber to get stoichiometric oxide layers [1]. An optical absorption in the deposited layers of less than 10 ppm may be achieved with such a system.

There are different types of ion-beam sources. The oldest one is the Kaufman source, where the plasma is sustained by electron emission and a magnetic field. These sources have a very low lifetime because the filaments must be replaced often. The electron cyclotron resonance (ECR) sources do not have a filament and so they have a long lifetime. However, the ECR sources need a matching network for a proper microwave coupling and so they are rather sophisticated to use. The newest type of sources are the inductively coupled plasma (ICP) or radio frequency (RF) sources. Here, the plasma is induced by a magnetic field. These sources also have a very long lifetime and do not need a matching network to operate. The ions (argon is normally used) are extracted by a two- or three-grid ion optic. The ion beam is positively charged and the beam must be neutralized with electrons to avoid the charging of the target. Cathode filament, hallow cathode, or plasma bridge neutralizer are commonly used [2].

3. Theory

In Fig. 1, a coating with n layers on a semiconductor substrate is schematically shown. The particular layer r has the refractive index n_r and the thickness d_r. The light strikes the coating under an angle θ.

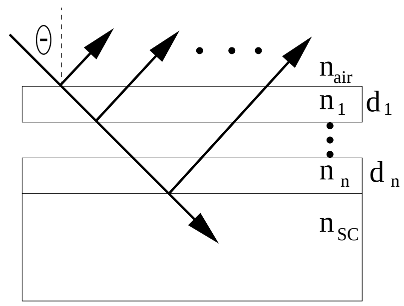

Fig. 1. Multilayer coating on a semiconductor substrate with refractive indices n and thicknesses d. The light strikes the surface under an angle of incidence θ.

Such a multilayer can be characterized [3] by the matrix equation

$$\begin{pmatrix} B \\ C \end{pmatrix} = \left[\prod_{r=1}^{n} \begin{pmatrix} \cos\delta_{\mathrm{r}} & (i\sin\delta_{\mathrm{r}})/\eta_{\mathrm{r}} \\ i\eta_{\mathrm{r}}\sin\delta_{\mathrm{r}} & \cos\delta_{\mathrm{r}} \end{pmatrix} \right] \begin{pmatrix} 1 \\ \eta_{\mathrm{SC}} \end{pmatrix} \tag{1}$$

with the phase thicknesses $\delta_{\mathrm{r}} = \frac{2\pi\eta_{\mathrm{r}} d_{\mathrm{r}} \cos\theta}{\lambda}$ and the admittances $\eta_{\mathrm{TE}} = n\sqrt{\frac{\epsilon_0}{\mu_0}}\cos\theta$ and $\eta_{\mathrm{TM}} = n\sqrt{\frac{\epsilon_0}{\mu_0}}/\cos\theta$, respectively. With the admittance $Y = \frac{C}{B}$, the reflection factor $R = \left(\frac{\eta_{\mathrm{air}}-Y}{\eta_{\mathrm{air}}+Y}\right)^2$ can be calculated.

For a single-layer coating, the matrix equation can be calculated easily. For a given semiconductor material (e. g. GaAs $n_{\mathrm{SC}} = 3.4$) the deposited layer must have a refractive index of $n_1 = \sqrt{n_{\mathrm{SC}} n_{\mathrm{air}}} = 1.84$ and a thickness of $d_1 = \frac{\lambda_0}{4n_1} = 128\,\mathrm{nm}$ for a wavelength $\lambda_0 = 945\,\mathrm{nm}$. But with such a single-layer coating, the reflectivity is only $R = 0$ for the design wavelength $\lambda = \lambda_0$ and an incident angle of $\theta = 0$ (see Fig. 2).

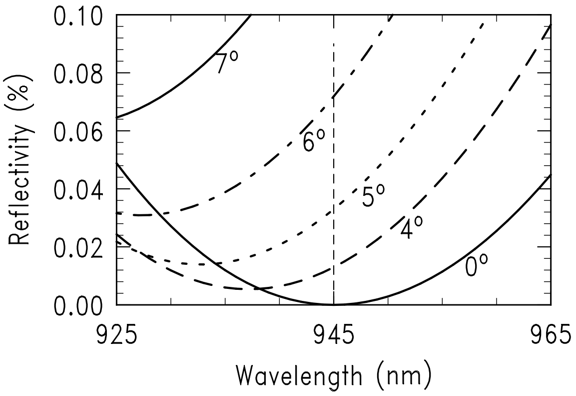

Fig. 2. Reflectivity R over wavelength λ of a single-layer coating with different incident angles θ.

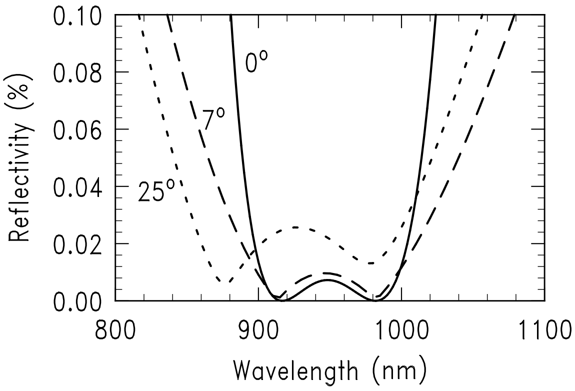

Fig. 3. Reflectivity R over wavelength λ of an 4-layer coating with different incident angles θ.

4-layer coatings are often used. The reflectivity increases much slower for increasing incidence angle θ than for a single-layer coating. Also the bandwidth is much larger compared to a single-layer coating. The reflectivity of such a 4-layer coating is shown in Fig. 3. The advantage of multilayer coatings is the possibility to individually optimize the thickness of each layer to achieve the required reflectivity. So, given materials with fixed and exact characterized refractive indices can be used.

4. Realization of a Sputter Deposition System

In our application, an reactive ion-beam sputter deposition system (RIBS) will be constructed. The first step is to build a system with one inductively coupled plasma (ICP) ion-beam source and a cubic target holder with four targets. The ion beam is neutralized by a filamentless bridge neutralizer (FBN). Additionally, oxygen is introduced into the chamber for the oxidation of the layers and the targets [1]. The setup of the system is shown in Fig. 4.

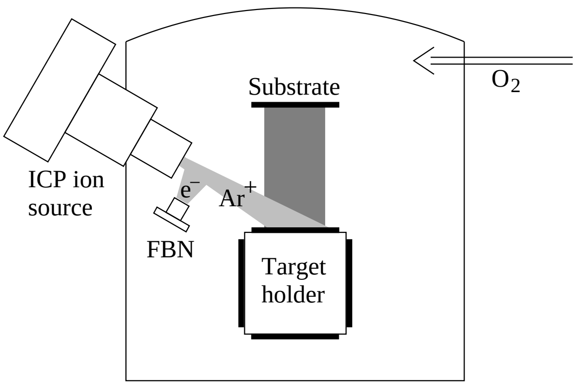

Fig. 4. RIBS system with one ion-beam source.

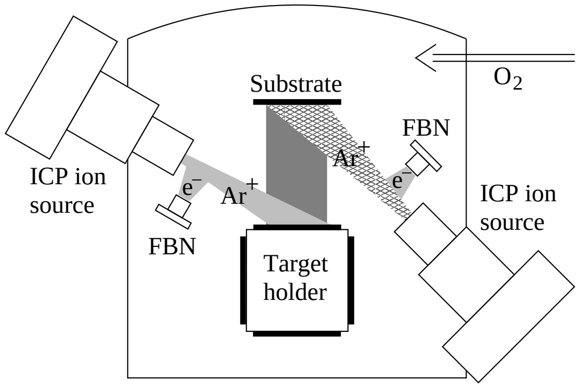

Fig. 5. RIBS system with two ion-beam sources.

The next step will be the use of a second ICP ion-beam source as shown in Fig. 5. With the implementation of a second ion-beam source, the deposition of the layers can be assisted to get higher densities with lower optical absorption. Also, the substrate can be cleaned before the deposition to avoid an oxide layer at the interface between substrate and coating layer. Different target materials will be examined. There are a lot of materials which can be used for sputter deposition. A lot of work has been done on SiO_2, TiO_2, and Al_2O_3. Also materials like Ta_2O_5, HfO_2, and Y_2O_3 can be used [4, 5].

5. Characterization

The deposited layers can be characterized in different ways. A first short characterization can be done with an ellipsometer to obtain the thickness and the refractive index. With the photo thermal deflaction (PTD), the absorption coefficient can be determined more exactly [6, 7]. For the characterization of an entired multi-layer coating on a laser facet, two methods will be described below.

A) Threshold shift

A laser (GaAs/AlGaAs) with cleaved facets has a reflectivity of around 30%. If one facet is coated with an antireflection coating, the threshold current I_{th} increases. Knowing the reflectivity R_1 of the cleaved facet, the threshold current I_{th}, the length of the laser L, and the gain Γg_0, the reflectivity of the coated facet R_1^* can be calculated according to:

$$R_1^* = R_1 \left(\frac{I_{\mathrm{th}}}{I_{\mathrm{th}}^*} \right)^{2L\Gamma g_0} \tag{2}$$

But if the reflectivity is very low ($< 10^{-2}$), this method is not exact enough, however, it is sufficient for AR/HR coatings of lasers with reflectivities of e. g. 10% and 90%. The principle of this characterization method [8] is shown in Fig. 6.

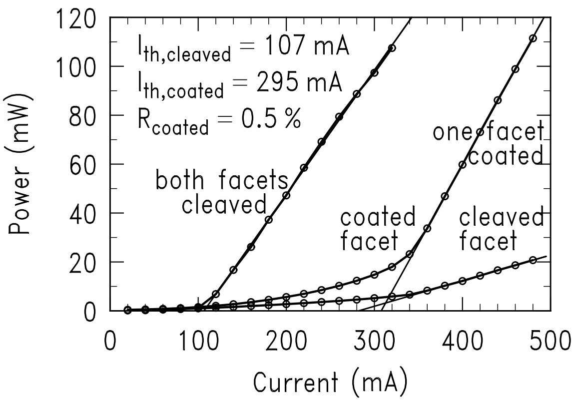

Fig. 6. Facet reflectivity calculated by the threshold shift.

B) Hakki-Paoli method

The Hakki-Paoli method [9, 10] uses the modulation $m = \frac{P_{\max}-P_{\min}}{P_{\max}+P_{\min}}$ with $m = \frac{2a}{1+a^2}$ of the intensity I over the wavelength λ. If the reflectivity R_1 of the cleaved facet is known, the reflectivity R_1^* of the coated facet can be calculated with:

$$R_1^* = a^2 R_1 \tag{3}$$

The modulation is measured with a current as high as the threshold current of the uncoated laser. This method is shown in Figs. 7 and 8.

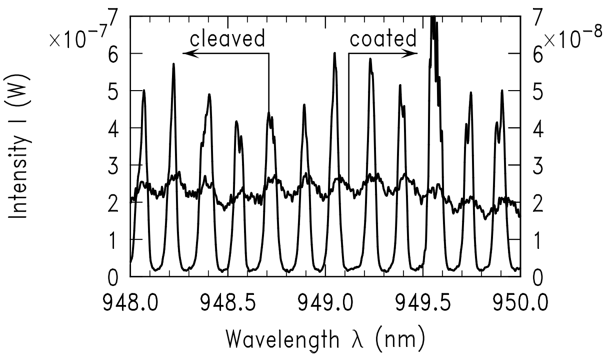

Fig. 7. Modulation m of intensity I with current at threshold of a laser with cleaved facets.

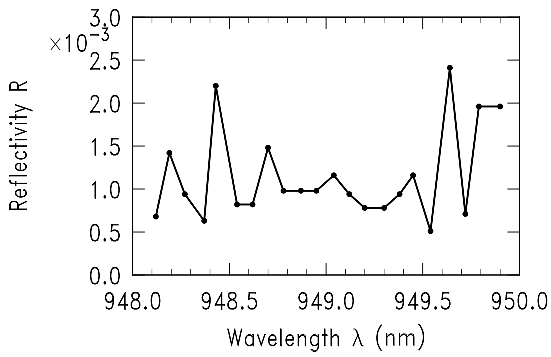

Fig. 8. Facet reflectivity R calculated by Hakki-Paoli method.

6. Conclusion

To fabricate optical coatings with low optical absorption and good reproducibility, a reactive ion-beam sputter deposition system with a second ion source for deposition assistance and pre-cleaning should be used. Different materials will be examined and composed to multilayer coatings. It should achieve an optical absorption less than 10 ppm for single layers. With photo thermal deflaction and the Hakki-Paoli method, the deposited layers can be characterized exactly enough. It should be possible to fabricate antireflection coatings with a reflectivity less than 10^{-4}.

References

[1] M. Tilsch, "Eigenschaften ionenstrahlgesputterter optischer SiO_2- und TiO_2-Schichten bei unterschiedlichen Wachstumsbedingungen und Veränderungen bei thermischer Nachbehandlung," *PhD Thesis, University of Darmstadt*, 1997.

[2] H.R. Kaufman and R.S. Robinson, "Operation of broad-beam sources," *Commonwealth Scientific Corporation*, 1987.

[3] H.A. MacLeod, "Thin-film optical filters, 2nd edition," *Adam Hilger Ltd., Bristol*, 1986.

[4] M. Varasi, C. Misiano, and L. Lasaponara, "Deposition of optical thin films by ion beam sputtering," *Thin Solid Films*, vol. 117, pp. 163–172, 1984.

[5] D. Ristau, X.C. Dang, and J. Ebert, "Interface and Bulk Absorption of Oxide Layers and Correlation to Damage Threshold at 1.06 μm," *Manuscript, Institute of Quantum Optics, University of Hannover*, vol. 19, no. 4, pp. 493–495, 1985.

[6] V. Scheuer, "Untersuchungen zu den Ursachen der Absorption in oxidischen ionenstrahlgesputterten optischen Schichten," *PhD Thesis, University of Darmstadt*, 1994.

[7] P.A. Temple, "Thin Film Absorptance Measurements Using Laser Calorimetry," *in E.D. Palik, Handbook of Optical Constants of Solids, Academic Press, Orlando*, 1985.

[8] G. Jost, "Hochleistungs-Laserverstärker auf der Basis von InGaAs-AlGaAs-GaAs," *PhD Thesis, Optoelectronics Department, University of Ulm*, 2000.

[9] B.W. Hakki and T.L. Paoli, "Gain spectra in GaAs double-heterostructure injection lasers," *J. Appl. Phys.*, vol. 46, no. 3, pp. 1299–1306, 1974.

[10] I.P. Kaminow, G. Eisenstein, and L.W. Stulz, "Measurement of the Modal Reflectivity of an Antireflection Coating on a Superluminescent Diode," *IEEE J. Quantum Electron.*, vol. 19, no. 4, pp. 493–495, 1983.

Blue-green Emitting Semiconductor Disk Lasers with Intra-Cavity Frequency Doubling

Eckart Schiehlen and Michael Riedl

Diode-pumped semiconductor disk lasers, also referred to as VECSEL (Vertical External Cavity Surface Emitting Laser), show excellent beam characteristics in combination with high output powers. Current injection inhomogeneities as in VCSELs (Vertical Cavity Surface Emitting Lasers) can be overcome as well as problems potentially caused by high optical intensity at the facets of edge-emitting lasers. A nonlinear crystal was introduced into the external cavity for frequency doubling (Second Harmonic Generation, SHG). Using non-linear crystal material Lithium Triborate (LBO) we achieved 16 mW of coherent blue-green light at a wavelength of 490nm, which is to our knowledge the highest reported value for a frequency doubled semiconductor disk laser.

1. Introduction

Based on the principle of diode-pumped solid-state disk lasers, diode-pumped semiconductor disk lasers have been reported recently [1]. This relatively new type of laser is also referred to as VECSEL (Vertical External Cavity Surface Emitting Laser). Any conventional direct semiconductor material can be used for this type of laser. In this paper, we present an InAlGaAs-based semiconductor disk laser without any additional phosphorus containing layers for strain compensation. Semiconductor disk lasers show very good beam characteristics in combination with high output powers. Because of the disk geometry, a nearly one-dimensional heat flow can be assumed. This allows power scaling by a simple enlargement of the active area.

As for all semiconductor lasers, the emission wavelength can be chosen by the epitaxial design. There is no limitation to discrete emission lines as for commonly used solid-state laser gain material (i.e. Nd:YAG). In addition to this, the semiconductor material's absorption spectrum is broad and the absorption coefficient is much higher. Therefore, no multi-pass pump optic is required.

Electrically pumped single-mode VCSELs (Vertical Cavity Surface Emitting Lasers) show an almost perfect beam profile, but the maximum single-mode output power is limited to approximately 6 mW at present time [2],[3]. When exceeding the power range of a VCSEL by increasing the active area, higher order transverse modes are observed [4], which can be explained by inhomogeneous current injection and the lack of transverse mode discrimination.

Edge-emitting lasers do not emit in the fundamental axial and transverse mode at high optical output power [5] because of inhomogeneous electrical pumping, spatial hole burning, short axial mode distance, and thermal effects inside the active region. Inevitable intensity variations inside the laser diode (filamentations) are primary responsible for Catastrophic Optical Mirror Damage (COMD). COMD occurs suddenly and destroys the laser diode facet. Moreover, the beam profile of edge-emitting lasers is highly asymmetric and tends to higher order modes at high output powers.

In contrast to other semiconductor lasers, semiconductor disk lasers have an external cavity which can be equipped with various intra-cavity elements e.g. for frequency selection or frequency conversion. Additionally, the high intra-cavity power is advantageous for frequency conversion processes using non-linear optical crystals.

Based on the InAlGaAs material system, we present a disk laser oscillating in the TEM_{00} mode with a maximum output power of 0.25 W in continuous wave (CW) operation. Our semiconductor disk laser is pumped by a commercial 1.5 W 808 nm high-power broad-area laser diode. The output beam shows a circular symmetric Gaussian intensity distribution, the beam propagation factor M^2 was measured to be < 1.1, depending on the mirror adjustment. The high single-mode fiber coupling efficiency of more than 70 % also indicates the very good focusability of the beam.

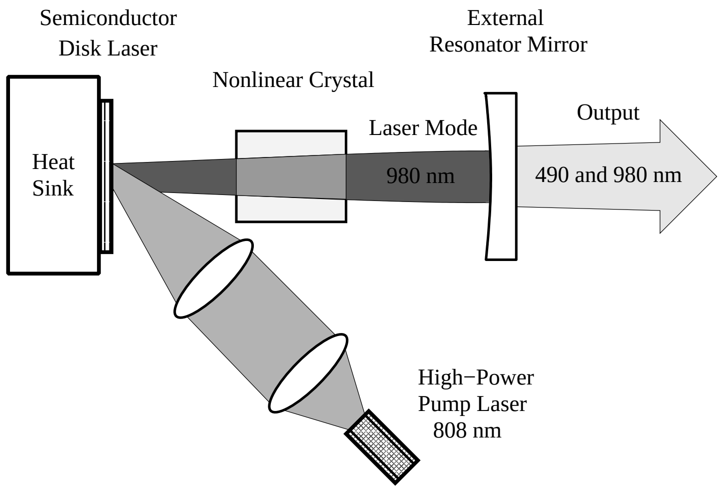

Fig. 1. Schematic setup of a diode-pumped semiconductor disk laser. The laser cavity is formed by a Bragg mirror and an external concave dielectric mirror. Pumping of the gain medium (InGaAs quantum wells) is done optically by a laser beam. A nonlinear crystal is placed inside the external cavity for frequency doubling.

As shown in Fig. 1, the semiconductor chip is mounted on a heat sink and forms a resonator together with an external concave mirror. The laser pump beam is focused onto the chip at an angle of about 45°, and should ideally result in a round spot. A non-linear optical crystal is placed inside the external cavity for frequency doubling.

The laser cavity is formed by an AlAs/GaAs Bragg mirror (distributed Bragg reflector, DBR) which is grown directly on the GaAs substrate and an external concave dielectric mirror. Because of the short gain medium length, the external mirror reflectivity has to be $\sim 99\,\%$. The Bragg mirror should exceed $99.9\,\%$ to avoid additional losses. A stable concentric (hemispheric) resonator configuration is used here. The length of the laser cavity is variable and is mainly given by the mirror radius. The epitaxial structure is a classical Resonant Periodic Gain (RPG) structure [6],[7].

2. Epitaxial Design

The gain is provided by 12 8 nm-thick compressively strained $In_{0.2}Ga_{0.8}As$ quantum wells in the antinodes of the standing wave pattern, separated by (Al)GaAs pump light absorbing layers. Electron-hole pairs are generated by absorption of the pump light in the (Al)GaAs absorbing layers and relax into the InGaAs quantum wells where they undergo stimulated emission. The very strong absorption coefficient of the semiconductor material yields to short absorption lengths for the pump light of only a few microns. The absorbing layers are realized as GRaded-INdex (GRIN) areas to support carrier movement into the quantum wells. A standing wave builds up within the resonator with the intensity maxima located in the quantum-well regions. A surface barrier made of AlGaAs with an Al content of $30\,\%$ prevents excited carriers from recombining at the wafer surface. This surface barrier layer is transparent for the pump wavelength. Optical free-carrier absorption (of photons at the emission wavelength) is kept to a minimum since the epitaxial layers are not intentionally doped. The monolithically grown Bragg mirror consists of 30 pairs of alternating AlAs/GaAs layers with a thickness of $\lambda_0/4n$.

3. Processing and Mounting

For semiconductor disk lasers, no lateral (lithographic) patterning is necessary. Grown by molecular beam epitaxy (MBE), the wafer surface is coated by a dielectric antireflection coating. The substrate is thinned to $\sim 60\,\mu$m, metallized with Ti/Pt/Au layers and chips with the desired size are cleaved. Using Indium solder, these chips directly are bonded to a copper heat sink. No electric contacts are necessary, so no additional heat originating from the ohmic contacts is generated which would raise the device temperature and reduce the conversion efficiency.

4. Experimental Results

In continuous wave (CW) operation, we achieve 0.25 W in the fundamental transverse mode using an external mirror with a reflectivity of $R = 99.5\,\%$ and a radius of curvature of $R_C = 50\,$mm. Figure 2 shows the output characteristic in TEM_{00} mode operation.

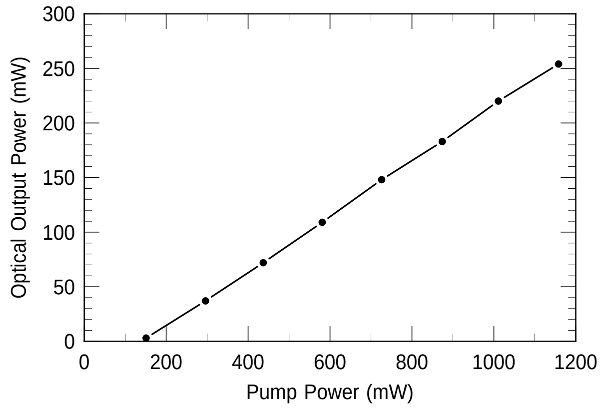

Fig. 2. Continuous-wave output characteristic of a semiconductor disk laser in TEM_{00} mode operation.

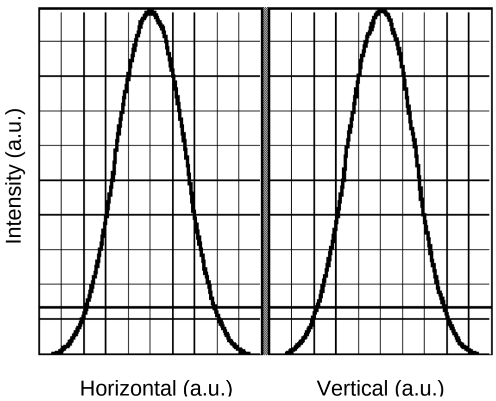

Fig. 3. Optical far-field intensity distribution of a semiconductor disk laser in the horizontal and vertical plane in TEM_{00} mode operation. The measured intensity distributions fit to a Gaussian distribution very well. The ellipticity was measured to be 0.989.

The peak wavelength is around $\lambda = 972\,\text{nm}$. The diameter of the laser-active area is estimated to be $80\,\mu\text{m}$. The optical far-field intensity distribution in the horizontal and vertical plane is shown in Fig. 3. The measured intensity distributions fit to a Gaussian distribution very well. The ellipticity was measured to be 0.989.

The collimated semiconductor disk laser beam has been coupled into a $5.9\,\mu\text{m}$ core 980 nm single-mode fiber. Using a single aspheric lens, we achieve a coupling efficiency of $> 70\,\%$ for all the measured data points (see Fig. 4).

For 490 nm blue-green light generation, a 5 mm-long Type-I critically phase matched non-linear Lithium Triborate crystal (LBO) is used. For the doubling process, it is necessary to achieve and maintain laser operation in linear polarization. We have observed that the polarization of semiconductor disk lasers may change but can be affected by the external

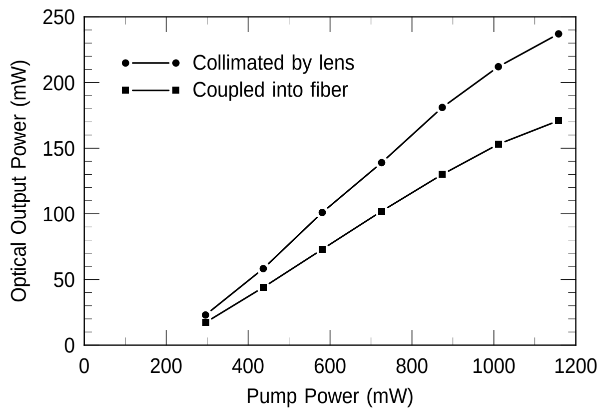

Fig. 4. Coupling of the disk laser beam into a 5.9 μm-core 980 nm single-mode fiber. The coupling efficiency is $> 70\,\%$.

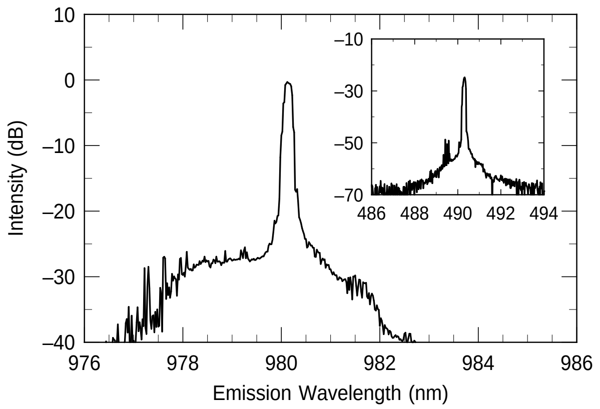

Fig. 5. Fundamental and second harmonic spectrum of a frequency doubled semiconductor disk laser. As non-linear optical crystal, LBO is used.

mirror adjustment. The fundamental and second harmonic spectrum is shown in Fig. 5 for a pump laser diode current of $I_{\mathrm{D}} = 1.6\,\mathrm{A}$. The optical power of the second harmonic generated (SHG) light has been measured to be 16 mW. A location of a focus inside the crystal would increase the doubling efficiency significantly. The optical-to-optical conversion efficiency was measured to be 2.3 %.

5. Conclusion

An InAlGaAs semiconductor disk laser has been grown, processed and characterized which shows a high beam quality ($M^2 < 1.1$) and high power near-infrared ($\lambda \sim 972\,\mathrm{nm}$) laser output. The collimated laser beam has been coupled into a 5.9 μm-core 980 nm single-mode fiber with a coupling efficiency of $> 70\,\%$.

Additionally, the 980 nm semiconductor disk laser radiation has been frequency doubled to produce 16 mW coherent blue-green light (490 nm) by intra-cavity second harmonic generation (SHG) using Lithium Triborate (LBO).

References

[1] M. Kuznetsov, F. Hakimi, R. Sprague, and A. Mooradian, "Design and Characteristics of High-Power (> 0.5-W CW) Diode-Pumped Vertical-External-Cavity Surface-Emitting Semiconductor Lasers with Circular TEM_{00} Beams," *IEEE J. Selected Topics Quantum Electron.*, vol. 5, no. 3, pp. 561–573, 1999.

[2] H. J. Unold, S. W. Z. Mahmoud, R. Jäger, M. Kicherer, M. C. Riedl, and K. J. Ebeling, "Improving Single-Mode VCSEL Performance by Introducing a Long Monolithic Cavity," *IEEE Photon. Technol. Lett.*, vol. 12, no. 8, pp. 939–941, 2000.

[3] A. J. Fischer, K. D. Choquette, W. W. Chow, A. A. Allermann, and K. M. Geib, "5.2 mW Single-Mode Power from a Coupled-Resonator Vertical-Cavity Laser," *IEEE LEOS 2000 Lasers and Electro-Optics Society, 13th Annual Meeting, Rio Grande, Puerto Rico, ThN2*, pp. 802–803, 2000.

[4] M. Miller, M. Grabherr, R. King, R. Jäger, R. Michalzik, and K. J. Ebeling, "Improved Output Performance of High-Power VCSELs," *IEEE J. Selected Topics Quantum Electron.*, vol. 7, no. 2, pp. 210–216, 2001.

[5] M. Sagawa, T. Toyonaka, K. Hiramoto, K. Shinoda, and K. Uomi, "High-Power Highly-Reliable Operation of 0.98-μm InGaAs-InGaP Strain-Compensated Single-Quantum-Well Lasers with Tensile-Strained InGaAsP Barriers," *IEEE J. Selected Topics Quantum Electron.*, vol. 1, no. 2, pp. 189–195, 1995.

[6] M. Y. A. Raya, S. R. J. Brueck, M. Osinski, C. F. Schaus, J. G. McInerney, T. M. Brennan, and B. E. Hammons, "Resonant Periodic Gain Surface-Emitting Semiconductor Lasers," *IEEE J. Quantum Electron.*, vol. 25, no. 6, pp. 1500–1512, 1989.

[7] S. W. Corzine, R. S. Geels, J. W. Scott, R.-H. Yan, and L. A. Coldren, "Design of Fabry-Perot Surface-Emitting Lasers with a Periodic Gain Structure," *IEEE J. Quantum Electron.*, vol. 25, no. 6, pp. 1513–1524, 1989.

Determination of Dislocation Density in epitaxial grown GaN

Frank S. Habel

Up to now the question how far the high dislocation density in Gallium Nitride epitaxial layers affects the device efficiency and lifetime is not completely answered. The investigation of these topics as well as the further improvement of the crystalline quality requires a fast and reliable method to determine the dislocation density. Therefore, a HCl vapor phase etching process was established that provides access not only to the overall dislocation density but also to the densities of several dislocation types.

1. Introduction

Due to the lack of Gallium Nitride (GaN) substrates, the growth of GaN has to be carried out heteroepitaxially. The most common substrates are sapphire (Al_2O_3) and silicon carbide (SiC) with a lattice mismatch of 13.8 % and 3.4 % respectively. This huge lattice mismatch leads to the formation of threading dislocations with a density in the order of $10^8 - 10^{10}$ cm^{-2}. It is well known that such dislocations act as nonradiative recombination centers in other semiconductor materials. On the other hand these recombination centers cannot be very effective in GaN for the realization of optoelectronic devices is possible in spite of these high dislocation densities [1, 2]. Another important topic is the effect of the dislocation density on device lifetime, although there are publications which conclude that the dislocation mobility in GaN-related materials is too low to contribute to the degradation of devices [3].

Several methods to analyze the dislocation density are known. Observation by transmission electron microscopy (TEM) is regarded as the most reliable but also very time-intensive technique. Other possibilities are wet chemical etching in molten potassium hydroxide (KOH) or in heated phosphoric acid (H_3PO_4). Since etching occurs where dislocations penetrate the surface, pits are formed which make the dislocations visible. Another method is a HCl vapor phase etching process, that is described in the next section.

2. HCl Etching Process

The HCl vapor phase etching process was established in an GaN hydride vapor phase epitaxy system (HVPE). A temperature of 600°C has been chosen. The HCl gas was

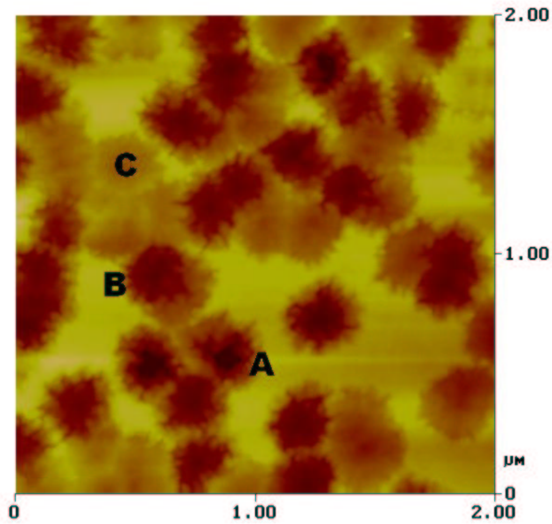

(a)
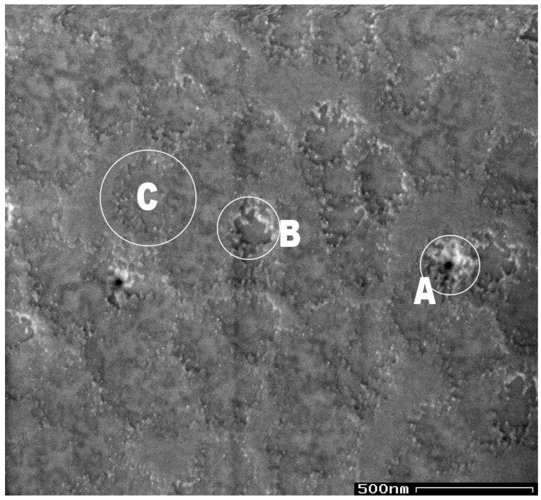

(b)

Fig. 1. AFM image (a) and SEM image (b) showing three types of etch pits

diluted by nitrogen (N_2). The reactor pressure was 950 mbar and the etching time was varied between 15 minutes and 30 minutes.

According to [4] a possible chemical reaction for the etching process is the formation of GaCl, N_2 and H_2 as shown in the following equation:

$$2\mathrm{GaN(s)} + 2\mathrm{HCl(g)} \rightarrow 2\mathrm{GaCl(g)} + \mathrm{N_2(g)} + \mathrm{H_2(g)} \tag{1}$$

The etching time as well as the HCl partial pressure can be used to control the size of the etch pits. Smaller pits are preferred for accurate determination of the overall dislocation density. With increasing pit size different types of pits can be distinguished, but for high pit densities the counting of the pits gets more difficult because the pits start to merge. A further increase of the temperature or a decrease of the reactor pressure lead to a serious roughening of the sample surface.

3. Evaluation

The pits can be observed by atomic force microscopy (AFM) (figure 1a) as well as by scanning electron microscopy (SEM) (figure 1b). For the determination of the overall pit density generally a 10 μm x 10 μm image has been taken by AFM in tapping mode to obtain a statistically significant number of pits. In table 2 some typical values for the etch pit densities (EPD) of samples grown in our metal-organic vapor phase epitaxy system (MOVPE) are shown. The number of threading dislocations for a multi quantum well (MQW) structure is higher than for a intentionally undoped GaN layer. The Mg-doped p-GaN layer has even more dislocations.

In order to distinguish different dislocation types, larger pits had to be etched. An etching time of 30 minutes and a high HCl partial pressure have been necessary. In figure 2 the

sample	EPD [cm^{-2}]
GaN, undoped	8.9×10^8
GaN, MQW-structure	2.2×10^9
GaN, p-doped	2.9×10^9

Tab. 2. First EPD-values for samples grown by MOVPE

number of pits versus the pit depth is plotted. It shows that the depth-levels of the pits are not randomly distributed. Three pit types with certain depth-levels can be observed.

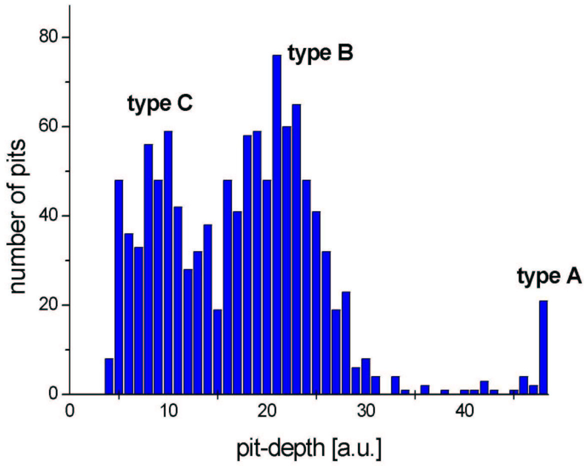

Fig. 2. Distribution of the pits over depth-levels

Type A dislocations lead to pits about 70 nm deep, type B pits have a depth of about 20 nm, whereas type C pits are relatively flat with about 10 nm in depth. These types are marked in figure 1. The corresponding cross-sections are shown in figure 3. For none of these types a hexagonal shape could be observed. The typical values for the densities of the pit types mentioned above are listed in table 3. First comparisons of these values with those obtained from the same wafer by TEM and by H_3PO_4-etching showed good agreement.

Furthermore the pit types could be assigned to certain dislocation types. According to

Pit	depth [nm]	EPD [cm^{-2}]
type A	70	3.8×10^7
type B	20	5.8×10^8
type C	10	8.2×10^8

Tab. 3. First EPD-values for different pit-types

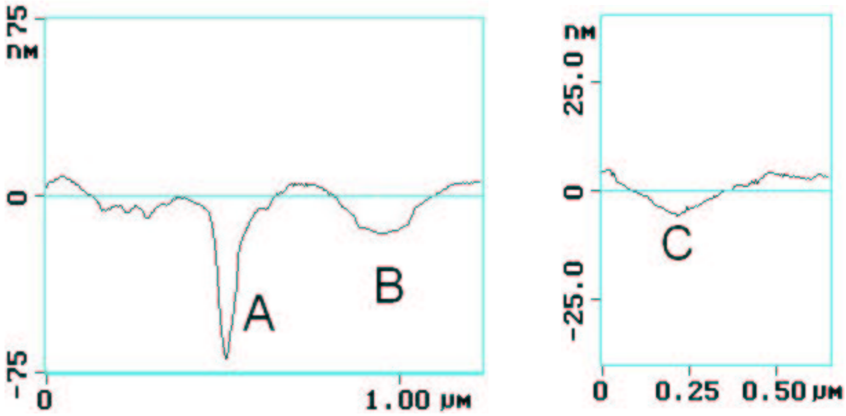

Fig. 3. Cross-sections of etch pits type A, B and C

Hino et al. [4] type A pits correspond to screw dislocations with Burgers vector $\vec{c}$, type C pits to edge dislocations (Burgers vector $\vec{a}$) and type B pits to mixed dislocations (Burgers vector $\vec{a} + \vec{c}$).

4. Conclusion and Summary

A HCl vapor phase etching process has been established to reveal threading dislocations by the formation of etch pits. The etched samples can be analyzed easily by AFM or SEM. The reliability and reproducibility of this technique have been proven by a comparison with other methods like TEM and H_3PO_4-etching. The HCl etching technique is a fast alternative to TEM analysis and has no drawbacks in reliability like some wet-etching methods. Therefore, it is an important instrument to increase the performance of GaN-based devices.

References

[1] E. R. Weber, J. Krüger, and C. Kisielowski, "New Materials: Gallium Nitride," in *Handbook of Semiconductor Technology, Vol. 1, K. A. Jackson and W. Schröter* , pp. 771–808, 1998.

[2] F. A. Ponce, "Structural defects and materials performance of the III-V nitrides," in *Group III nitride semiconductor compounds - physics and applications, B. Gil* , pp. 123–157, 1998.

[3] L. Sigura, "Dislocation motion in GaN light-emitting devices and its effect on device lifetime," J. Appl. Phys. **81** , pp. 1633–1638, 1997.

[4] T. Hino, S. Tomiya, T. Miyajima, K. Yanashima, S. Hashimoto, and M. Ikeda, "Characterization of threading dislocations in GaN epitaxial layers," Appl. Phys. Lett. **76** , pp. 3421–3423, 2000.

Substrates for Wide Bandgap Nitrides

Matthias Seyboth

Different substrates for gallium nitride growth are discussed. The commercially relevant substrates, silicon carbide and sapphire, and the two most promising alternatives, silicon and gallium nitride, are compared in their effects on devices. An estimation on future market success is given.

1. Introduction

Within a decade, gallium nitride (GaN) and its ternary alloys InGaN and AlGaN conquered a substantial share of the compound semiconductor market - so far predominantly in the optoelectronics sector, but recently with an increasing potential in electronics. Considering the strongly lattice mismatched heteroepitaxial growth of the nitrides, yielding dislocation densities 5 – 6 orders of magnitude higher than in other commercial compound semiconductor materials, this is even more amazing. Of late increasing efforts have been undertaken to further improve the material quality of the GaN layers by employment of substrates superior to the industrial quasi standards silicon carbide (SiC) and sapphire (Al_2O_3).

Within this report we focus on four substrate materials: GaN - single crystal substrates together with hydride vapor phase epitaxy (HVPE) grown quasi substrates constitute an approach for the high end device market. They are compared with SiC and sapphire as the established industrial standards and with silicon (Si) as an alternative for electronic applications and for low cost optoelectronics.

In industrial LED production 6H-SiC and sapphire prevailed so far. On both substrates suitable growth techniques have been developed allowing the usage of specific advantages of the materials. Sapphire has a higher availability as well as significantly lower costs. Its lower refractive index and negligible absorption allow better outcoupling efficiency. The compressive strain in epitaxial GaN on sapphire permits thicker layers compared to SiC. The latter, however, is available electrically conductive and thus allows a complete vertical structure, it also reduces electrostatic discharge problems. Thermal conductivity of SiC is higher than of sapphire making an improved thermal management possible.

From point of epitaxial growth, defect free GaN substrates are obviously the ideal choice, omitting threading dislocations, nucleation layers, as well as wafer bending due to different thermal expansion coefficients. Unfortunately, in spite of strong research efforts, e.g. high pressure bulk growth or HVPE and substrate removal, there is not yet a commercialized freestanding 2” GaN substrate. Growth on small, defect reduced substrates, however, showed physical properties setting standards for GaN growth.

In contrast to usual comparisons from epitaxial perspective this report focuses on the impact of substrate material on devices. We end with a forecast considering also economic factors.

2. Processing and Manufacturing

A means of cost reduction in semiconductor technology is usually scaling up wafer size. Here are obvious differences: whereas Si is available from 2” – 12” in excellent quality, sapphire is commercially available up to 4”. Good SiC can be obtained up to 3”. GaN is expected to be available in 2” size from HVPE and just in square centimeter size from bulk crystal growth. But there are also drawbacks for scaling up wafer size for GaN growth: with differences in thermal expansion coefficients wafer bending is an increasing problem for larger wafers. Heat coupling during epitaxy gets difficult but also processing steps like wafer thinning and photolithography are complicated. Additionally, a reduced temperature homogeneity in LED growth, e.g., results in non-uniformity of emission wavelength and thus reduced production yield.

In several process steps mechanical and chemical properties of substrates are important. For substrate thinning Si would be advantageous, the relatively hard and chemically inert substrates SiC, sapphire and GaN need advanced and therefore expensive thinning processes. In general, only Si allows easy substrate structuring with all manufacturing and etching tools known from Si-processing, e.g. for via hole formation for integrated structures. Comparing sapphire and SiC, the latter one is better structurable in sawing processes, with several consequences: thinner saw blades and less material break out enable higher device densities on wafer and thus a better production yield; more advanced processes allow substrate structuring e.g. for LED structures such as Osram Opto Semiconductors (Regensburg, Germany) so called ”ATON” technology [1]. Difficult for processes on (111) Si might be the nonperpendicular cleavage planes. For cleaving of laser facets SiC- and GaN-substrates are preferable. They offer a close enough matching of crystal directions to produce excellent mirrors [2], though cleaving of lasers on a-plane sapphire has been demonstrated.

For device design and performance the electrical conductivity of the substrate can be decisive. For homogeneous current injection in LEDs and lasers a conductive substrate is advantageous. It allows for a vertical structure and thus also can increase the number of devices per wafer. Conducting substrates additionally reduce problems with electrostatic discharge (ESD). Only on SiC substrates standard LEDs in ESD class II (stable up to 1000 V) are manufactured, on isolating sapphire class I (up to 400 V) is possible. SiC, Si and GaN allow such vertical structures. On the other hand electronic devices for high frequency power applications need insulating substrates, sapphire is an insulator and SiC achieves resistivity values of $\rho > 10^5\,\Omega$cm, values for Si reach only $\rho > 10^4\,\Omega$cm. However, resistivity in both semiconductors decreases drastically at elevated temperatures.

A unique feature of growth on Si substrates is of course the direct integration of GaN-technology - allowing optoelectronics or high power high frequency electronics - with silicon technology. Even though it is not clear to what extend the epitaxial and processing steps for the two material systems can be adapted, this integration opens interesting perspectives e.g for micromechanical or sensor applications.

3. Thermal Conductivity

A common problem of semiconductor devices is heating due to power loss. In GaN-based light emitters especially the p-contact and p-region but also nonradiative recombination act as heat sources. We determined the local temperature distribution of LEDs on sapphire substrate by spatially resolved Raman measurements [4] and also by fits to micro-electroluminescence spectra [3]. The measurements were performed on diced LED chips. In figure 1 the determined data are compared with the temperature simulations performed with ANSYS. Based on the good agreement we simulated temperature distributions for

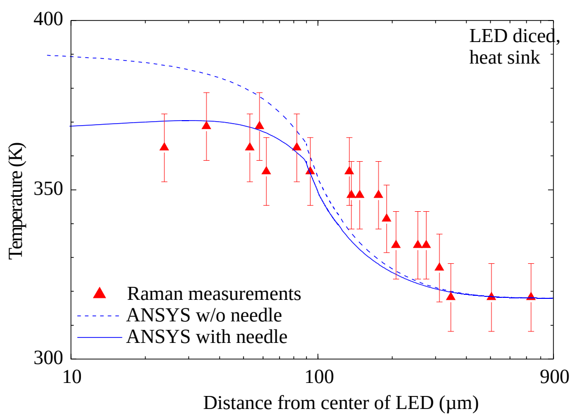

Fig. 1. Comparison of a profile of the ANSYS simulation with data from Raman measurements. For a good match the heat drain by the contact needle has to be considered.

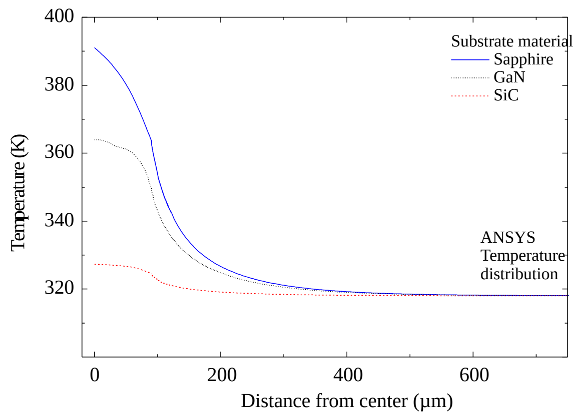

Fig. 2. Temperature profile in dependence of substrate material.

different substrates. In table 4 the heat conductivity for the four discussed substrates is compared. Figure 2 depicts the resulting temperature distribution. The advantage of

	GaN	sapphire	SiC	Si
thermal conductivity [W/cmK]	1.3	0.46	4.9	1.5

Tab. 4. thermal conductivity at 300 K

SiC is obvious; Si and GaN have about the same characteristics; and the poor temperature conductivity of sapphire results in a strongly elevated device temperature. A similar behavior can also be expected for electronic devices, especially for power devices a good thermal conductivity is necessary.

An alternative method for improving thermal management of devices is reducing distance to a heat sink. NEC employed this process step to improve the device performance of FETs grown on sapphire [5].

However, device temperature is not only a function of substrate, whether material or thickness, the complete device including bondwires, housing, etc. determines the thermal management. In standard 3 or 5 mm LEDs the package can be a limiting element for heat removal. For such devices the complete design has to be adapted to take the most advantage of a better thermal conductivity of a substrate. Since in an LED the heat is confined beneath the p-contact it should be ideally removed from the LED surface and not through the substrate. This is the case in most device structures, thus flip chip technologies are of interest, e.g. junction side down mounting of laser diodes and for high brightness LEDs [6]. With flip chip mounted devices, substrate removal technologies get also back into focus. Si of course allows the easiest method of etching; and for sapphire substrates laser ablation techniques have been demonstrated.

4. Optical Properties

For light emitting devices the substrate to some extend acts more as a part of the device than as a mere carrier. Within the layer structure of a laser diode the refractive index of the substrate and the differences to the epitaxial layers can lead to substrate modes. In LED structures the combination of absorption and refractive index of the substrate have significant influence on extraction efficiency and thus device performance [7].

In Figure 3 a point source within an epitaxial layer structure is displayed. The cones sketch the part of light that is not reflected at refractive index steps from semiconductor to surface or substrate. For the different cones there are several approaches to enhance outcoupling. The top cone for example is usually hindered by the top metal contact: a semitransparent contact improves efficiency. The sidewise cones can be influenced by chip geometry. The light in the bottom cone has to pass the substrate. Absorption and thickness determine the amount of light to reach the bottom end. Refractive indices determine the angle of the cone.

Graph 4 depicts calculations of outcoupling efficiency dependent on the used substrate. The simulation is based on a LED emitting at 410 nm so there is already significant absorption for GaN and 6H-SiC. The utilized values for refractive index and absorption are stated in table 5. A three layer structure serves as simplified model for the LED. A $50\,\mu$m$\times$$50\,\mu$m gold p-contact on a mesa of 400 nm thick p-GaN on $2\,\mu$m n-GaN with a size of $150\,\mu$m$\times$$150\,\mu$m. The substrate size is $300\,\mu$m$\times$$300\,\mu$m with a thickness of $100\,\mu$m. The resulting differences are obvious. On the silicon substrate a large part of the generated light is absorbed in the substrate. Here a bragg mirror might be a helpful. For the other substrate materials the refractive index is the dominating factor, reducing

	GaN	sapphire	SiC	Si
refractive index	2.5	1.7	2.8	5.2
absorption [cm^{-1}]	100	10	40	8×10^4

Tab. 5. refractive indices and absorption coefficients at 410 nm.

the outcouple angle. To overcome this disadvantage of SiC, Osram Optosemiconductors and Cree (Durham, USA) demonstrated an enhanced outcoupling efficiency by substrate structuring. In Osram's "ATON" technology [1] equivalent to Cree Lighting's "ultrabright LEDs" [8] the cubicle substrate shape is combined with a truncated pyramid.

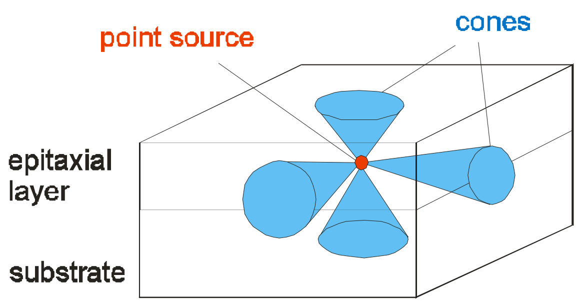

Fig. 3. Outcouple cones of a point source in a LED structure illustrating the part of light coupled out without a reflection.

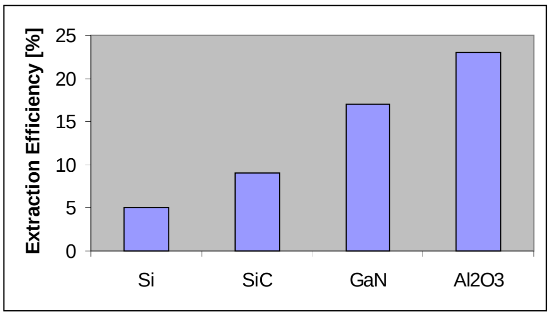

Fig. 4. Calculated extraction efficiency for different substrates.

5. Economical Considerations and Conclusion

It is obvious that physical and technical advantages and disadvantages of different substrate materials combine to a complex picture. Additional economical considerations complicate this picture even more.

From substrate price the situation is simple. A short, in no way representative, survey yielded for 2" substrates a factor between 5 and 10 as increase in price from Si to sapphire and another 5 to 10 between sapphire and SiC. For GaN substrates there is no 2" substrate available. However, processes for sapphire and SiC for LED production show that processing costs and devices per wafer dominate the calculation. The resulting economically important figure is a combination of physical values and *the* economical value: lm/$ – How much do you have to spend to get the desired light.

For gaining share in the LED market, devices on Si first have to show typical 1 mW optical output power at 20 mA at 470 nm emission wavelength and reasonable lifetimes. Only then these devices have a chance to conquer parts of the low cost market. To a lesser extend by making use of the inexpensive substrate than by reduced processing costs. Another possibility for GaN on Si is the forming electronics market, here Si is not a newcomer but is directly competing with the alternatives.

Chances for GaN substrates lie in reduced defect densities. Devices like lasers could profit in lifetime and far field. Here these substrates compete in price with an also costly defect reducing ELO processes. However, problematic is the market for these laser diodes: modules for DVD-players are certainly no high price products. With existing production techniques and falling prices, GaN substrates in a far future might partly compete with SiC. For scientific purposes even commercially not applicable substrates are of high interest. Of course invention and realization of less expensive GaN substrates would make large parts of this discussion obsolete.

Concluding the discussion, we do not expect rapid changes (i.e. in the next 2–3 years) in the established LED market. With all existing production lines and epitaxy facilities sapphire and SiC in 2" size will prevail. Surprises may come from emerging markets for electronic devices or laser diodes.

References

[1] N. Stath, V. Härle, and J. Wagner, "Optoelectronic device substrates," *Materials Science and Engineering B* vol. 80, no. 1–3, pp. 224–231 , 2001.

[2] V. Schwegler, S.S. Schad, M. Scherer, M. Kamp, G. Ulu, M. Emsley, M.S. Ünlü, A. Lell, S. Bader, B. Hahn, H.J. Lugauer, F. Kühn, A. Weimar, and V. Härle, "GaN-based lasers on SiC: influence of mirror reflectivity on L-I characteristics," *Crystal Growth* vol. 230, pp. 512-516, 2001.

[3] V. Schwegler, M. Seyboth, C. Kirchner, M. Scherer, M. Kamp, P. Fischer, J. Christen, and M. Zacharias "Spatially Resolved Electroluminescence of InGaN-MQW-LEDs," *MRS Internet J. Nitride Semicond. Res.* vol. 5S1, W1.2, 2000.

[4] V. Schwegler, M. Seyboth, S. Schad, M. Scherer, C. Kirchner, M. Kamp, U. Stempfle, W. Limmer, and R. Sauer, "Temperature Distribution in InGaN-MQW LEDs Under Operation," *MRS Internet J. Nitride Semicond. Res.* vol. 5S1, W11.18, 2000.

[5] Press Release NEC, December 12th, 2001.

[6] Lumiled, Luxeon Application Notes. AB07 Lumen Maintenance of White Luxeon Light Sources, http://www.luxeon.com/products/products_index.html, 2002.

[7] S.S. Schad, M. Scherer, M. Seyboth, and V. Schwegler, "Extraction Efficiency of GaN-Based LEDs," *Phys. Stat. Sol. a* vol. 188, no. 1, pp. 127–130, 2001.

[8] "Cree Doubles Brigthness of Blue and Green LEDs," *Compound Semiconductor* vol. 6, no. 8, p. 11, 2000

Wafer-bonded, Tapered InGaAlP-LEDs with an Emission Wavelength of 650 nm

Marcus Scherer

In this article a new concept for efficient light-emitting diodes is presented. It combines the idea of outcoupling taper with a soldering technique. First devices show external quantum efficiencies of 11% and optical output power of 2 mW. Additionally the process flow for these devices is given in detail.

1. Introduction

One of the cardinal problems limiting the performance of light-emitting diodes (LEDs) is their low external quantum efficiency due to total internal reflection of light in the semiconductor material. Several approaches have already been published to counteract this problem including resonant cavity LEDs with their modified internal direction of spontaneous emission [1], surface textured devices with a back side mirror where photons repeatedly try to escape [2], or the use of transparent substrates [3]. We presented a new method of efficient light outcoupling from thin-film LEDs by introducing lateral tapers [4, 5, 6]. For this concept, light generation is limited to a small area in the very center of a circularly symmetric structure. After propagating between two highly reflecting mirrors, light is outcoupled in a flat tapered mesa region. Since this idea is not limited to a certain material system, it has been transferred to the InAlGaP system after proving its suitability for As-based devices emitting at 980 nm [6].

For free standing devices we have evolved a process route which has the substrate removement as final step. Nevertheless, handling a thin semiconductor film is difficult. Here, a new type which combines the outcoupling taper with a soldering technique [7] is presented. This promises a more feasible fabrication method.

2. Device Processing

The epitaxial structure for these LEDs is grown by metal-organic vapor phase epitaxy. It consists of an AlAs etch stop layer followed by several μm n-doped $Al_{0.5}Ga_{0.5}As$. The active region made up of AlGaInP multiple-quantum wells is embedded into AlInP cladding layers. Finally a p-type $Al_{0.5}Ga_{0.5}As$ contact layer is grown on top of the structure.

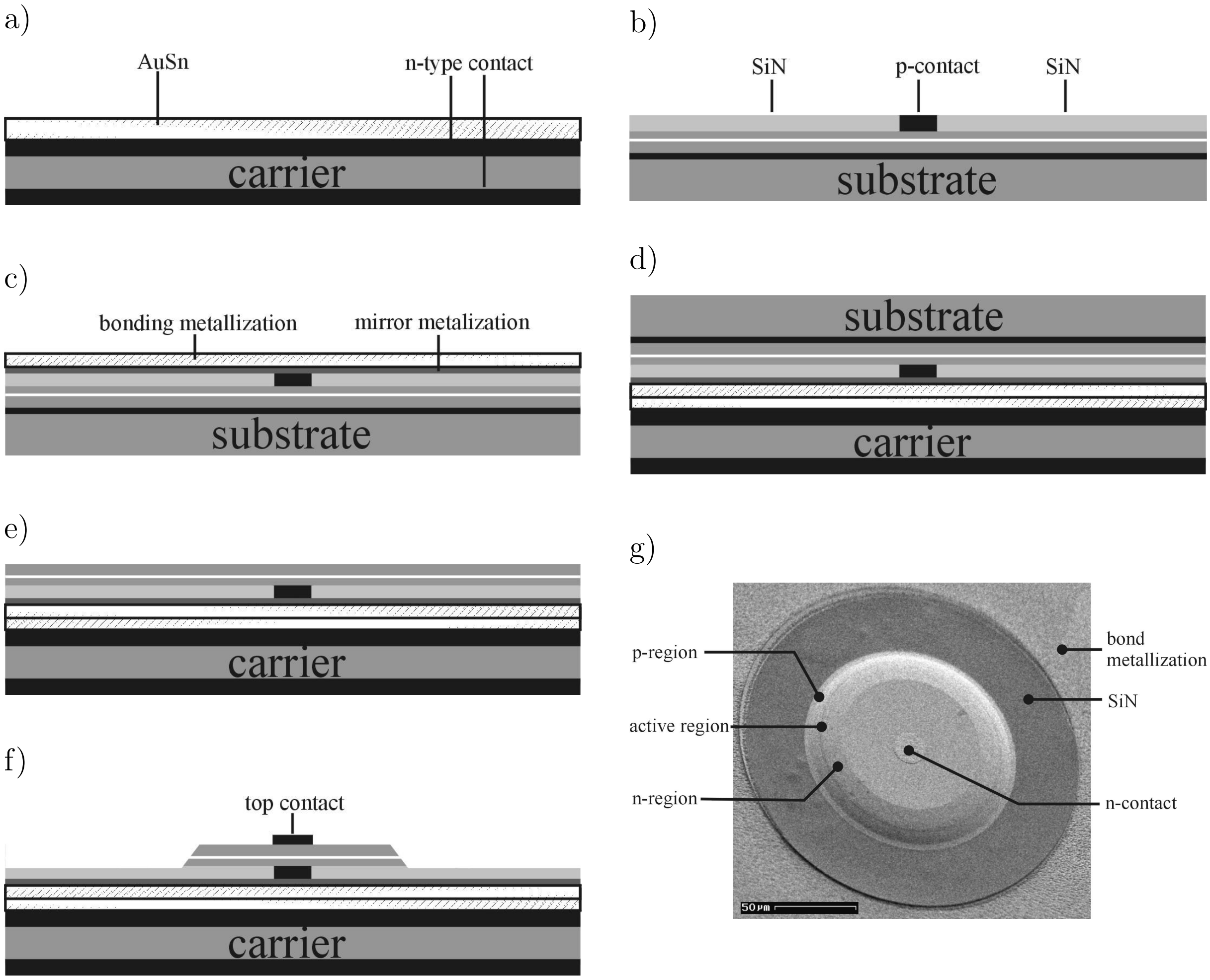

Fig. 1. Processing steps: A carrier is prepared with electric contacts and a bond metallization (a). P-contacts are deposited onto the epitaxial structure and surrounded by SiN (b). After mirror and Au bonding layer deposition (c), the LED structure is flip-chip bonded onto the carrier (d) and substrate and etch stop layer are removed (e). After forming the taper, a top contact is evaporated onto the LED (f). (g) shows a SEM image of a ready processed waferbonded LED.

The process flow for waferbonded LEDs is given in Fig. 1. At the outset, a GaAs carrier is covered with AuGe on both sides, followed by thick electro-plated AuSn on one side. The latter layer is serving as bond metallization in the following process.

On top of the epitaxial layers, a 20 μm in diameter p-contact is embedded in SiN which passivates the surrounding area and enhances the reflectivity of the subsequently evaporated metal mirror. The metal mirror is finally enhanced by a thick bonding layer (Fig. 1c). The LED structure is then up-side-down bonded onto the carrier (Fig. 1d) using the hypereutectic soldering technique [7]. After removing the GaAs substrate in a citric acid solution [8] and the AlAs etch stop layer, a 300–400 nm high socket is wetchemically structured. After depositing resist on the pedestal, it reflows in solvent atmosphere

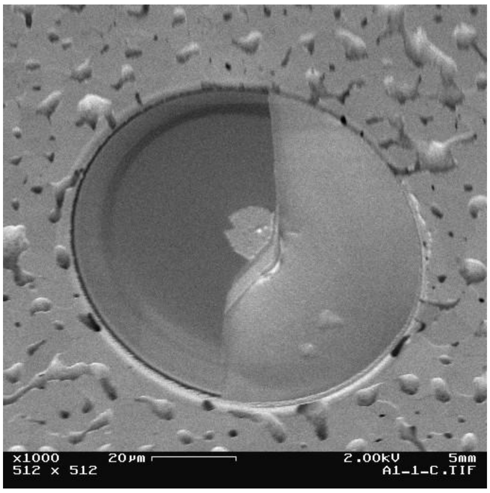

Fig. 2. Mechanically damaged device after being contacted by needles.

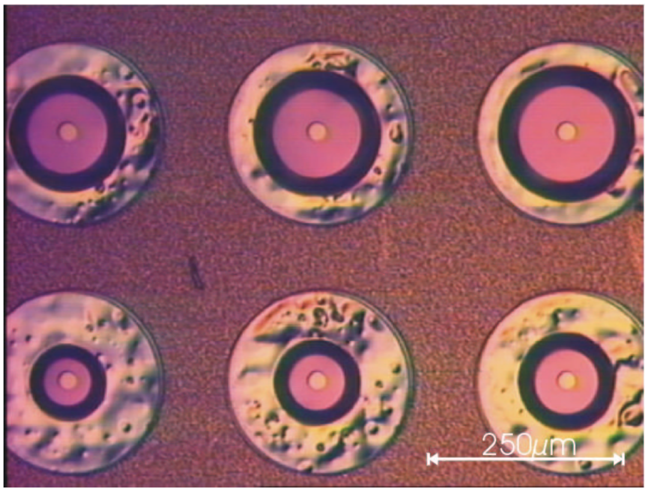

Fig. 3. Blistered backside mirror after contact annealing.

becoming lens-like. This structure is partly transferred into the semiconductor using ion beam etching. A more detailed description of forming the taper is published by Schmid and colleagues [5]. Finally a Ge/Au/Ni/Au contact with a diameter of 20 μm is evaporated onto the device. Fig. 1g) shows a SEM image of a completely processed waferbonded, tapered LED.

Although first samples could been demonstrated (see Sect. 3.) several technological problems still have to be solved. First the mechanical stability of the devices. Since the thickness of the epitaxial layers is in the range of 5 μm the devices could easily be damaged by any mechanical stress like contacting by needles (Fig. 2) or bonding. Here imbedding the LEDs in polyimide might help. Second, contact annealing has to be adjusted to the layer sequence for the backside mirror. Here a blistered surface (Fig. 3) is detected after thermal treatment at 400°C.

3. Characterization and Discussion

First results are given Fig. 4 illustrating the characteristics of a 120 μm diameter device. The LED shows a maximum optical output of 2 mW at 15 mA. The external quantum efficiency reaches a value of 11% at 3 mA and a just slightly smaller wallplug efficiency (10%) for the unencapsulated device. Comparing these results with bottom emitting devices [9] of the same epitaxial structure, one can see from the reduced turn-on voltage that this devices benefit from a different process flow which does not require contacts on a dry etched semiconductor surface. This reduces internal heating of the device resulting in higher output power and later instating thermal roll-over. Additionally, the maximum external quantum efficiency is shifted to higher currents.

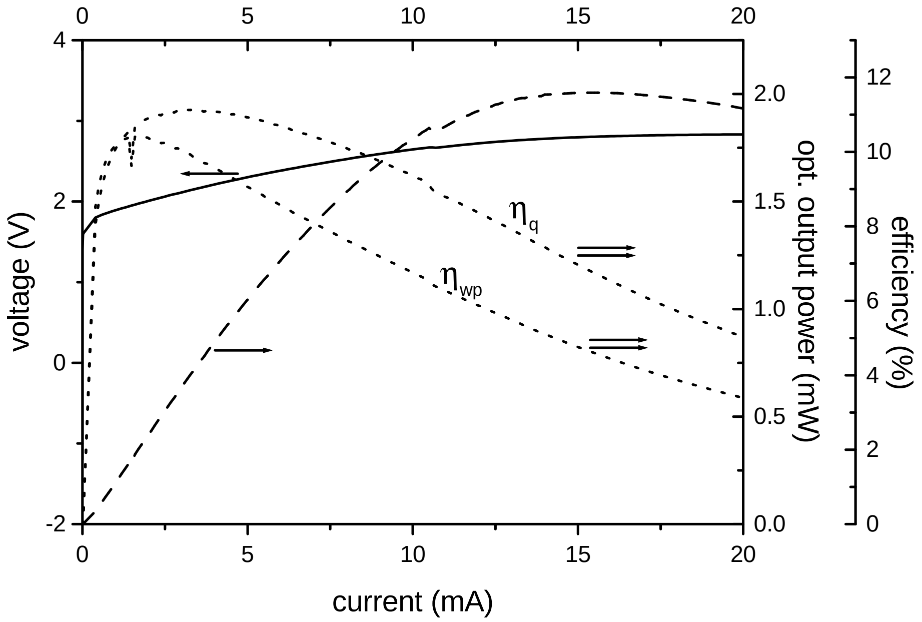

Fig. 4. Optical output power and quantum efficiency of a 120 μm diameter waferbonded device without encapsulation.

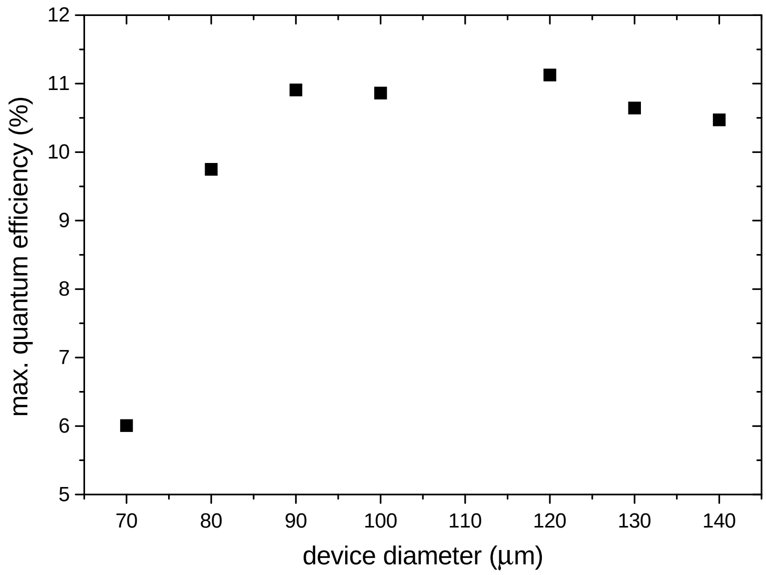

Fig. 5. Maximum external quantum efficiency vs. device diameter.

Nevertheless, these LEDs suffer from low quantum efficiencies (Fig. 5) between 9 and 11% for devices with an overall diameter of more than 80 μm. These values are just slightly lower than those for the bottom emitting devices [9] and comparable taper angles around 10°. The low efficiency for both concepts denotes a general problem for this devices in the red wavelength range. This assumption is supported by measurements indicating an internal efficiency of less than 30% (see article by Sven-Silvius Schad in this issue). To counteract, a redesign of the epitaxial structure including the use of different contact layers like GaP is planned.

4. Conclusion

We have successfully established a process route to fabricated devices that combine the idea of a tapered structure with a soldering technique for improved light outcoupling from semiconductor material. First InGaAlP-LEDs show maximum optical output power of 2 mW at an emission wavelength of 650 nm. External quantum efficiencies of 11% have been determined for these samples.

References

[1] H. DeNeve, J. Blondelle, P. van Daele, P. Demeester, and R. Baets, "Recycling of guided mode light emission in planar microcavity light emitting diodes," *Appl. Phys. Lett.* vol. 70, pp. 799–801, 1997.

[2] R. Windisch, M. Kuijk, B. Dutta, G.H. Döhler, G. Borghs, and P. Heremans, "High-Efficiency Surface-Textured LEDs," *Compound Semiconductors.* vol. 6, no. 4, pp. 55–58, 2000.

[3] M.R. Krames, M. Ochiai-Holcomb, G.E. Höfler, C. Carter-Coman, E.I. Chen, I.-H. Tan, P. Grillot, N.F. Gardner, H.C. Chui, J.-W. Huang, S.A. Stockman, F.A. Kish, and M.G. Craford, "High-power truncated-inverted-pyramid $(Al_xGa_{1-x})_{0.5}In_{0.5}P/GaP$ light-emitting diodes exhibiting >50% external quantum efficiency," *Appl. Phys. Lett.* vol. 75, no. 16, pp. 2365–2367, 1999.

[4] W. Schmid, F. Eberhard, M. Schauler, M. Grabherr, R. King, M. Miller, E. Deichsel, G. Stareev, U. Martin, R. Jäger, J. Joos, R. Michalzik, and K.J. Ebeling, "Infrared Light-Emitting Diodes with Lateral Outcoupling Taper for High Extraction Efficiency," *Proc. SPIE* vol. 3621, pp. 198–205, 1999.

[5] W. Schmid, F. Eberhard, R. Jäger, R. King, M. Miller, J. Joos, and K.J. Ebeling, "45% quantum-efficiency light-emitting diodes with radial outcoupling taper," *Proc. SPIE* vol. 3938, pp. 90–97, 2000.

[6] W. Schmid, M. Scherer, R. Jäger, P. Stauss, K. Streubel, and K.J. Ebeling, "Efficient Light-Emitting Diodes with Radial Outcoupling Taper at 980 and 630 nm Emission Wavelength," *Proc. SPIE* vol. 4278, pp. 109–118, 2001.

[7] S. Illek, U. Jacob, A. Plößl, P. Stauß, K. Streubel, W. Wegleiter, and R. Wirth, "Micro-Reflector Light-Emitting Diodes with Buried Mirror," *Electrochemical Society Proc.* vol. 2001-27, The Electrochemical Society, 2001.

[8] M. Köhler, "Etching in Microsystem Technology," Wiley-VCH, WeinheimNew York, 1999.

[9] M. Scherer, B. Neubert, S.S. Schad, W. Schmid, C. Karnutsch, W. Wegleiter, A. Plössl, and K.P. Streubel, "Efficient InAlGaP Light-Emitting Diodes using Radial Outcoupling Taper," *Proc. SPIE* vol. 4641, in press, 2002.

Extraction Efficiencies of Tapered AlInGaP Light Emitting Diodes Emitting at 650 nm

Sven-Silvius Schad

In this work, a simulation model for the tapered LED is presented by using ray tracing techniques. It is shown that the taper angle influences the extraction efficiency significantly. Based on these simulation results, a small taper angle and a low absorption coefficient are desired. Furthermore, the absorption coefficient is determined using the transmission and the photothermal deflection spectroscopy method. A comparatively large value of $\hat{\alpha} = 50\ \mathrm{cm}^{-1}$ is obtained. By processing a series of samples with varying taper angle, a comparison has been carried out and we get a fair agreement of the predicted and measured values of the efficiencies revealing a small internal efficiency of 28%.

1. Introduction

High brightness light emitting diodes (LEDs) have proven their suitability for a variety of applications such as large area outdoor displays or automotive rear lights. High output power, long lifetime, high reliability and pure saturated colors are advantages which encourage the development of solid state lighting. However, a common problem of light emitting diodes is the presence of total internal reflections and internal absorption losses. A short propagation distance, low absorption coefficients and the avoidance of total internal reflection are therefore demands for novel chip designs. Various approaches have already been presented to realize these requirements such as the truncated inverted pyramid (TIP), the textured surface [1, 2], the resonant cavity LED [3, 4] and the radial outcoupling taper [5, 6, 7]. In this work, we investigate tapered InGaAlP devices operating at 650 nm. This concept is based on light generation in the central area of a circularly symmetric structure. After light propagation between a semiconductor surface and a gold mirror, the extraction of photons takes place in a tapered mesa region.

The basic equation for the external efficiency assuming no current leakages over the heterobarriers exist is

$$\eta_{\mathrm{ext}} = \eta_{\mathrm{int}}\eta_{\mathrm{extract}} \tag{1}$$

where η_{ext} is the external quantum efficiency, η_{int} the internal quantum efficiency and η_{extract} the extraction efficiency. Whereas the internal efficiency depends on the fraction of the radiative and total recombination rate, the extraction efficiency is affected mainly by the chip geometry and absorption. The determination of the extraction efficiency is necessary in order to optimize the processing of such devices. By using ray tracing simulations we will show that both, the extraction and the internal efficiency can be estimated.

Fig. 1. Schematic model of the tapered LED.

2. Simulation of the Extraction Efficiency

We present here only a simplified structure used as simulation model, a description of the processing and the structure of the tapered LED has already been published [5, 6, 7]. We assume a homogeneous semiconductor taper with an average absorption coefficient and refractive index $\bar{n} = 3.5$. Fig. 1 depicts the geometry. The semiconductor taper is 70 μm in diameter with a height of 2.4 μm. The structure is covered by polyimide (1 μm thick, $\bar{n} = 1.7$) and a gold mirror (complex refractive index $\bar{\eta} = 0.166{+}3.15i$ at 650 nm [8]). The p-type contact is 20 μm in diameter. The active region is modelled by a circular array of point sources with isotropic emission. Fig. 2 shows the extraction efficiency versus taper angle τ for different absorption coefficients in the range of 1 cm^{-1} to 50 cm^{-1}. The oscillations for smaller absorption values can be explained by geometrical resonance. This occurs due to the fact that rays are modelled without spatial extend perpendicular to the propagation direction and that the angular transformation of the tapered region cannot reduce the angle of incidence effectively. For these minima a large fraction of the traced rays propagate on closed loops. However, since scattering and refraction is present, we do not expect such behavior in real devices. Based on these calculations, it is evident that

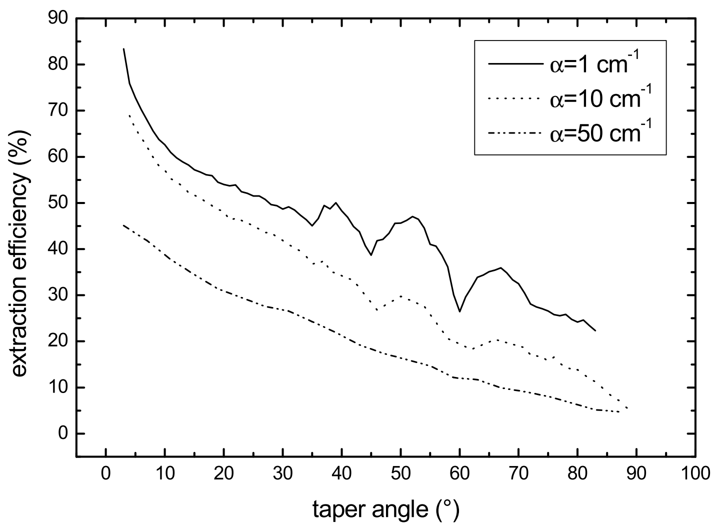

Fig. 2. Simulated external quantum efficiency vs. taper angle.

the taper angle should be as small as possible. Furthermore, the absorption coefficient has a major influence on the absolute results but calculated curves for different absorption coefficients show a similar shape. Below 10° the slope is affected by the absorption mainly due to the increasing volume of the semiconductor taper, since for the simulation the upper diameter is assumed constant. The simulation results denote the importance of knowing the absorption coefficient in the LED structure. Thus, the average absorption for the devices is investigated.

3. Absorption Coefficient

The measurement of optical transmission [9, 10] and reflection as a function of wavelength is a widely used method to determine the absorption around the fundamental band edge of the semiconductor. However, the evaluation for complex structures such as LEDs is difficult. Multiple reflections at each boundary result in complicated analytical terms for the transmission T below the band edge where all interference effects have to be taken into account. On the other hand, absorption far below the band edge is low, so transmission is not noticeably reduced by typical thin film semiconductor thicknesses in the range of 1–4 μm. Within the band, absorption is strong, so, depending on the thickness, all light is absorbed and the evaluated absorption coefficient remains constant. However, there is a small gap in between, where the absorption coefficient is obtained. The absorption coefficient for a two layer system is expressed as [9]

$$\alpha = -1/d \ln \left\{ \left(A + \left(A + 2BT\left(1 - R_2R_3\right)\right)^{1/2} \right) / B \right\} \quad , \tag{2}$$

where

$$\begin{aligned} A &= -(1-R_1)(1-R_2)(1-R_3) \quad (3) \\ \text{and} \quad B &= 2T(R_1R_2 + R_1R_3 - 2R_1R_2R_3) \quad . \quad (4) \end{aligned}$$

Here R_l (l = 1..3) are the intensity reflection coefficients at the three interfaces and d the total thickness. For a large $\alpha \cdot d$ product Eqn. 2 can be simplified to

$$T \approx (1-R)^2 \exp\left(-\hat{\alpha} d\right) \quad , \tag{5}$$

which is indeed a reduction to a one layer system and thus only an average absorption coefficient $\hat{\alpha}$ is obtained. To extend the spectral range of measured absorption values we have employed photothermal deflection spectroscopy (PDS) [11, 12]. For this measurement, the sample is placed in a liquid with a high temperature coefficient of its refractive index. Absorption of a monochromatic pump light causes heating of the sample and thus heating of the surrounding liquid. In consequence, the refractive index of the liquid is changed and a probe laser beam is deflected. The PDS method has the advantage of a wide sensitivity range [12], but only relative measurements can be made. To overcome this, we fit the relative PDS values to the absolute absorption coefficients of the transmission experiment. Fig. 3 illustrates the absorption coefficient for a typical sample.

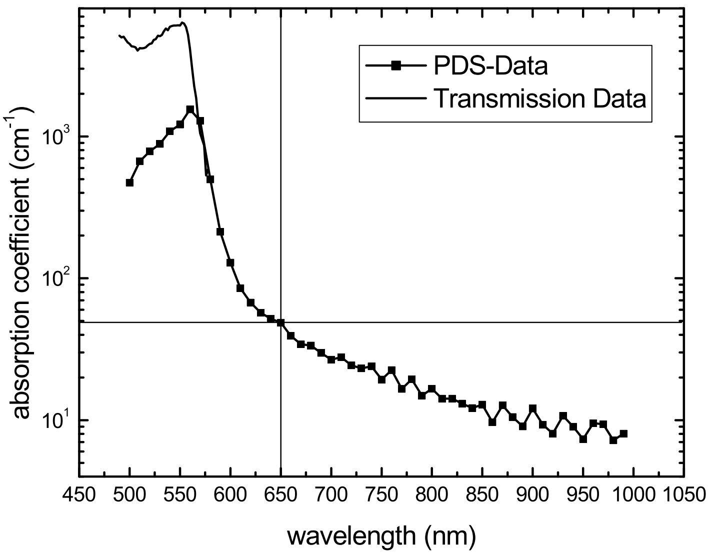

Fig. 3. Absorption coefficient of an investigated sample determined by transmission and photothermal deflection spectroscopy.

Using the transmission and reflection spectra, the absorption coefficient can be calculated precisely in the region of 550–578 nm. Within the band, transmission decreases to zero and the absorption coefficient is not accurate. We estimate the error in $\hat{\alpha}$ to be 45 cm^{-1}, assuming an accuracy of both, transmission and reflection measurement of 1% and taking into account that the two spectra are measured successively. The absorption coefficient derived from the PDS data is adapted in the overlap region. The large deflection causes the probe beam to move out of the detector area. This explains the decay of the PDS signal to shorter wavelengths. For the emission wavelength of 650 nm an absorption coefficient of 50 cm^{-1} is determined and used for a further simulation (Fig. 2).

4. Variation of the Taper Angle

In order to check the validity of the simulation results, a series of samples with varying taper angle in the range of 8 to 53° had been processed by changing the parameters of the etching system. The samples were measured using a profilometer and the taper angles were calculated from these data. Fig. 4 shows measured external quantum and calculated extraction efficiencies. Due to the unknown internal efficiency, only the relative slopes can be compared. Assuming an absorption of $\hat{\alpha} = 50$ cm^{-1} and an internal efficiency of 28%, a fair agreement of the relative linear regression with the simulation is attained. It should be emphasized that the above model does not take into account the low reflectivity of the n-side contact. Therefore, the calculated efficiencies are too high leading to an underestimation of the internal efficiency. The high forward voltage observed for these free-standing devices causes thermal power losses which reduce the internal efficiency. This is probably the main reason for the data scattering. Additionally, the taper angle has an uncertainty, since the values are calculated from a height profile measurement.

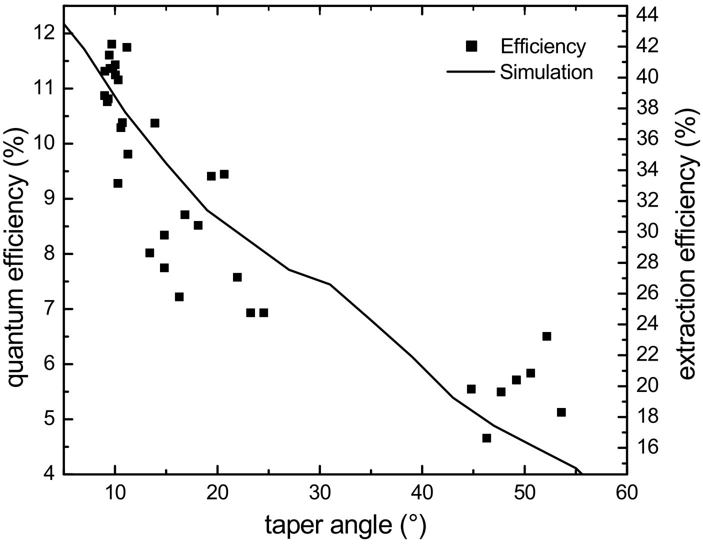

Fig. 4. External quantum efficiency vs. taper angle. Adjusting the calculated extraction efficiency leads to an internal efficiency of 28%.

Depending on the achieved cross section, the real angles are assumed to be slightly larger than the measured ones.

5. Conclusion

In this work, we presented a simulation model which can be used to calculate extraction efficiencies of tapered LED devices. Thereby, the taper angle and the average absorption have been the most important parameters. A determination of the absorption coefficient has been carried out using both, the transmission and photothermal deflection spectroscopy method. A comparatively large value of $\hat{\alpha} = 50\ \mathrm{cm}^{-1}$ has been determined and used for further calculations of extraction efficiency. Samples with varying taper angles have been fabricated and a comparison between simulation and devices showed a fair agreement disclosing a small internal efficiency of 28%.

References

[1] I. Schnitzer, C. Caneau, T. J. Gmitter, A. Scherer, and E. Yablonovitch, "30 % external quantum efficiency from surface textured, thin-film light-emitting diodes," *Appl. Phys. Lett.*, vol. 63, pp. 2174–2176, 1993.

[2] R. Windisch, M. Kuijk, B. Dutta, G. H. Döhler, G. Borghs, and P. Heremans, "High-efficiency surface-textured LEDs," *Compound Semiconductors*, vol. 6, no. 4, pp. 55–58, May 2000.

[3] E. F. Schubert, N. E. J. Hunt, M. Micovic, R. J. Malik, D. L. Sivco, A. Y. Cho, and G. J. Zydzik, "Highly efficient light-emitting diodes with microcavities," *Science*, vol. 265, pp. 943–945, 1994.

[4] H. De Neve, J. Blondelle, P. van Daele, P. Demeester, and R. Baets,"Recycling of guided mode light emission in planar microcavity light emitting diodes," *Appl. Phys. Lett.*, vol. 70, pp. 799–801, 1997.

[5] W. Schmid, F. Eberhard, M. Schauler, M. Grabherr, R. King, M. Miller, E. Deichsel, G. Stareev, U. Martin, R. Jäger, J. Joos, R. Michalzik, and K.J. Ebeling, "Infrared light-emitting diodes with lateral outcoupling taper for high extraction efficiency," *Light-Emitting Diodes: Research, Manufacturing, and Applications III*, Proc. SPIE vol. 3621, pp. 198–205, 1999.

[6] W. Schmid, F. Eberhard, R. Jäger, R. King, M. Miller, J. Joos, and K.J. Ebeling, "45 % quantum-efficiency light-emitting diodes with radial outcoupling taper," *Light-Emitting Diodes: Research, Manufacturing, and Applications IV*, Proc. SPIE vol. 3938, pp. 90–97, 2000.

[7] W. Schmid, M. Scherer, R. Jäger, P. Stauss, K. Streubel, and K.J. Ebeling,"Efficient light-emitting diodes with radial outcoupling taper at 980 and 630 nm emission wavelength," *Light-Emitting Diodes: Research, Manufacturing, and Applications V*, Proc. SPIE vol. 4278, pp. 90–97, SPIE, 2001.

[8] E.D. Palik, "Handbook of Optical Constants of Solid," Academic Press, Orlando, 1985.

[9] E.C. Freeman and W. Paul, "Optical constants of rf sputtered hydrogenated amorphous Si," *Phys. Rev. B*, vol. 203, pp. 716–728, 1979.

[10] R. Swanepoel, "Determination of the thickness and optical constants of amorphous silicon, " *J. Phys. E: Sci. Instrum.*, vol. 16, pp. 1214–1222, 1983.

[11] A.C. Boccara, D. Fournier, W. Jackson, and N.M. Amer. "Sensitive photothermal deflection technique for measuring absorption in optically thin media," *Opt. Lett.*, vol. 5, p. 377, 1980.

[12] O. Ambacher, D. Brunner, R. Dimitrov, M. Stutzmann, A. Sohmer, and F. Scholz, "Absorption of InGaN single quantum wells determined by photothermal deflection spectroscopy," *Jpn. J. Appl. Phys.*, vol. 37, pp. 745–752, 1998.

Tunable GaN-Based Laser Diode

Christoph Eichler

We have investigated the wavelength tuning characteristics of a GaN-based cw-laser diode with an emission wavelength of 425 nm. Temperature dependent spectra have been measured and the shift of the longitudinal modes has been determined with a high resolution optical spectrum analyzer. By using the laser diode in a Littrow configuration [1] we achieved a tuning range of $\Delta\lambda = 4.37$ *nm.*

1. Introduction

Gallium-nitride based blue lasers are subject to intensive research because they are the key technology for the next generation of optical data storage [2]. Further areas of application include high resolution laser printers. Tunable blue lasers are interesting for example to analyze chemicals by their characteristic absorption spectrum.

The emission wavelength of lasers can be tuned using different methods. One possibility is to change the operating temperature of the laser diode which results in a shift of the bandgap energy and a modification of the resonator length, thus affecting the emission wavelength. An other way is to apply an external, wavelength selective feedback to force a specific mode.

In this work we first studied the temperature dependence of the emission wavelength and the resonator modes. In addition we operated the laser diode in a setup with wavelength selective feedback and investigated the tuning range and the side mode suppression ratio (SMSR) of this configuration.

2. Temperature Dependent Shift of the Emission Wavelength

In order to determine the effect of the case temperature on the emission wavelength, we measured the spectrum of the laser at various temperatures in the range from 10°C to 30°C. The normalized spectra are shown in figure 1.

The wavelength does not increase linearly with temperature, but shows mode hopping as can be seen in figure 1. This is caused by a shift of the gain curve with regard to the longitudinal modes of the resonator. Over the measured temperature range a shift of the emission maximum of 0.8 nm was observed (0.04 nm per Kelvin). This result is in good

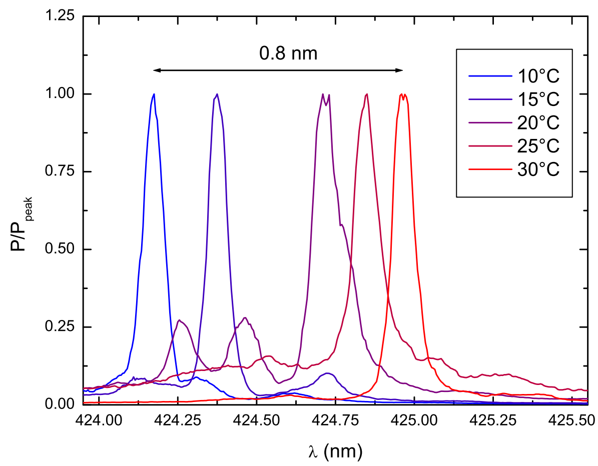

Fig. 1. Spectrum of the Nichia 425 nm laser at temperatures between 10°C and 30°C.

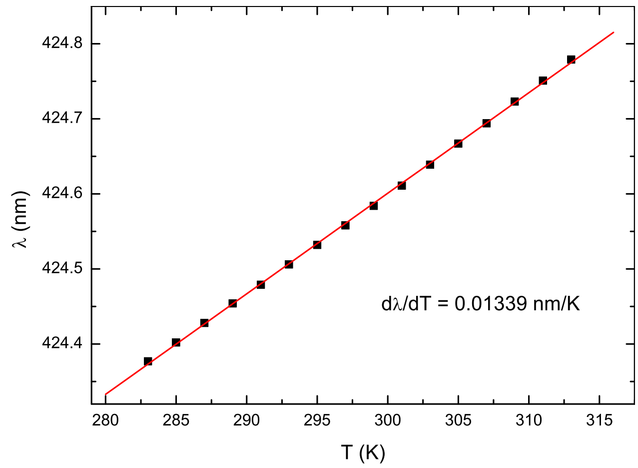

Fig. 2. Wavelength shift of longitudinal modes of a Nichia 425 nm laser with increasing temperature.

agreement with the equation of Varshni for the temperature dependence of the band gap $E_g(T)$:

$$E_g(T) = E_0 - \frac{\alpha T^2}{T + \beta} \quad , \tag{1}$$

where $E_0 = 3.485$ eV, $\alpha = 8.32$ ev/K and $\beta =$ 835.6 K [4, 5]. Using equation 1, an increase of the wavelength of 0.796 nm is calculated for a change in temperature from 10°C to 30°C.

The influence of the temperature on the Fabry-Perot resonator was examined by measuring the spectrum of the laser with a high resolution spectrum analyzer (Advantest Q8347, 0.001 nm resolution) and tracking the wavelength shift of a single longitudinal mode with increasing temperature. Figure 2 shows that the mode shifts almost linearly to longer wavelengths with increasing temperature. A temperature coefficient $\frac{d\lambda}{dT}$ of 0.01339 nm/K is derived from the slope. First, heating of the device causes an expansion of the material and thus a physical extension of the resonator. Second, the refractive index of the material increases with higher temperatures, leading to an additional extension of the optical path inside the resonator. Assuming the change of the optical resonator length to be small and supposing a constant number of nodes of the standing wave, the position of the longitudinal modes in the spectrum will shift to longer wavelengths.

3. Laser in Littrow Configuration

Another possibility to tune the emission wavelength is to use a selective feedback of the desired wavelength into the laser. Thus the gain at this wavelength is increased and the corresponding mode is preferred. Such a feedback can be realized using an external grating, which is described by the grating equation

$$m\lambda = d(\sin\alpha + \sin\beta) \quad , \tag{2}$$

where m is the order of diffraction, d is the grating constant, α is the angle of incidence, and β is the angle of the diffracted beam. For a given wavelength λ only those diffraction orders m are realizable where $|m\lambda/d| < 2$ is fulfilled.

In a special case of equation 2 the light is diffracted back in the incidence direction, i.e. $\alpha = \beta$. This arrangement is called Littrow configuration. The grating equation (2) is simplified to

$$m\lambda = 2d\sin\alpha \quad . \tag{3}$$

From this it follows that, after feeding back the diffraction order $m = 1$ into the laser, it is possible to tune the emission wavelength by rotating the grating which changes the angle of incidence α [1].

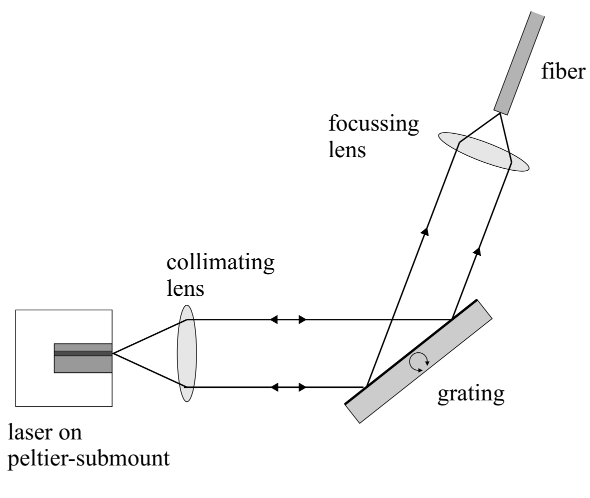

Fig. 3. Littrow-setup for tuning of the emission wavelength.

Figure 3 shows a setup for a tunable laser based on the Littrow configuration. The position of the collimating lens and the rotation of the grating are controlled by Piezo actuators. This allows for optimum coupling into the laser and high resolution selection of the Littrow wavelength. The width of the tunable range of this configuration is limited by the shape and the width of the gain curve of the laser. To force a laser mode which is not in the maximum of the gain curve, the back diffracted power has to be large enough to reach the threshold condition of the desired mode. Otherwise the spectrum will be dominated by the mode which is emitted without grating.

We used a grating with a groove spacing $d = \left(3600\ \frac{1}{\mathrm{mm}}\right)^{-1} = 277.8$ nm and coupled back the first order of diffraction $m = 1$ into the laser. The coupling was optimized by maximizing the output power, which is a result of a decrease of the threshold current by the back diffracted light. A reduction of the threshold current from 37.0 mA to 35.1 mA was evaluated.

By coupling back a wavelength close to the emission maximum, the SMSR was increased to 24.7 dB compared to 5.5 dB of the laser without grating. This is due to the reduced resonator losses obtained by the grating feedback. Thereby the corresponding mode is enhanced and the other modes are suppressed. For modes with a larger distance from the maximum of the gain curve results a lower SMSR, because the losses compared to the wavelength without grating are larger (figure 4). The SMSR at the free running wavelength is only 3.4 dB due to the spectral width of the diffracted light.

Figure 5 shows the spectra of the laser diode for the shortest and the largest wavelength where stable operation has been achieved. The laser could be tuned from 422.30 nm to 426.67 nm. For wavelengths exceeding that range the emission wavelength of the laser without grating dominated the spectrum. As one can see in figure 5, at the edge of the tuning range the wavelength of the free running laser had already approximately the same intensity as the forced wavelength.

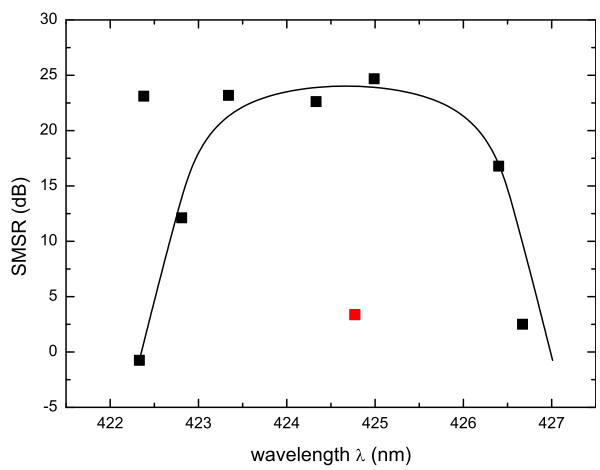

Fig. 4. SMSR (side mode suppression ratio) of the Nichia 425 nm laser with grating. (gray: emission wavelength without grating)

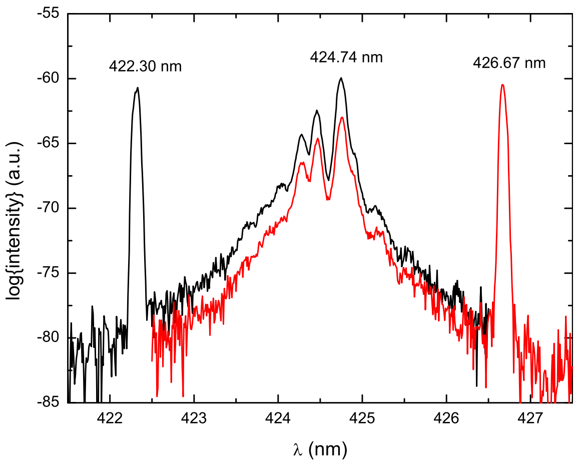

Fig. 5. The maximum tunable range of the Nichia 425 nm laser is 4.37 nm.

4. Conclusion

We investigated the effect of the temperature on emission properties and measured an increase of the wavelength of 0.8 nm for a rise of case temperature from 10°C to 30°C. A temperature coefficient $\frac{d\lambda}{dT} = 0.01339\ \frac{\text{nm}}{\text{K}}$ for the longitudinal modes was found. Applying an external feedback an improvement of the SMSR of 19.2 dB was achieved and the laser emission wavelength could be tuned over a range of 4.37 nm.

References

[1] C. Palmer, *"Diffraction Grating Handbook,"* Richardson Grating Laboratory, 4th edition, 2000.

[2] Sony Deutschland GmbH, "DVD Technologie," 2000 (http:\\www.sony.de).

[3] S. Nakamura and G. Fasol, *"The blue laser diode: GaN based light emitters and lasers,"* Springer-Verlag, 1997.

[4] S.C. Jain, M. Willander, J. Narayan, and R. Van Overstraeten, "III-nitrides: Growth, characterization, and properties," *J. Appl. Phys.*, vol. 87, no. 3, pp. 965–1006, 2000.

[5] M. Leroux and B. Gil. "Bandedge and optical functions of GaN," In J.H. Edgar, S. Strite, I. Akasaki, H. Amano, and C. Wetzel, editors, *Gallium Nitride and Related Semiconductors*. INSPEC, London, 1999.

Habilitation and Ph.D. Theses

[1] Markus Kamp. *GaN-based Light Emitters — Epitaxy, Technology, and Devices*. Habilitation Thesis, Optoelectronics Department, 2001.

[2] Wolfgang Schmid. *Hocheffiziente Leuchtdioden mit lateralem Auskoppeltaper: Konzept, Herstellung und Eigenschaften*. Ph.D. Thesis, Optoelectronics Department, 2001.

[3] Christoph Kirchner. *Metallorganische Gasphasenepitaxie für optoelektronische und elektronische Bauelemente im Materialsystem AlGaInN*. Ph.D. Thesis, Optoelectronics Department, 2001.

Diploma Theses and Semester Projects

[1] Daniel Supper. Herstellung und Charakterisieurng von oberflächenemittierenden Laserdioden mit Vertikalresonator mit integrierten Elementen zur Modenkontrolle. Diploma Thesis, Optoelectronics Department, 2001.

[2] Torsten Sven Schaal. Hochbitratiges optisches Datenbertragungssystem auf Basis von Standard PMMA Fasern für Kraftfahrzeuge. Diploma Thesis, DaimlerChrysler Forschungszentrum Ulm, 2001.

[3] Christoph Eichler. Charakterisierung GaN-basierender Laserdioden mit Emission im ultravioletten Spektralbereich. Diploma Thesis, Optoelectronics Department, 2001.

[4] Frank Habel. Optimierung und Skalierung von HVPE Prozessen zur Herstellung von Galliumnitrid Substraten und Quasisubstraten. Diploma Thesis, Optoelectronics Department, 2001.

[5] Ihab Kardosh. Substratseitig emittierende Vertikallaserdioden mit integrierten Mikrolinsen. Diploma Thesis, Optoelectronics Department, 2001.

[6] Doris Yacoub. Zuverlässigkeit von Vertikallaserdioden. Diploma Thesis, Optoelectronics Department, 2001.

[7] Lennart Elmar Schreiber. Herstellung und Charakterisierung von Esaki Tunneldioden. Semester Project, Optoelectronics Department, 2001.

[8] Michael Furitsch. Optische Kopplung eines hybriden Laser-Verstärker Systems. Semester Project, Optoelectronics Department, 2001.

[9] Melanie Decker. Herstellung und Charakterisierung von Laserdioden mit verbesserten Strahleigenschaften. Semester Project, Optoelectronics Department, 2001.

[10] Andreas Munding. Aufbau eines computergestützten Messplatzes zur Charakterisierung von kantenemittierenden Lasern. Semester Project, Optoelectronics Department, 2001.

[11] Martin Peschke. Quantitativer Vergleich von legierenden Kontakten mit und ohne Gold-Diffusionssperre auf schwach dotiertem Galliumarsenid. Semester Project, Infineon München, 2001.

[12] Tobias Frey. Untersuchungen zur Strahlqualität eines Oszillator-Laserverstärkersystems auf Halbleiterbasis. Semester Project, Optoelectronics Department, 2001.

Talks

[1] I. Ecker, S. Menzel, J. Joos, and K. Ebeling, "Wachstum von GaAsSb/GaAs Breitstreifenlaserdioden mit Emissionswellenlängen nahe 1.3 μm," *MBE Workshop 2001*, Berlin, Germany, Sep. 2001.

[2] I. Ecker, S. Menzel, J. Joos, R. Michalzik, and K. Ebeling, "Wachstum von GaAsSb/GaAs Breitstreifenlaserdioden mit Emissionswellenlängen nahe 1.3 μm mittels Gasquellen-Molekularstrahlepitaxie," *Photonik-Symposium 2001 der Volkswagen-Stiftung*, Baden bei Wien, Austria, Sep. 2001.

[3] M. Golling, T. Knödl, R. Michalzik, and K. Ebeling, "MBE mehrstufiger Vertikallaserdioden," *Workshop Epitaxie von III/V-Halbleitern, DGKK 2001*, Berlin, Germany, Dec. 2001.

[4] F. Habel, M. Seyboth, R. Beccard, and M. Heuken, "HVPE auf strukturierten Substraten," *Workshop Epitaxie von III/V-Halbleitern, DGKK 2001*, Berlin, Germany, Dec. 2001.

[5] M. Kicherer, "Optische Übertragungssysteme mit integrierten Halbleiterlasern," *Optische Netze Forum 2001*, Königswinter, Germany, Nov. 2001.

[6] R. Michalzik, M. Golling, R. Jäger, M. Kicherer, R. King, T. Knödl, S. Mahmoud, F. Mederer, G. Steinle, H. Unold, and K. Ebeling, "What's hot in VCSEL research at Ulm University?," Colorado State University, Dept. of Electrical & Computer Engineering, Fort Collins, CO, USA, Aug. 2001.

[7] R. Michalzik, M. Golling, R. Jäger, M. Kicherer, R. King, T. Knödl, S. Mahmoud, F. Mederer, G. Steinle, H. Unold, and K. Ebeling, "Current topics of research into VCSELs at Ulm University," Cielo Communications, Broomfield, CO, USA, Aug. 2001.

[8] R. Michalzik and K. Ebeling, "VCSELs: Characteristics and applications," *Laser seminar*, Max-Planck-Institute for Quantum Optics, Garching, Germany, Feb. 2001.

[9] M. Riedl, M. Golling, E. Schiehlen, and P. Unger, "MBE von optisch gepumpten VECSELs," *Workshop Epitaxie von III/V-Halbleitern, DGKK 2001*, Berlin, Germany, Dec. 2001.

[10] S. Schad, M. Seyboth, C. Kirchner, M. Kamp, I. Daumiller, M. Neuburger, and E. Kohn, "InGaN, a material for electronic devices?!," *WOCSDICE 2001*, Cagliari, Sardinia, Italy, May 2001.

[11] M. Seyboth and M. Kamp, "Substrates for wide bandgap nitrides," *EWMOVPE IX* (invited), Wrexham, Wales, UK, June 2001.

[12] P. Unger, "Optoelectronic integrated circuits (OIC): technologies and processes," *Winter School on Optoelectronics and Photonics, 'Micro-optoelectronics: Materials, Devices and Integration'*, Trento, Italy, Mar. 2001.

[13] H. Unold, R. Michalzik, and K. Ebeling, "New concepts for single-mode VCSELs," *European Semiconductor Laser Workshop*, Gent, Belgium, Sep. 2001.

Publications and Conference Contributions

[1] H. Chung, A. Pelzmann, M. Drechsler, M. Scherer, V. Schwegler, M. Seyboth, C. Kirchner, and M. Kamp, "Multiple-step annealing for 50% enhanced p-conductivity of GaN," *J. Crystal Growth*, vol. 230, pp. 549–553, 2001.

[2] E. Deichsel, F. Eberhard, R. Jäger, and P. Unger, "High-power laser diodes with dry-etched mirror facets and integrated monitor photodiodes," *IEEE J. Selected Topics Quantum Electron.*, vol. 7, pp. 106–110, 2001.

[3] E. Deichsel and P. Unger, "High-brightness semiconductor lasers fabricated with improved dry-etching technology for ultra-smooth laser facets," in Proc. *Microprocesses and Nanotechnology Conference, MNC 2001*, Shimane, Japan, pp. 218–219, Oct. 2001.

[4] K. Ebeling, "VCSELs: Further progress," in Proc. *Focus Meetings at the Conference on Lasers and Electro-Optics Europe, CLEO/Europe 2001*, Munich, Germany, p. 35, June 2001.

[5] K. Ebeling, F. Mederer, R. King, M. Kicherer, G. Steinle, and R. Michalzik, "Advances in optical interconnect technology," in Proc. *Microoptics Conference, MOC 2001,* (Plenary talk), Osaka, Japan, pp. 4–7, Oct. 2001.

[6] M. Golling, T. Knödl, A. Straub, M. Kicherer, and K. Ebeling, "Optimization strategies for diode cascade InGaAs VCSELs," in *Vertical Cavity Surface Emitting Lasers V, SPIE Proc.*, vol. 4286, San Jose, CA, USA, pp. 102–108, Jan. 2001.

[7] R. King, R. Michalzik, R. Jäger, and K. Ebeling, "32-VCSEL channel CMOS-based transmitter module for Gb/s data rates," in *Vertical Cavity Surface Emitting Lasers V, SPIE Proc.*, vol. 4286, San Jose, CA, USA, pp. 136–141, Jan. 2001.

[8] T. Knödl, M. Golling, A. Straub, and K. Ebeling, "Multi-diode cascade VCSEL with 130 % differential quantum efficiency at cw room temperature operation," *Electron. Lett.*, vol. 37, pp. 31–33, 2001.

[9] T. Knödl, A. Straub, M. Golling, R. Michalzik, and K. Ebeling, "Scaling behavior of bipolar cascade VCSELs," *IEEE Photon. Technol. Lett.*, vol. 13, pp. 930–932, 2001.

[10] T. Knödl, "Cascade VCSEL with 130% slope efficiency," *Compound Semiconductor Magazine*, vol. 7, p. 50, 2001.

[11] T. Knödl, M. Golling, A. Straub, M. Miller, H. Choy, R. Michalzik, and K. Ebeling, "Influence of design variations on bipolar cascade VCSEL performance," in Proc. *Lasers and Electro-Optics Society, LEOS 2001*, San Diego, USA, pp. 463–464, Nov. 2001.

[12] S. Mahmoud, D. Wiedenmann, M. Kicherer, H. Unold, R. Jäger, R. Michalzik, and K. Ebeling, "Spatial investigation of transverse mode turn-on dynamics in VCSELs," *IEEE Photon. Technol. Lett.*, vol. 13, pp. 1152–1154, 2001.

[13] S. Mahmoud, H. Unold, W. Schmid, R. Jäger, R. Michalzik, and K. Ebeling, "Analysis of longitudinal mode wave guiding in vertical-cavity surface-emitting lasers with long monolithic cavity," *Appl. Phys. Lett.*, vol. 78, pp. 586–588, 2001.

[14] F. Mederer, R. Jäger, H. Unold, R. Michalzik, K. Ebeling, S. Lehmacher, A. Neyer, and E. Griese, "3-Gb/s data transmission with GaAs VCSELs over PCB integrated polymer waveguides," *IEEE Photon. Technol. Lett.*, vol. 13, pp. 1032–1034, 2001.

[15] F. Mederer, R. Jäger, J. Joos, M. Kicherer, R. Michalzik, M. Riedl, H. Unold, A. Cheleg, K. Ebeling, S. Lehmacher, B. Wittmann, and A. Neyer, "Improved VCSEL structures for 10 Gigabit-Ethernet and next generation optical-integrated PC-boards," in Proc. *Electronic Components and Technology Conference, ECTC 2001*, Orlando, USA, pp. 1–7, May 2001.

[16] F. Mederer, G. Steinle, G. Kristen, R. Michalzik, H. Riechert, A. Egorov, and K. Ebeling, "Up to 10 Gbit/s data transmission with 1.3 μm wavelength InGaAsN VCSELs," in Proc. *European Conference on Optical Communication, ECOC 2001*, Amsterdam, Netherlands, pp. 218–219, Sep. 2001.

[17] F. Mederer, I. Ecker, J. Joos, M. Kicherer, H. Unold, K. Ebeling, M. Grabherr, R. Jäger, R. King, and D. Wiedenmann, "High performance selectively oxidized VCSELs and arrays for parallel high-speed optical interconnects," *IEEE Trans. Advanced Packaging*, vol. 24, pp. 442–449, 2001.

[18] R. Michalzik, F. Mederer, R. King, M. Kicherer, R. Jäger, and K. Ebeling, "Very short reach optical interconnect applications of vertical-cavity surface-emitting laser diodes," *Kleinheubacher Berichte*, vol. 44, pp. 85–94, 2001.

[19] R. Michalzik, R. King, F. Mederer, M. Kicherer, G. Giaretta, and K. Ebeling, "Short-wavelength vertical-cavity surface-emitting laser applications: from high throughput multimode fiber links to two-dimensional interchip interconnections," *Opt. Eng.*, vol. 40, pp. 1179–1185, 2001.

[20] R. Michalzik, K. Ebeling, M. Kicherer, F. Mederer, R. King, H. Unold, and R. Jäger, "High-performance VCSELs for optical data links," *IEICE Trans. Electron.*, (invited), vol. E84-C, pp. 629–638, 2001, also published in *IEICE Trans. Commun.*, vol. E84-B, pp. 1255–1264, 2001.

[21] R. Michalzik, M. Kicherer, and H. Unold, "VCSELs for high-throughput very short reach optical interconnects," *SPIE Newsletter, Optics & Information Systems*, vol. 12, p. 6, 2001.

[22] R. Michalzik, R. King, R. Jäger, S. Müller, and K. Ebeling, "VCSEL arrays for CMOS integrated optical interconnect systems," in *Optoelectronic and Wireless Data Management, Processing, Storage and Retrieval,* R. Raymond, P.K. Srimani, R. Su, C.W. Wilmsen (Eds.), Proc. SPIE 4534 (invited), Denver, CO, USA, pp. 101–113, Aug. 2001.

[23] M. Miller, M. Grabherr, R. Jäger, and K. Ebeling, "High-power VCSEL arrays for emission in the Watt regime at room temperature," *IEEE Photon. Technol. Lett.*, vol. 13, pp. 173–175, 2001.

[24] M. Miller, M. Grabherr, R. King, R. Jäger, R. Michalzik, and K. Ebeling, "Improved output performance of high-power VCSELs," *IEEE J. Selected Topics Quantum Electron.*, vol. 7, pp. 210–216, 2001.

[25] T. Rotter, D. Mistele, J. Stemmer, M. Seyboth, S. Paprotta, V. Schwegler, F. Fiedler, H. Klausing, O. Semchinova, J. Aderhold, and J. Graul, "First AlGaN/GaN metal oxide semiconductor heterostructure field effect transistor based on a photoanodic oxide," *Electron. Lett.*, vol. 37, pp. 715–716, 2001.

[26] S. Schad, M. Scherer, M. Seyboth, and V. Schwegler, "Extraction efficiency of GaN-based LEDs," *Phys. Stat. Sol. (A)*, pp. 127–130, 2001.

[27] M. Scherer, V. Schwegler, M. Seyboth, C. Kirchner, M. Kamp, A. Pelzmann, and M. Drechsler, "Low resistive p-type GaN using two-step rapid thermal annealing processes," *J. Appl. Phys.*, vol. 89, pp. 8339–8341, 2001.

[28] M. Scherer, V. Schwegler, M. Seyboth, F. Eberhard, C. Kirchner, M. Kamp, G. Ulu, M. Ünlü, R. Gruhler, and O. Hollricher, "Characterization of etched facets for GaN-based lasers," *J. Crystal Growth*, vol. 230, pp. 554–557, 2001.

[29] W. Schmid, M. Scherer, R. Jäger, P. Stauß, K. Streubel, and K. Ebeling, "Efficient light-emitting diodes with radial outcoupling taper at 980 and 630 nm emission wavelength," in *Light-Emitting Diodes: Research, Manufacturing, and Applications V, SPIE Proc.*, vol. 4278, San Jose, CA, USA, pp. 109–118, Jan. 2001.

[30] V. Schwegler, S. Schad, M. Scherer, M. Kamp, G. Ulu, M. Emsley, M. Ünlü, A. Lell, S. Bader, B. Hahn, H. Lugauer, F. Kühn, A. Weimar, and V. Härle, "GaN-based lasers on SiC: influence of mirror reflectivity on L–I characteristics," *J. Crystal Growth*, vol. 230, pp. 512–516, 2001.

[31] P. Unger, "Optoelectronic integrated circuits (OIC): technologies and processes," in *'Micro-optoelectronics: Materials, Devices and Integration'* edited by M. Ferrari, L. Pavesi, G.C. Righini, Collana Quaderni di Ottica e Fotonica, vol. 8, pp. 1–19, 2001.

[32] H. Unold, S. Mahmoud, R. Jäger, M. Grabherr, R. Michalzik, and K. Ebeling, "Large-area single-mode VCSELs and the self-aligned surface relief," *IEEE J. Selected Topics Quantum Electron.*, vol. 7, pp. 386–392, 2001.

[33] H. Unold, M. Riedl, S. Mahmoud, R. Jäger, and K. Ebeling, "Long monolithic cavity VCSELs for high singlemode output power," *Electron. Lett.*, vol. 37, pp. 178–179, 2001.

[34] H. Unold, M. Golling, F. Mederer, R. Michalzik, D. Supper, and K. Ebeling, "Single-mode output power enhancement of InGaAs VCSELs by reduced spatial hole burning via surface etching," *Electron. Lett.*, vol. 37, pp. 570–572, 2001.

[35] H. Unold, M. Golling, R. Michalzik, D. Supper, and K. Ebeling, "Photonic crystal surface-emitting lasers: tailoring waveguiding for single-mode emission," in Proc. *European Conference on Optical Communication, ECOC 2001*, Amsterdam, Netherlands, pp. 520–521, Sep. 2001.

[36] C. Wang, H. Chung, M. Seyboth, M. Kamp, K. Ebeling, R. Beccard, and M. Heuken, "Influence of growth parameters on crack density in thick epitaxially lateral overgrown GaN layers by hydride vapor phase epitaxy," *J. Crystal Growth*, vol. 230, pp. 377–380, 2001.

[37] J.-P. Hermier, A. Bramati, A. Khoury, V. Josse, E. Giacobino, P. Schnitzer, R. Michalzik, and K. Ebeling, "Noise characteristics of oxide confined vertical-cavity surface emitting lasers," *IEEE J. Quantum Electron.*, vol. 37, pp. 87–91, 2001.

[38] E. Kohn, I. Daumiller, M. Neuburger, M. Seyboth, C. Kirchner, and M. Kamp, "InGaN-channel FETs – growth, technology and characteristics," in Proc. *MRS Spring Meeting* (invited), vol. 680, no. E3.1, San Francisco, CA, USA, Apr. 2001.

[39] S. Lehmacher, A. Neyer, and F. Mederer, "Polymer optical waveguides integrated in printed circuit boards," in Proc. *European Conference on Optical Communication, ECOC 2001*, Amsterdam, Netherlands, pp. 302–303, Sep. 2001.

[40] A. Oster, M. Zorn, H. Unold, J. Sebastian, H. Wenzel, W. John, M. Weyers, and G. Tränkle, "Development of 650 nm-emitting VCSELs for cw operation," in Proc. *27th International Symposium of Compound Semiconductors, ISCS 2000*, Monterey, USA, pp. 377–382, Oct. 2001.

[41] H. Riechert, G. Steinle, and F. Mederer, "1300 nm VCSELs as next generation optical sources for 10 Gbit/s systems," *LaserOpto magazine*, vol. 5, pp. 70–72, 2001.

[42] S. Riyopoulos, H. Unold, and J. Liu, "Tailoring of transverse and longitudinal mode stability in extended cavity VCSELs, using paraxial eigenmode algorithms," in Proc. *Lasers and Electro-Optics Society, LEOS 2001*, San Francisco, USA, pp. 465–466, Nov. 2001.

[43] G. Steinle, F. Mederer, M. Kicherer, R. Michalzik, G. Kristen, A. Egorov, H. Riechert, H. Wolf, and K. Ebeling, "Data transmission up to 10 Gbit/s with 1.3 μm wavelength InGaAsN VCSELs," *Electron. Lett.*, vol. 37, pp. 632–634, 2001.

[44] L. Vanwassenhove, R. Bockstaele, R. Baets, M. Brunfaut, W. Meeus, J. V. Campenhout, J. Hall, H. Melchior, A. Neyer, J. V. Koetsem, R. King, K. Ebeling, and P. Heremans, "Demonstration of 2-D plastic optical fibre based optical interconnect between CMOS IC's," in Proc. *Optical Fiber Communication, OFC 2001*, vol. WDD74, Anaheim, CA, USA, pp. 1–3, Mar. 2001.

[45] M. Willemsen, A. van de Nes, M. van Exter, J. Woerdman, M. Kicherer, R. King, R. Jäger, and K. Ebeling, "Polarization-resolved linewidth-power product of a vertical-cavity semiconductor laser," *Appl. Phys. Lett.*, vol. 89, pp. 4183–4185, 2001.

Submitted Publications and Conference Contributions

[1] M. Kicherer, A. Fiore, U. Österle, R. Stanley, M. Ilegems, and R. Michalzik, "Data transmission using GaAs-based InAs-InGaAs quantum dot LEDs emitting at 1.3 μm wavelength," *Electron. Lett.*, 2001, submitted.

[2] F. Mederer, I. Ecker, R. Michalzik, G. Steinle, H. Riechert, K. Ebeling, B. Lunitz, J. Moisel, and D. Wiedenmann, "VCSEL transmitters for 10-Gigabit Ethernet: 1.3 μm wavelength VCSELs for metropolitan-area-networks and TO-packaged 850 nm wavelength VCSELs for data transmission over multimode fibers and optical backplane-waveguides," in Proc. *Electronic Components & Technology Conference, ECTC 2002*, San Diego, California, USA, May 2002, accepted.

[3] D. Mistele, T. Rotter, K. Röver, S. Paprotta, M. Seyboth, V. Schwegler, F. Fedler, H. Klausing, O. Semchinova, J. Stemmer, J. Aderhold, and J. Graul, "First AlGaN/GaN MOSFET with photoanodic gate dielectric," *Mat. Sci. Eng. (B)*, 2001, in press.

[4] D. Mistele, T. Rotter, Z. Bougrioua, I. Moermann, K. Röver, M. Seyboth, V. Schwegler, J. Stemmer, F. Fedler, H. Klausing, O. Semchinova, J. Aderhold, and J. Graul, "AlGaN/GaN MOSHFETs with different gate dielectrics and treatment," in *MRS Fall Meeting*, Boston, MA, USA, Nov. 2001, in press.

[5] M. Scherer, B. Neubert, S. Schad, W. Schmid, C. Karnutsch, W. Wegleiter, A. Plössl, and K. Streubel, "Efficient InAlGaP light-emitting diodes using radial outcoupling taper," in *Photonics West 2002, SPIE Proc.*, Jan. 2002, accepted.

[6] E. Schiehlen, M. Golling, and P. Unger, "Diode-pumped semiconductor disk laser with intra-cavity frequency doubling using Lithium Triborate (LBO)," *IEEE Photon. Technol. Lett.*, vol. 14, pp. 777–779, 2002.

[7] W. Schmid, M. Scherer, C. Karnutsch, A. Plößl, W. Wegleiter, S. Schad, B. Neubert, and K. Streubel, "High efficiency, red and infrared light-emitting diodes using radial outcoupling taper," *IEEE J. Selected Topics Quantum Electron.*, 2001, accepted.

[8] H. Unold, S. Mahmoud, R. Jäger, M. Golling, M. Kicherer, F. Mederer, M. Riedl, T. Knödl, M. Miller, R. Michalzik, and K. Ebeling, "Single-mode VCSELs," in *Photonics West 2002, SPIE Proc.*, San Jose, CA, USA, Jan. 2002, accepted.

[9] H. Unold, M. Riedl, R. Michalzik, and K. Ebeling, "Polarization control in VCSELs by elliptic surface etching," *Electron. Lett.*, 2001, submitted.

[10] E. Kohn, I. Daumiller, M. Kunze, M. Seyboth, and C. Kirchner, "InGaN-channel FETs – a case of polar heterojunctions," in Proc. *International Workshop on the Physics of Semiconductor Devices, IWPSD 2001*, New Delhi, India, Dec. 2001, in press.

[11] S. Riyopoulos and H. Unold, “Theoretical interpretation of the enhanced single mode stability in extended cavity VCSELs,” *IEEE J. Quantum Electron.*, 2001, submitted.

[12] B. Stegmüller, E. Baur, and M. Kicherer, “1.55 μm and 1.3 μm DFB lasers integrated with electro absorption modulators for high-speed transmission systems,” in Proc. *Second Joint Symposium on Opto- & Microelectronic Devices and Circuits, SODC 2002*, Stuttgart, Germany, Mar. 2002, submitted.